



UNIVERSITÀ DEGLI STUDI DI CATANIA  
DIPARTIMENTO DI FISICA E ASTRONOMIA  
CORSO DI LAUREA MAGISTRALE IN FISICA

---

Absolute dosimetry and diagnostics of laser-driven ion  
beams with Faraday Cup

---

TESI DI LAUREA

---

Giada Petringa

**Relatore:**

Prof. Giacomo Cuttone

**Correlatori:**

Dott. G. A. Pablo Cirrone

Dott. Francesco Romano

Dott.ssa Valentina Scuderi

---

ANNO ACCADEMICO 2014/2015

A Rosetta

# Contents

<b>Introduction</b>	<b>4</b>
<b>1 The Hadron - therapy</b>	<b>8</b>
1.1 Interaction of heavy charged particles . . . . .	8
1.1.1 Stopping - Power . . . . .	9
1.1.2 The Bragg peak . . . . .	11
1.2 Linear Energy Transfer . . . . .	15
1.3 The dose concept . . . . .	17
1.4 Relative Biologic Effectiveness . . . . .	18
1.5 The traditional accelerators machines . . . . .	22
<b>2 The ELIMED project</b>	<b>25</b>
2.1 The ELIMED transport beamline: Collecting, focusing and selection system . . . . .	28
2.2 Diagnostics of laser-accelerated ion beams . . . . .	31
2.2.1 Thompson Parabola Spectrometer . . . . .	31
2.2.2 Time Of Flight detectors (ToF) . . . . .	34
2.3 Relative and absolute dosimetry of laser-accelerated ion beams	39
2.3.1 Radiochromic Film . . . . .	39
2.3.2 CR39 . . . . .	40
2.3.3 ELImon . . . . .	41
<b>3 Laser-plasma interaction</b>	<b>42</b>
3.1 High intensity laser . . . . .	43

3.2	Plasma characteristics . . . . .	45
3.2.1	Plasma frequency and <i>Debye length</i> . . . . .	46
3.3	Laser Interaction with matter . . . . .	48
3.3.1	Laser-induced ionization . . . . .	48
3.3.2	Sputtering effect . . . . .	49
3.3.3	Laser-absorption and energy transfer . . . . .	49
3.3.4	Ponderomotive force . . . . .	50
3.4	Laser induced ion acceleration . . . . .	52
3.4.1	Target Normal Sheath Acceleration TNSA . . . . .	53
3.4.2	Radiation Pressure Acceleration . . . . .	57
<b>4</b>	<b>Dosimetry for a laser - driven beam</b>	<b>58</b>
4.1	The Faraday Cup . . . . .	59
4.1.1	The Faraday Cup as beam intensity monitor . . . . .	59
4.1.2	The Faraday Cup as absolute dosimeter system . . . . .	60
4.2	Preliminary test . . . . .	66
4.2.1	Experimental setup at <i>Centro di AdroTerapia e Applicazioni Nucleari Avanzate</i> (CATANA) . . . . .	67
4.2.2	Experimental characterization . . . . .	68
<b>5</b>	<b>Experimental tests in laser facilities</b>	<b>76</b>
5.1	Terawatt Apparatus for Relativistic And Nonlinear Interdisciplinary Science (TARANIS) . . . . .	77
5.2	Prague Asterix Laser System (PALS) . . . . .	79
5.3	Time of flight measurements . . . . .	82
5.3.1	Energy distribution of the ions emitted . . . . .	82
5.3.2	Experimental Set-up at the TARANIS facility . . . . .	85
5.3.3	Data analysis . . . . .	87
5.4	ElectroMagnetic Pulse (EMP) . . . . .	96
5.4.1	Characterization of the EMP propagation . . . . .	97
5.4.2	EMP signal investigation as a function of the laser parameters . . . . .	103

<b>Conclusion</b>	<b>108</b>
<b>Ringraziamenti</b>	<b>109</b>
<b>Appendix A</b>	<b>110</b>
<b>Appendix B</b>	<b>120</b>
<b>Appendix C</b>	<b>122</b>
<b>Bibliography</b>	<b>124</b>

# Introduction

Hadrontherapy is a well-established technique for cancer radiation therapy which employs beams of charged hadrons, mainly protons and carbon ions. Due to their physical and radiobiological properties, they allow conformal treatment avoiding the damaging of healthy tissues located in proximity of the tumour[4]. So this technique allows a higher control of the disease with respect to the conventional radiation therapy using photons. The accelerating machines used in this field are mostly cyclotrons and synchrotrons which are huge, complex and expensive machines. For this reason, nowadays, only about 60 centers are available around the world[2].

In order to increase the hadrontherapy spread, several advanced technological solutions, based on the research in laser-matter interaction field, are currently under investigation by the scientific community. In this framework, during the last decades, the research has led to the development of an innovative proton and ion acceleration technique, which might represent a valid alternative to the conventional ones.

In this contest, an international project named ELIMED (Extreme Light Infrastructure for MEDical application) was born in 2011 by a common initiative proposed by researches of the INFN-LNS in Catania and FZU (Academy of Sciences of Czech Republic) in Prague[7].

The activity of the project is entirely focused on the development of innovative instrumentation, technologies and dosimetric methodologies pointed to the realization of a beam line for dosimetric and radiobiological studies based on laser-driven beams[21]. The ELIMED project activities will lead to the delivery and assembly, within 2017, of the first beam line for hadrontherapy studies using laser - driven beams accelerated up to 60 MeV at the ELI-Beamlines laser facility in Prague (CZ). High energy charged particles, such as protons and ions, can be, accelerated by means of high intensity laser beams interacting with matter creating a plasma. The interaction of a strong

laser pulse with a target can generate plasma waves capable of accelerating electrons to higher energies via non-linear forces[38]. Fast electrons are generated immediately due to their small mass. Their fast displacement from the interaction point creates a spatial charge separation leading to a high intensity electric field causing the acceleration of protons and heavier ions. Recent progress in laser technology enables the production of laser pulses with intensities high enough to accelerate protons/ions to energies of several ten's of MeV from thin solid targets.

This thesis, developed in the framework of the ELIMED project, focuses on the characterization of an innovative Faraday Cup (FC), a device designed and realized for the absolute dose measurements with laser driven ion beams and the characterization of the diagnostics devices for the energy distribution measurements. The FC is one of the fundamental components in the dosimetric system that will be realized for the first beamline entirely dedicated to the high energy (60-250 MeV) optically accelerated proton beam physics and radiobiological studies. As it is well known, the FC has a linear response with the dose-rate for a large range of fluences: therefore it is a very good candidate for absolute dose measurements with conventional proton beams as well as for laser-driven proton beam, since very high dose pulses are expected. In order to characterize the FC in terms of charge efficiency and dose, the FC has been preliminary tested in November 2014 using the 62 MeV clinical proton beam in an experimental campaign carried out at the CATANA (Centro di AdroTerapia e Applicazioni Nucleari Avanzate) protontherapy facility of the Southern National Laboratory (LNS) in Catania.

In addition, an experimental campaign has been performed at the Terawatt Apparatus for Relativistic And Nonlinear Interdisciplinary Science (TARANIS) at the Queen's University in Belfast (December - February 2015) and at the Prague Asterix Laser System (PALS) in Prague (May 2015). This experimental campaign has been performed in order to investigate the characteristic signal features by the Faraday Cup in terms of particle emission, energy spectra and electromagnetic pulse component.

In the first chapter, the description of the charged particle interaction with matter is reported. The advantages of using ion beams in tumor treatment as well as the benefits of hadrontherapy in relation to traditional radiotherapy, in terms of enhanced biological effectiveness and survival probability are also discussed.

The second chapter contains an overview of the ELIMED transport beam-

line and dosimetric systems for laser-generated beams, which will be installed at the ELI-Beamlines facility in Prague. The components of the transport beam-line based on the quadrupoles system and an Energy Selection System, are described. Furthermore, the dosimetric system and the devices that will be used for the diagnostics are also discussed.

In the third chapter, a theoretical description of the acceleration processes occurring when an high power laser interacts with matter is reported with a review of the state-of-the-art of ultra intense pulse production based on the CPA system.

In the fourth chapter the description of the innovative Faraday Cup developed at Southern National Laboratory is briefly outlined. The Faraday Cup is characterized by a peculiar geometry of the electric field, allowing maximizing the secondary electron suppression. This will allow reaching an high level of accuracy in the charge collection and in the dose extraction. Furthermore, the response of the detector versus the applied voltage of the suppressor electrodes, the dose, the dose rate and the preliminary results of the experimental campaign performed at LNS, have been listed.

In the fifth chapter the results obtained in the two experimental campaigns at PALS and TARANIS facilities are presented. The plasma characterization in terms of particles emission has been obtained using a Silicon Carbide and a Diamond detector in time of flight configuration. The results on the proton energy spectrum and fluence extracted from the Radiochromic film stack and the CR39 detectors are also shown. The results on the EMP characterization depending on the different laser parameters and targets, performed in the two laser facilities, are also reported.

# Chapter 1

## The Hadron - therapy

### 1.1 Interaction of heavy charged particles

Charged particles lose their energy differently from that of uncharged radiations (e.g. x or gamma rays and neutrons). An individual photon or neutron incident upon a slab of matter may pass through it with no interactions at all and, consequently, no loss of energy. In alternative it may interact and thus lose its energy in one or a few “catastrophic” events. By contrast, a charged particle, being surrounded by its Coulomb electric force field, interacts with one or more electrons or with the nucleus of practically every atom it contacts. Most of these interactions individually transfer only small fractions of the incident particle’s kinetic energy: particles gradually lose their kinetic energy in a friction-like process, often referred as the “continuous slowing-down approximation”[8]. If a stochastic point of view is assumed in the description of these processes, it is possible to roughly predict how far an individual photon or neutron will penetrate through matter, since only one or few randomly occurring interactions are needed to dissipate all of its quantum or kinetic energy. Charged particles, on the other hand, can be approximately characterized by a common pathlength, traced out by most such particles of given type and energy in a specific medium. Because of the multitude of the interactions undergone by each charged particle while slowing down, its path length tends to approach the expectation value that would be observed as a mean for a very large population of identical particles.

### 1.1.1 Stopping - Power

In general, two main features characterize the passage of charged particles through matter: a loss of energy and a deflection of the particle from its incident direction. These effects are primarily the result of two processes:

1. inelastic collisions with the atomic electrons of the material;
2. elastic and inelastic scattering from nuclei.

Among these, the first process is almost the unique responsible for the energy loss of charged particles in the matter. In these collisions the energy is transferred from particle to atom causing the ionization or excitation of the latter. The amount of energy transferred in each collision is generally a very small fraction of the particle's total kinetic energy; however, the number of collisions per unit path length is so large that a substantial cumulative energy loss is observed even in relatively thin layers of material. These atomic collisions are divided into two different groups: soft collisions, in which only an excitation is obtained and hard collisions, in which the energy transferred is sufficient to cause ionization[10]. In some of the hard reactions, enough energy is, in fact, transferred such that the electron itself causes substantial secondary ionization. These high-energy recoil electrons are sometimes referred to as  $\delta$ -rays.

Elastic scattering between a charged particle with the medium atomic number can also occur, even if with a smaller interaction cross section. In general very little energy is transferred in these collisions since the masses of the nuclei of many materials are usually large compared to the incident particles.

The inelastic collisions are, of statistical nature and they occur with a certain quantum mechanical probability. However, as their number per macroscopic pathlength is generally large, the fluctuations in the total energy loss are small and one can work with the average energy loss per unit path length. This quantity, called stopping power was first calculated by Bohr using classical arguments and later by Bethe, Bloch and others using a quantum mechanical formulation.

In the famous paper "On the theory of the decrease of velocity of moving electrified particles on passing through matter" [9] Bohr derived an expression for the stopping cross section per target electron using the collision classical theory. He considered the energy transfer of a projectile (of mass, charge

and velocity known) to a target electron due to a collision with an impact parameter depending to the incident angle. However for lighter particles the formula breaks down because of quantum effects.

The correct quantum - mechanical calculation was firstly performed by Bethe, Bloch and other authors. In the calculation, the energy transfer is parametrized in terms of momentum transfer rather than the impact parameter. The equation obtained is commonly known as the Bethe - Bloch formula and is the basic expression used for energy loss calculation:

$$-\frac{dE}{dx} = \frac{2\pi r_e^2 m_e c^2 \rho z^2 N_a Z}{\beta^2 A} \left[ \ln \left( \frac{2m_e \gamma^2 v^2 W_{max}}{I^2} \right) - 2\beta^2 - \delta - 2\frac{C}{Z} \right] \quad (1.1)$$

In this expression,  $v$  and  $z$  are the velocity and charge of the primary particle,  $A$  and  $Z$  are the atomic weight and the atomic number of the absorber atoms,  $m_e$  is the electron mass,  $r_e$  the classical electron radius and  $e$  is the electronic charge. The parameter  $I$  represents the average excitation and ionization potential of the absorber and is normally treated as an experimentally determined parameter significant. The terms  $\beta$  and  $\gamma$  are the relativistic corrections for the incident particle velocity.

The *density correction*,  $\delta$  is an important correction to the Bethe-Bloch formula at high energy while the *shell correction*  $C$  is important at low energy[8]. The Born approximation assumption is not well satisfied when the velocity of the passing particle finishes to be much greater than that of the atomic electrons in the stopping medium. Since K-shell electrons have the highest velocities, they are firstly affected by insufficient particle velocity, the slower L-shell electrons are next, and so on. The so called *shell correction* is intended to account for the resulting error in the Born's formula.

The second correction term,  $\delta$  to account for the *polarization* or *density effect* in condensed media is included. The density effect is due to particles electric field that tends to polarize the atoms along their path. This effect increase with the incident particle energy. The material density have a important role, as well inducing a greater solid state polarization than that in the state gas. The correction for the density effect is less than 0.1% for proton up to 800 MeV while its contribute results non-negligible for electrons.

The maximum energy transfer in a single collision is:

$$W_{max} = \frac{2m_e c^2 \beta \gamma}{1 + 2(m_e/M) \sqrt{1 + (\beta \gamma)^2 + (m_e/M)^2}} \quad (1.2)$$

for an incident particle of mass  $M$ .

An example of the energy dependence of  $dE/dx$  is shown in Figure 1.1 where the Bethe - Bloch formula as a function of the particle kinetic energy for several different particles is reported. At non relativistic energies the stopping power is dominated by the term  $1/\beta^2$  and decreases with increasing velocity until about  $v \sim 0.96c$ , where a minimum is reached[8]. Particles at this point are known as *minimum ionizing* particles or MIP. As the energy increases beyond this point, the term  $1/\beta^2$  become almost constant and  $dE/dx$  rise again due to the logarithmic dependence in Fig. 1.1.

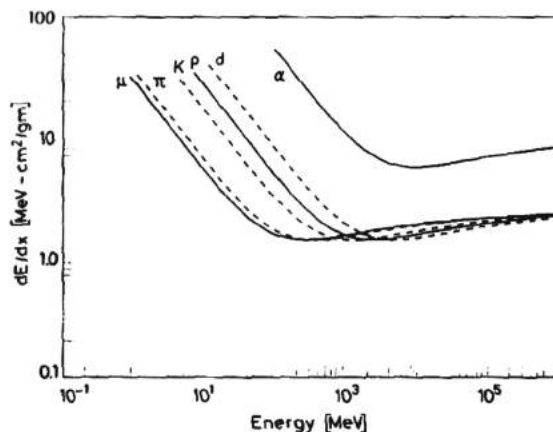


Figure 1.1: The stopping power as function of energy for different particles

However for energies below the minimum ionizing value, each particle exhibits a stopping power curve which, in most cases, is distinct from the other particle types.

### 1.1.2 The Bragg peak

A plot of the specific energy loss along the track, also known as *Bragg curve* for the case of an alpha particle of several MeV[10], is shown in Figure 1.2. For

most of the track, the charge on the alpha particle is equal to two electronic charges and the specific energy loss increases roughly of  $1/E$  as predicted by the Formula 1.1. Near the end of the track, the charge is reduced through electron pickup and the curve falls off.

In other hand, as depth of the material increases charged particles slow down. At some depth, depending on the type of particle and the their initial energy, the maximum energy (the Bragg peak) will be released.

Plots are shown in figure 1.2 both for single alpha particle track and for the average behavior of a parallel beam of alpha particles of the same initial energy. The differents is due to the effects of straggling between two curves.

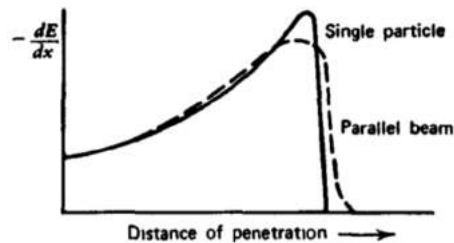


Figure 1.2: The specific energy loss along an alpha track

The microscopic interactions undergone by any specific particle vary somewhat randomly and its energy loss is statistical or stochastic. Therefore, a spread in energy always turns out after a beam of monoenergetic charged particles has passed through a given thickness of traversed material. The width of this energy distribution is a measure of energy straggling, which varies with the distance along the particles track.

The Figure 1.3 shows a schematic representation of the energy distribution of a beam initially monoenergetic particles at various points along its range.

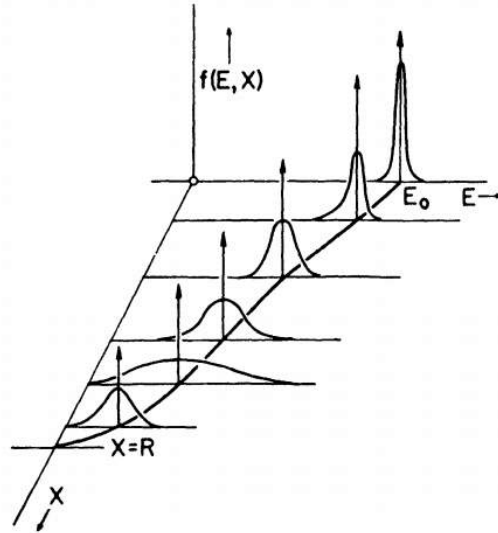


Figure 1.3: Plots of energy distribution of a beam of initially monoenergetic charged particles at various penetration distance  $x$ .

After the first part, the distribution becomes wider with penetration distance, showing the increasing importance of energy straggling. Near the end of the range the distribution narrows again because the mean particle energy has been greatly reduced.

The energy straggling introduces an error in the range determination, as well. The range is defined as the traveled distance by incident particle in the medium until it stops:

$$R(T) = \int_0^T \left(-\frac{dE}{dx}\right)^{-1} dE \quad (1.3)$$

where  $T$  is the incident particle kinetic energy.

The *range straggling* is defined as the fluctuation in path length for individual particles of the same initial energy. The same stochastic factors that lead to energy straggling at a given penetration distance, also result in slightly different total path lengths for each particles.

In order to evaluate the range it is possible to use the following operative approach: considering the *mean range* or the *extrapolate range*. The mean range is defined as the absorber thickness that reduces the incident particles

count to exactly one-half of its value in the absence of the absorber. This definition is most commonly used in tables of numerical range value. Another version, that appears in literature is the extrapolated range, which is obtained by extrapolating the linear portion of the end of the transmission curve to zero.

In the figure 1.4 it is represented a qualitative scheme of the two different approach.

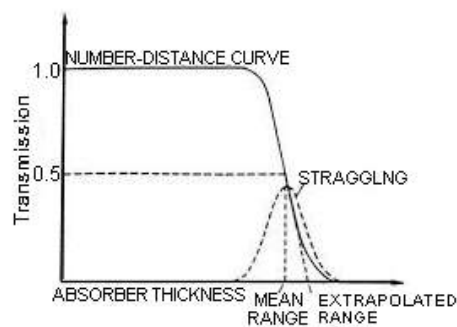


Figure 1.4: Typical range straggling trend of the incident particles in a material

In radiotherapy, the particles range estimation is a crucial factor in the definition of treatment plans. It is so often calculated with the help of algorithms based on the Monte Carlo method. In this context, another important factor is the dimension and the shape of the tumor. Once the geometrical characteristics of the tumor are outline, the energy and the type of particle are defined, the beam must cover the typical tumor entire extension. Usually the typical dimension of a monoenergetic beam has a diameter on the order of a few millimeters but the tumor dimension can have an extension of several centimeters. Indeed a strictly monoenergetic proton beam is unsuitable for cancer treatment because of its longitudinally narrow Bragg peak. On the other hand, it is necessary to spread out the Bragg peak to provide uniform dose within the target volume, by providing a suitably weighted energy distribution of the incident beam. The problem of producing a spread-out Bragg peak (SOBP) through a weighted collection of monoenergetic proton beams has been studied by various researchers[6].

In the figure 1.5 is shown a typical spread out Bragg peak.

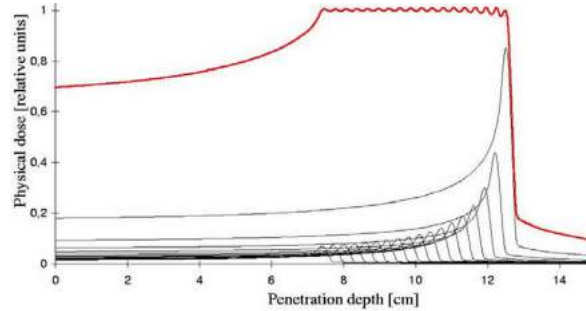


Figure 1.5: Spread Out Bragg Peak

## 1.2 Linear Energy Transfer

The concept of Linear Energy Transfer (LET) was introduced in the early 1950s to describe the quality of radiation and it represents the rate at which energy is deposited by the ionizing particles along their track. In such terms, LET and stopping power represent the same quantity. Nevertheless, the interest in discriminating between the energy transferred by the particle and the energy which is effectively deposited in the area of interest lead to the adoption of the term restricted linear collision stopping power[6].

In 1962 the International Commission on Radiation Units and Measurements (ICRU) introduced the adjective “locally” to the energy imparted to a medium, but, again, the definition was not quite strict and LET was not always used with the same meaning. Finally, in 1980, the ICRU defined LET as[11]:

$$L_{\Delta} = \left(\frac{dE}{dl}\right)_{\Delta} \quad (1.4)$$

where  $dl$  is the distance traversed by the particle and  $dE$  is the mean energy loss due to those collisions which have an energy transfer smaller than a specified energy cut-off value  $\Delta$ . For example,  $L_{\infty}$  means that all possible energy transfers are included and in this case the concept of unrestricted stopping power is used, while  $L_{100}$  means a cut-off value of 100 keV and it is referred to as restricted stopping power. In this case, those secondary electrons with more than 100 keV are not taken into account, as they leave

the volume of interest around the primary particle track. LET is usually expressed in  $\text{keV}/\mu\text{m}$ .

The unrestricted collision stopping power may be determined directly from experimental measurements of energy particles before and after passing through a thin absorber. Measurements of range in a material as a function of energy can also give approximate value of  $L_\infty$ .

Normally  $L_\Delta$  with a restricted value of  $\Delta$  is difficult to measure but it has been calculated for a variety of conditions (ICRU 1970).

LET, being a measure of the density of the ionization events along the particle track is strongly related to the amount of biological damage inferred by a certain kind of radiation to biological tissue.

Generally it is possible to divide the particles in two categories: Low-LET (as electrons and photons) and high-LET (as alpha particles, ions and neutrons) particles.

Radiation has different efficiency in damaging the DNA and this is related to the spatial distribution of their energy deposition. For example photons deposit energy homogeneously throughout the nucleus while ions deposit energy in localized sites of the cell nucleus. In particular, they deposit a very high dose in proximity of the particle track and essentially no energy in the areas between the tracks, leading to a very uneven distribution of the local dose. For this reason, same doses of carbon ions and X-rays have completely different effects at a biological level due to different events occurring at a microscopic level.

In accord to this peculiar effect if represents the LET dependence with the energy for different particles there are different trend, Fig. 1.6.

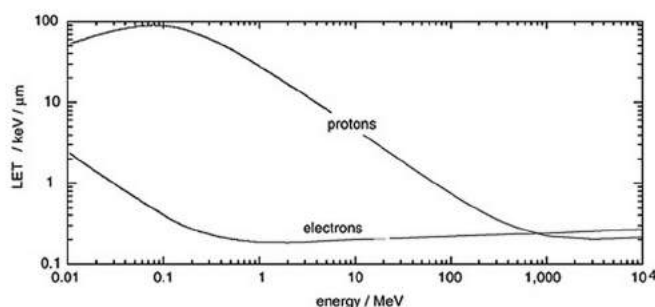


Figure 1.6: Linear Energy Transfert for protons and electrons

DNA damage can be direct, caused by the ion or its generated secondary electrons, or indirect, generated by radiation induced radicals. In particular:

1. Indirect effect: free radical generation, which being highly reactive, are the greater responsible for function loss or alteration of the cell. Even if short lived, free radicals can easily reach the nucleus of a cell and damage the nitrogenous bases of the DNA. In addition, their combination can generate  $H_2O_2$ , which is toxic for a cell. The damage caused by free radicals can be reflected even far off the origination point. Generally, free radicals are the main damaging byproducts of radiation. The presence of oxygen in the cell, can promote the origination of free radicals, and then less vascularized tissues are characterized by more resistance to radiation.
2. Direct effects: Radiation can directly affect the omeostasis of an organism by alteration of cellular functions. In particular they can modify the chromosome stock of a cell inducing apoptosis.

Several kinds of DNA damages can occur. In some circumstances isolated DNA lesions, like single strand breaks (SSBs), damaged bases, and abasic sites, which can be repaired efficiently. In other cases more closely spaced lesions, like double strand breaks (DSBs), two or more SSBs on opposing strands and other clustered damages, constituting lesions on both DNA strands, are considered to be significantly harmful. When a complex damage is inferred, chromosome aberrations and cell death will occur with more probability[5].

### 1.3 The dose concept

The biologic effect of a radiation is traditionally related to the amount of energy transferred to the irradiated volume and then, as above stated, it is often studied in relation to LET. The latter, however, only defines the linear transfer of energy but not the amount of it really absorbed by the medium.

In order to evaluate such parameter, the concept of *dose* is adopted. The dose express the mean energy dE transferred inside a unitary element of mass dm and volume dV and density  $\rho$ :

$$D = \frac{dE}{\rho dV} = \frac{dE}{dm} \quad (1.5)$$

According to the IS its unit of measure is the Gray (Gy), corresponding to the ratio Joule over kilogram.

A unit of measure related to the former one is the *dose rate*,  $\dot{D}$  expressed in gray per second and defined as:

$$\dot{D} = \frac{dD}{dt} \quad (1.6)$$

The absorbed dose is the sum up of the associated dose to the ionization product by the primary beam and by the secondary ions eventually produced by the fragmentation of the beam itself. In particular, when beams of charged particles run through targets it is possible to obtain a fragmentation of the target into ions of low atomic number.

As different radiations produce different biologic damage, the concept of *equivalent dose*, defined as the mean absorbed dose by a tissue for a specific kind and energy of the radiation is introduced

$$H_t = \sum_R W_R D_{T,R} \quad (1.7)$$

where D, T and R are the dose D absorbed in a tissue T from a radiation R. The term  $W_R$  is the radiation weighting factor defined by regulation that depending on the type of tissue.

## 1.4 Relative Biologic Effectiveness

The motivation for using heavy ions in particle therapy is twofold: firstly the Bragg peak dose deposition shape allows a more confined delivery of the dose in correspondence to the tumor volume, saving at the same time the surrounding healthy tissues. Secondly but even more importantly, the radiobiological properties of ion beams make them more efficient in inducing damage in carcinogenic cells[4]. By tuning the beam energy, the high-efficiency portion of radiation, which for carbon ions occurs at the end, can be confined in the tumor volume, limiting in this way the damage inferred to

the tissue in the entrance channel, where the biological effectiveness is lower. To describe radiation in terms of its efficiency, the relative biological effectiveness (RBE) has been introduced. It is defined as the ratio of X-ray dose to particle dose to produce the same biological effect, which can be chosen to be an endpoint of, for example, 10 % survival rate

$$R.B.E = \frac{D_{ref}}{D_{particles}} \quad (1.8)$$

The rationale behind comparing the particle dose to the photon dose is that most of the clinical experience is based on photon radiotherapy, therefore RBE correlates directly to dose depositions of photons and heavy-ion radiation, giving a measure of the difference between them.

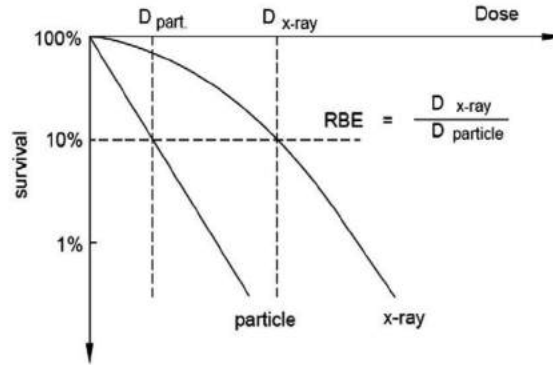


Figure 1.7: Qualitative RBE trend

The usual way to analyze the effects of different radiation types employs of cell survival curves[6]. The most common relation between cell survival probability (S, i.e. the fraction of surviving cells) and absorbed dose (D) is the so-called linear-quadratic (LQ) model, that aims to predict survival levels at different doses for different types of radiation (Fig. 1.7). According to the LQ model, RBE has an exponential linear quadratic dependence on dose, described by the relation:

$$FS = e^{-\alpha D - \beta D^2} \quad (1.9)$$

here:

- $\alpha$  represents the probability associated to lesions induced by a single track (SSB or DSB). It is expressed in  $Gy^{-1}$  and it is related to the initial slope, it is caused by repairable damage to the target and dominates the radiation response at low doses;
- $\beta$  is the probability for lesions introduced by two or more tracks. It is expressed in  $Gy^{-2}$  it represents the irreparable damage and causes the curve to bend at higher dose

The survival curve is represented in the figure 1.8:

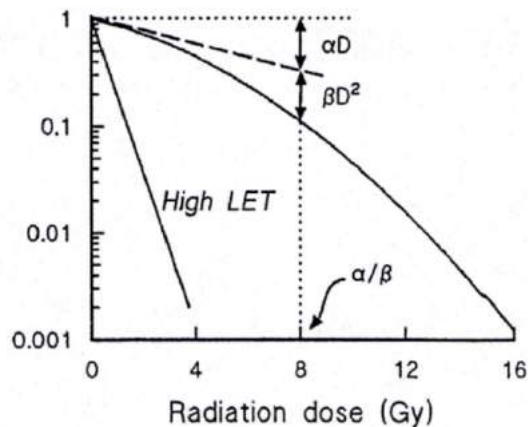


Figure 1.8: Linear-quadratic model typical trend. The term  $\alpha$  is the warp linear factor that identifying damage directly (for high LET radiation and low dose rate), while  $\beta$  corresponds to the quadratic curvature for damage to low LET radiation.

The shape of the curve is determined by the  $\alpha$  and  $\beta$  parameters, reflecting the kind of damage inferred to the cell. Low-LET radiation produces sparse lesions in the DNA, easy to repair via the cell repair mechanisms, while high-LET radiation damage is more difficult to repair. The increase of dose is related to a more complex cell damage: the shape of the linear-quadratic curve represents this trend. RBE is used in treatment planning as weighting factor to obtain the biological dose ( $D_{bio}$ ), as the physical dose ( $D_{phys}$ ) alone does not consider the response of biological tissues to the radiation:

$$D_{bio} = RBE \cdot D_{phys} \quad (1.10)$$

The  $D_{bio}$ , on the other hand, instead, for the increase of the biological effectiveness of ion beams towards the Bragg peak.

The main physical parameters which characterize RBE are the ion species, the beam energy, the dose and the LET, while the main biological ones are the tissue type, the repair capability of the cell, the level of oxygenation of the tissue. Due to its complex and multiple dependencies, RBE is not an easy quantity to evaluate experimentally: for this reason, the application of different biophysical models is necessary in treatment planning.

As RBE changes not only along the depth dose curve but also for the various ion species with different LET values, RBE is often given as a function of LET as is showned in Fig 1.9:

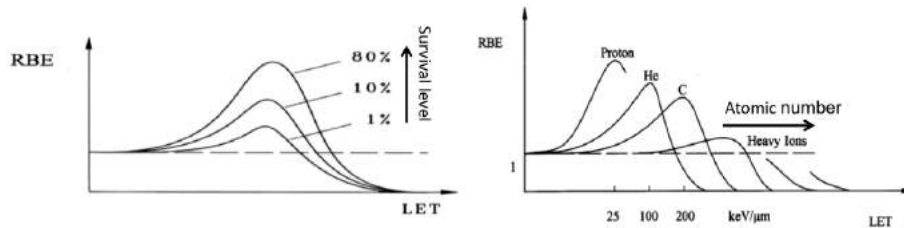


Figure 1.9: RBE as function of LET for a fixed atomic number: because of the dose dependence, RBE differs for different survival levels (left). Schematic comparison of RBE for different atomic numbers: for heavier ions the RBE maximum is shifted to larger LET values and decreased in height (right)

RBE increases with LET until it reaches a maximum, corresponding to the optimum LET value. After this point, a further increase of LET will not be anymore beneficial to cell killing and the excessive energy will not produce any cell damage.

Because of the dependence of RBE on dose, the fraction of survival has to be specified. RBE also depends on the particle type (Fig. 1.9, right): with the increase of the atomic number, the RBE maximum decreases and shifts to bigger LET values. These two dependencies show that the particle track

plays a role in the biological efficiency of the various ions, because not only the initial energy, but even more importantly the particular way the particle interacts with matter, counts.

Another important element linked with the tissue quality is the repair capability. Tissues with high repair capacity have higher RBE maximum compared to those which have a lower repair capacity, Fig. 1.10

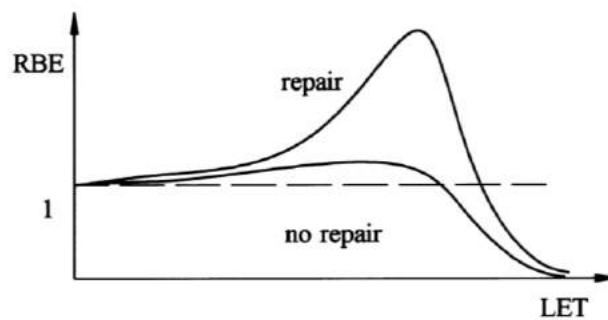


Figure 1.10: RBE as function of the linear energy transfer for cells with normal and reduced repair

This aspect has to be considered accurately in the treatment planning, as usually various tissues with different repair capacities are present. Moreover, also different endpoints are required, to guarantee an high efficiency of cell killing in correspondence of the tumor and a sparing of the surrounding healthy tissues

## 1.5 The traditional accelerators machines

Planning and building a modern accelerator facility for application in medical physics must rely on the extremely accurate control of the beam. This aspect is critical for the safety patient and effectiveness treatment[15].

Although originally built only for nuclear physics purpose, accelerator machines of charged particles are becoming increasingly more common in hospital centers. Since the first cathode ray tube used to produce X-rays, we can now rely on complex machines, from electrons accelerator for conventional

radiotherapy to protons and ions accelerators for the treatment of several neoplastic diseases. In the context of hadrontherapy, charged particles are accelerated using cyclotrons and synchrotrons. Nowadays, more than 60 hadrontherapy centers are active in the world, see Fig. 1.11.

Particle Therapy Patient Statistics (per end of 2013)

COUNTRY	WHERE SITE	PARTICLE	FIRST (-LAST) PATIENT	PATIENT TOTAL	DATE OF TOTAL
Belgium	Louvain-la-Neuve	p	1991 (-1993)	21	1993
Canada	Vancouver (TRILUMF)	n	1979 (-1984)	367	1994
Canada	Vancouver (TRILUMF)	p	1995	175	Dec-13
Czech Rep.	Frag (FTCCZ)	p	2012	140	Dec-13
China	Wanjie (WPTC)	p	2004	1076	Dec-13
China	Lanzhou	C ion	2006	213	Dec-13
England	Clatterbridge	p	1989	2446	Dec-13
France	Nice (CAL)	p	1991	4936	Dec-13
France	Orsay (CFO)	p	1991	6432	Dec-13
Germany	Darmstadt (GSI)	C-ion	1997 (-2009)	440	2009
Germany	Berlin (HM)	p	1996	2312	Dec-13
Germany	Munich (RPTC)	p	2009	1811	Dec-13
Germany	HIT, Heidelberg	C ion	2009	1368	Dec-13
Germany	HIT, Heidelberg	p	2009	503	Dec-13
Germany	WPE, Essen	p	2013	32	Dec-13
Italy	Catania (INFN-LNS)	p	2002	293	Nov-12
Italy	Pavia (CNAO)	p	2011	76	Dec-13
Italy	Pavia (CNAO)	C ion	2012	105	Dec-13
Japan	Chiba	p	1979 (-2002)	145	2002
Japan	Tsukuba (PMRC, 1)	p	1983 (-2000)	700	2000
Japan	Chiba (HIMAC)	C ion	1994	8073	Dec-13
Japan	Keshiwa (NCC)	p	1996	1226	Mar-13
Japan	Hyogo (HIBMC)	p	2001	4223	Dec-13
Japan	Hyogo (HIBMC)	C ion	2002	1935	Dec-13
Japan	WERC	p	2002 (-2009)	62	2009
Japan	Tsukuba (PMRC, 2)	p	2001	2967	Dec-13
Japan	Shizuoka	p	2003	1590	Dec-13
Japan	Koriyama-City	p	2006	2306	Dec-13
Japan	Gunma	C ion	2010	995	Dec-13
Japan	Ibusuki (MMRI)	p	2011	919	Dec-13
Japan	Fukui City (Prefectural Hospital)	p	2011	426	Dec-13
Japan	Nagoya PTC, Nagoya, Aichi	p	2013	199	Dec-13
Japan	Tosu (Sega-HIMAT)	p	2013	62	Dec-13
Poland	Krakow	p	2011	39	Dec-13
Russia	Dubna (1)	p	1967 (-1996)	124	1996
Russia	Moscow (ITEP)	p	1969	4320	Dec-13
Russia	St. Petersburg	p	1975	1386	Dec-12
Russia	Dubna (JINR, 2)	p	1999	990	Dec-13
South Africa	Themba LABS	p	1993	621	Dec-13
South Korea	Ilsan, Seoul (NCCR)	p	2007	1286	Dec-13
Sweden	Uppsala (1)	p	1957 (-1976)	73	1976
Sweden	Uppsala (2)	p	1989	1356	Dec-13
Switzerland	Villigen PSI (Pion)	n	1980 (-1993)	503	1993
Switzerland	Villigen PSI (OPTIS 1)	p	1984 (-2010)	5458	2010
Switzerland	Villigen-PSI, incl OPTIS2	p	1996	1581	Dec-13
USA, CA.	Berkeley 184	p	1954 (-1957)	30	1957
USA, CA.	Berkeley	He	1957 (-1992)	2054	1992
USA, NM.	Los Alamos	n	1974 (-1982)	230	1982
USA, CA.	Berkeley	ions	1975 (-1992)	433	1992
USA, MA.	Harvard (HCL)	p	1981 (-2002)	9116	2002
USA, CA.	Loma Linda (LLUMC)	p	1990	17829	Dec-13
IN., USA	Bloomington (MPRI, 1)	p	1993 (-1999)	34	1999
USA, CA.	UCSF - CNL	p	1994	1621	Dec-13
USA, MA.	Boston (NPTC)	p	2001	7345	Dec-13
USA, IN.	Bloomington (IU Health PTC)	p	2004	1927	Dec-13
USA, TX.	Houston (MD Anderson)	p	2006	4748	Dec-13
USA, FL.	Jacksonville (JFPTI)	p	2006	5085	Dec-13
USA, OK.	Oklahoma City (ProCure PTC)	p	2009	1354	Dec-13
USA, PA.	Philadelphia (UPenn)	p	2010	1750	Dec-13
USA, IL.	CDH Warrenville	p	2010	1329	Dec-13
USA, VA.	Hampton (HUPTI)	p	2010	767	Dec-13
USA, NY.	New Jersey (ProCure PTC)	p	2012	512	Dec-13
USA, WA.	Seattle (SCCA ProCure PTC)	p	2013	86	Dec-13
USA, MO.	St. Louis (S. Lee King PTC)	p	2013	1	Dec-13

Figure 1.11: Statistics summary on patients treated in all hadrontherapeutic centers of the world

The choice of the kind of accelerator to be used depends on the kind of particles that must be accelerated in order to reach the tumoral mass.

Cyclotrons can produce a very highly stable intensity beam, which can be tuned but energy can't be changed while the machine is on. The variation energy can be obtained by introducing passive elements which can down-regulate the beam along the transport line.

Instead synchrotrons, can change the energy released from pulse to pulse but need an injector for the extraction, and are more complex overall[14].

A crucial aspect of hadrontherapy is the fragmentation of accelerated lighter ion. These particle have a lower charge and can ionize the molecules of the cell planted beyond the tumor. Allowing to overcome Bragg peak and produce a tail in the dose distribution. In relation to this aspect, it is necessary to keep into account the intensity of the emitted beam, which can depends on the duration of the treatment, the dose, the beam modulation, and the shape and position of the tumor. In order to minimize the effects of the patient's movement during treatment, the exposure to the beam should not last more than a minute. For this reason, the intensity of the beam at the exit of an accelerator should be higher than the one expected for treatment, for loss due to efficiency transport from the machine to the patient.

By considering all of these aspects, cyclotrons are favored for protons production, while synchrotrons are used generally for ion beams generation. In both cases, these are very expensive and large machines, which make these kind of treatments unaffordable to anyone.

During the last years, the main effort of research has focused on the study and realization of increasingly more efficient accelerators, in order to reduce the costs and the size of such machinery. An innovative approach to particle acceleration could be the use of laser-driven technology, which can produce hadronic beams as result of laser-target interactions. Thanks to these kind of machinery, it could be possible to realize *gantry* more suitable and cheaper, allowing to turn around the patient as it already happens in conventional radiotherapy using linear accelerators (LINAC)[16].

## Chapter 2

### The ELIMED project

In the previously discussed economic and social context, the ELIMED project, was started on 2011. ELIMED, acronym for ELI-beamlines MEDical and multidisciplinary applications, starts as a collaboration between the European Southern National Laboratories of the National Institute of Nuclear Physics of Catania (LNS-INFN) and the Academy of Sciences of the Czech Republic-Prague fyzika Instar (ASCR-FZU).

The project proposes the design, development and realization of a complete transport beam line, including its diagnostics and dosimetric devices, for optically accelerated ion beams[12].

In addition, the realization of an ultra high-intensity, high repetition-rate, femtosecond laser facility whose main goal is the generation and the applications of high-brightness X-ray sources and accelerated charged particles in different fields is planned. Particular care will be devoted to the potential applicability of laser-driven ion beams for medical treatments of tumours. Such kind of beams shows very interesting peculiarities and, moreover, the laser-driven based accelerator can really represent a competitive alternative to the conventional machine since they are expected to be more compact in size and less expensive. In the figure 2.1 is showed the scheme of the layout of ELIMAIA experimental hall that will be realized in Prague[20].

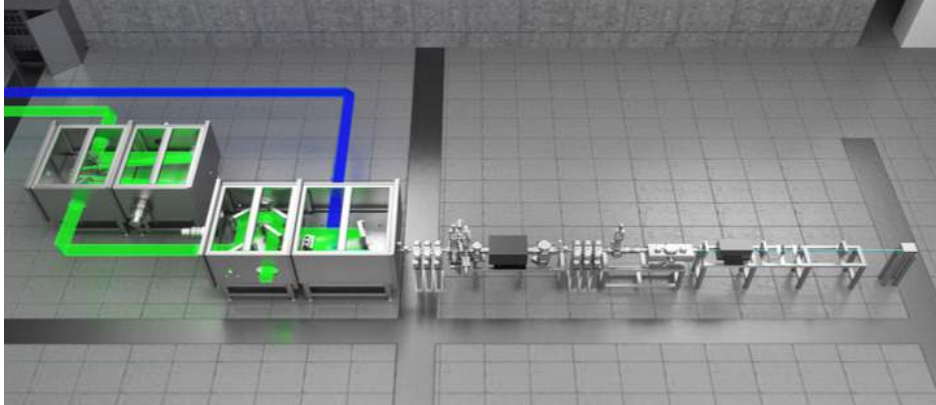


Figure 2.1: ELIMAIA experimental hall

The ELIMED transport beam-line and its dosimetric systems, will be installed at the ELI-Beamlines facility in Prague within 2017. The beamline will be mounted, inside the ELIMAIA (ELI Multidisciplinary Applications of laser- Ion Acceleration) experimental hall. The beam-line will be composed by two sections: one in vacuum, devoted to the collecting, focusing and energy selection of the primary beam and the second in air, where the dosimetric devices will be installed (see the Fig. 2.2). The scheme of the facility project is mainly divided in three packages:

1. Ion beam collection and diagnostic;
2. Ion beam selection, transport and diagnostics;
3. Dosimetry and sample radiation system.

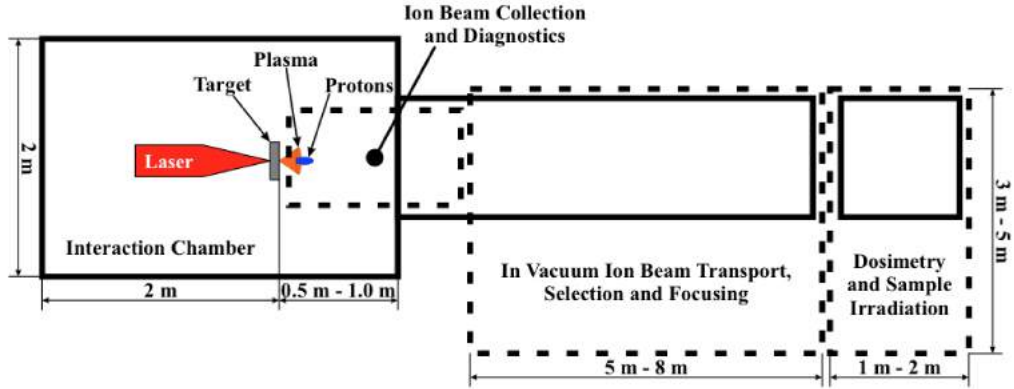


Figure 2.2: Simplified scheme of the Laser Driven Ion Beamline for Multi-disciplinary Applications showing the estimated physical length and width of the three different sections: (i) ion Beam Collection and Diagnostics; (ii) in-Vacuum ion Beam Selection, Transport and Diagnostics; (iii) Dosimetry and sample Irradiation

The realisation time schedule divided in four phases:

- Preparatory phase: the final design of the transport beam-line, from the target to the irradiation point will be realized, even if no laser beam will be available at the ELI-Beamlines facility.
- First phase: according to already performed Particle in Cell simulations, protons up to 20-30 MeV will be produced;
- Second phase: proton beams with energies up to 60 MeV will be produced;
- Third phase: proton beams with energies up to 100 MeV will be generated from the laser- target interaction. The transport beamline will be working at their maximum performances, the dosimetric systems will be commissioned and the final radiobiological tests will be realized.

In order to deliver beams with different energies, species and energy spreads, a target to the irradiation point, a quadrupoles system and an energy selector system for the transport, the handling and the refining energy selection of the initial beam will be realized [7].

The diagnostics will be guaranteed by a Thompson spectrometer, with tunable electric and magnetic fields and by different detectors in Time of Flight (ToF) configuration. Downstream, downstream an integrated system will permit the relative and absolute dosimetry with an accuracy of few per cents in order to assure the basic condition for the medical application. The main idea for the dosimetric system is to use a Faraday Cup coupled with other detectors, like CR-39 and GafChromic. The crucial goal of the whole beamline is the control, the stability and the reproducibility shot-to-shot of the output beam in terms of energy, flux and dose.

In the present paragraph the transport beam line and the selection system will be described. The development and the realization of the detector for the absolute and relative dosimetric system and the diagnostic system for the beam will be illustrated, as well.

## 2.1 The ELIMED transport beamline: Collecting, focusing and selection system

In contrast to conventional accelerators the combination of very high peak currents with extremely low emittance, makes laser-driven beams unique with the perspective of compact accelerator development for several applications. The laser-driven beams are usually characterized by a huge energy spread and a large angle of emission, though the source dimension keeps very small (about tens of microns).

The energy particles spectra changes from a minimum energy (few KeV) to a maximum that depends on the electric fields in expanding plasma process[21]. Even the spatial distribution depends on the particles energy.

The focus and the selection process of the beams produced in the laser-matter interaction is characterized by the following steps:

1. Initial phase of capturing and collecting;
2. Beam focusing and transport;
3. Selection energy system;

The initial phase of capturing and collecting charge starts close to the production point of the charged particles. The aim of this selection of the beam

transport line is to collect the largest fraction of particles so that to reduce the beam angular divergence. Thanks to this system it is possible to carry out the first beam energy selection. The first part is a set of four NdFeB permanent magnetic quadrupoles (PMQs), located just downstream the target and having the main function to reduce the divergency of the primary beam and to perform its collection and preliminary energy selection. In detail, the four PMQs have been realized to allow an efficient proton beams transport with energies ranging from 1 MeV up to 30 MeV. Each quadrupole has an external radius of 60 mm and an internal bore of 20 mm. Two of them have a longitudinal length of 40 mm and 80 mm with a maximum field gradient value of 110 and 114 T/m, respectively. In the Figure 2.3 is reported the detailed characteristics of the quadrupole magnetic flux density.

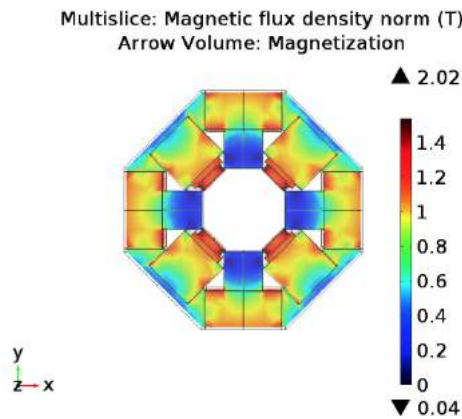


Figure 2.3: Magnetic flux density.

The final beam energy refinement will be performed by means of a second transport device prototype: an energy selection system, able to select particles with energy up to 100 MeV[7]. The energy selection is the most critical part of the entire beam transport system because, as mentioned above, particles emitted with a very wide energy spectrum by the laser-material interaction. In order to use a beam for medical applications the emitted particle energy must be accurately selected. National Laboratories of the South, has already designed and built a first prototype energy selection system characterized by a magnetic system consisting of a series of permanent-magnets

dipoles producing an alternating gradient magnetic field of 0.85T each (Figure 2.4).

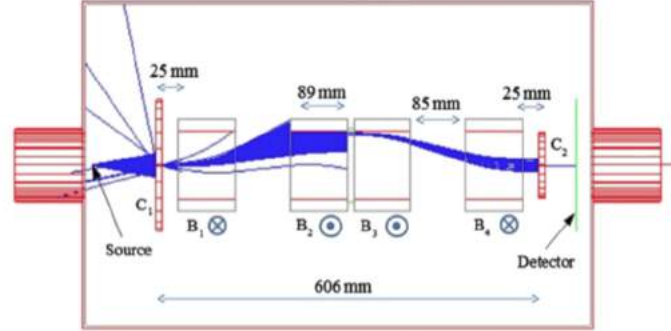


Figure 2.4: Scheme of the protons trajectory in the Energy Selection System: in the figure C1 and C2 are the collimators.

In such configuration, according to the Lawrence force, the beam is radially defocused in the first two dipoles. In this way it is possible to achieve a quiet good separation between the particles trajectories for the different energies at the exit of the second deflecting sector and to stop all the others. The particles passing through the collimator are then refocused by the opposite gradient of the third and fourth dipole magnet fields. In particular, the first two dipoles allow to radially defocusing the beam increasing the separation between the trajectories of particles at different energies, near the central gap between the second and the third magnet. Here, by means of a moving collimator, the particles energy is selected. The second pair of dipoles then refocuses the beam. Considering the natural divergence of laser-produced beams, two additional collimators are placed both upstream and downstream the selection system. The first one allows to avoid spatial mixing of particles with different energies inside the device, the second one ensures a more precise selection. The energy spread and the amount of particles passing through the slit depends on its aperture size. A roller guide system, placed in the central twin magnet position, allows the moving of the two magnets in the radial direction in order to increase the transverse displacement and to select the lowest energy particle component. In such a way, it is possible to choose the energy in a range between 1 MeV to 60 MeV.

## 2.2 Diagnostics of laser-accelerated ion beams

The laser-generated plasma, in non-equilibrium condition, has peculiar properties strongly depending on the laser parameters and on the target composition and geometry.

The investigation of fast ion emission is a crucial point for the using of the laser accelerated ion beams instead of the beam obtained by traditional acceleration technique. Actually various difficulties in such diagnostic methodologies exist when high - energy laser pulses are used, among which: high electromagnetic noise, overlapping of the signal due to photopeak and difficulties in separation of the ion signals. In order to overcome these problems the development of new detector is growing in the last years.

Different fast diagnostic techniques can be employed for the plasma characterization in term of particles and photon emission, plasma temperature and density, ion energy distribution, angular emission, yield and electric field acceleration. In this context, the ELIMED project is devoted to develop a fast diagnostic system in real time that produced several advantages respect to the ex situ diagnostics that allow to evaluate the data only at the end of the experiment[21]. Generally, these diagnostics are classified into two categories: energy spectrometers and time-of-flight detectors. The main characteristics of the first is that the signal produced is capable to provide the plasma ion energy distribution while thanks to the second detectors it is possible to provide information correlated with the velocity and the intensity of the particles. In particular, as ToF detectors it is possible to use various devices, such as semiconductor detectors, e.g. silicon carbide (SiC) and diamond. In order to distinguish the plasma charged particles from the UV/X-rays these detectors should be placed in a far distance from the target where the time gap these two different plasma products is significant. The different technique of particle detection that will be used in ELIMED project will be explained in the following paragraphs.

### 2.2.1 Thompson Parabola Spectrometer

One of the most interesting detectors in the characterization of charged particles produced by laser-target interaction is the Thomson spectrometer.

Information on energy, momentum and charge to mass ratio of particle beams can be provided by a Thomson Parabola spectrometer, widely used to study

ion sources such as ion accelerators, laser produced plasma, etc. In such a device charged particles are deflected by parallel electric and magnetic fields[24]. The electric deflection depends on the energy of particles while the magnetic deflection depends on their momentum; moreover particles with different charge to mass ratio are deflected on different trajectories.

Its principle of operation is based on the Lorentz force and, in particular, the use of electric and magnetic fields that deflect the particles (Figure 2.5).

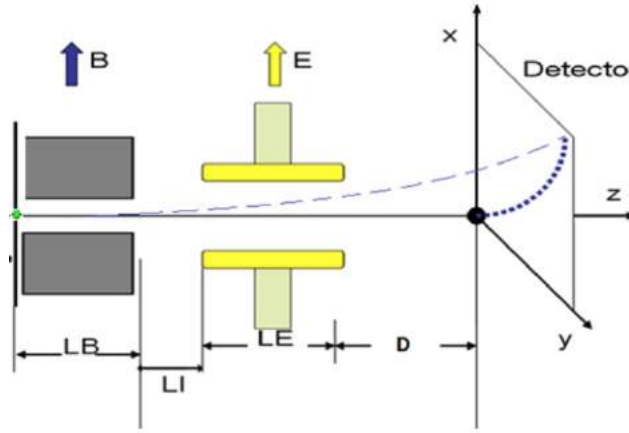


Figure 2.5: Scheme of the Thomson parabola spectrometer. The blue line represents a typical particle trajectory on the detector plane.

The Lorentz force can describe the motion of a particle:

$$\vec{F} = q(\vec{E} + \vec{v} \wedge \vec{B}) \quad (2.1)$$

Assuming that both fields are uniform over a length  $L$  and zero outside. Since the fields are parallel, the deflections are orthogonal to each other and the deflections are proportional to the deflection angle by means of the drift length between the electromagnetic device and the detector plane  $D$ .

Thus assuming that the magnetic field deflects on the  $x$  axis and the electric field deflects on the  $y$  axis, from the above equations one gets:

$$y = \frac{qELD}{2T_{kin}} \quad (2.2)$$

$$x = \frac{qBlD}{\sqrt{2mT}} \quad (2.3)$$

where  $q$ ,  $m$  e  $T$  are respectively the charge particles, the mass and the kinetic energy ions. Solving the second equation for  $v$  and replacing it in the first one we get the parabolic equation:

$$x^2 = \frac{q}{m} \frac{B^2 l D}{E} y \quad (2.4)$$

which means that particles with the same charge-to-mass ratio and different energies are deflected on a parabolic trace on the detector plane. The previous equation shows that a TP provides a separation of all ion species and charge state according to their  $q/m$ . Every single parabola on the detector belongs to a different ion charge-to-mass state ratio. Thus knowing the charge-to-mass ratio and the charge state it is possible to get the ion mass and to identify the ion species[25].

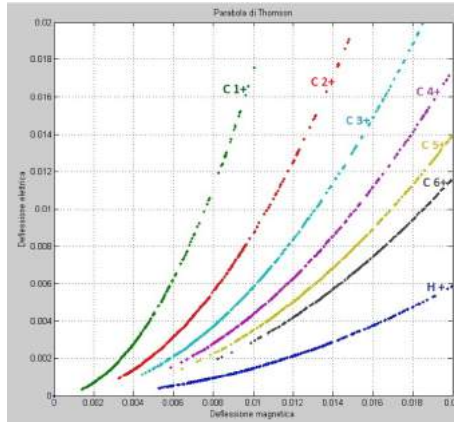


Figure 2.6: Simulation of a particle beam laser product of the interaction with a target of  $CH_2$

A first prototype of Thompson Parabola spectrometer able to resolve protons up to 20 MeV has been already developed at Southern National Laboratory of INFN and successfully tested. It represents a prototype to realize a more performing detector suitable for diagnostic of high energy, up to 250 MeV, laser driven proton beams. In order to fulfill the requirements of high spatial

resolution and relatively small dimension for this first prototype, its deflection sector is made of partially overlapped electric and magnetic field. Two 7 cm long copper electrodes with a gap of 2 cm generate the electric field. The overall potential difference on the electrodes can be varied from 0 to 20 KVolt[26]. The magnetic field is produced by an electromagnet made of two resistive coils and H-shaped iron. The current on the coils can reach at maximum value about 86 A corresponding to a maximum magnetic field value of 0.25 T.

### 2.2.2 Time Of Flight detectors (ToF)

Detectors in time of flight configuration are widely used in laser-plasma experiments. Thank to this technique it is possible to obtain information on particles emitted from the knowledge of their speed [28]. The most direct way to determine the particle speed is, of course, by measuring the time that it takes to travel a certain distance. Particles with the same momentum but different masses travel with different velocities; therefore from the knowledge of the momentum and the time of flight (ToF)  $t$ , across a known distance  $L$  the particle can be identified. The measured time  $t_{TOF}$  has to be corrected onto this distance as:

$$t = t_{TOF} + \frac{L}{c} \quad (2.5)$$

where  $c$  is the speed of light and  $L$  is the distance from the point where the particle is emitted to detector. Considering the previously equation, the particle velocity is, of course:

$$v = \frac{L}{t} = \frac{L}{t_{TOF} + L/c} \quad (2.6)$$

In a typical laser-plasma experiment, ToF detectors are located at a distance from the target such that the time gap between different two or more peaks is significant and hence measurable. Assuming the laser pulse length is much shorter than the sampling rate of scope (wherewith signal is acquire) it is possible to consider all the laser-plasma products as created in the same moment. So the particle energy from the ToF measurement is obtained from:

$$E = \left( \frac{1}{\sqrt{1 - \frac{v^2}{c^2}}} - 1 \right) m_0 c^2 \quad (2.7)$$

expressed in the relativistic form.

### Semiconductor detectors: Silicon Carbide and Diamond

In many radiation detection application, the use of a solid detection is of great advantage. For the measurement of high-energy electrons or gamma rays, detector dimensions can be kept much smaller than the equivalent gas-filled detector because solide densities are about 1000 times greater than for a gas. Furthermore these detectors have high energy resolution, low supply voltage and high response time.

The detection is based on the production of one the electron-hole pair when a particle pass through the material. The periodic lattice of crystalline materials establishes allowed two energy bands for electrons that exist within the solid. The lower band, called the valence band, corresponds to those outer - shell electrons that are bound to specific lattice sites within the crystal. While the next higher - lying is called the conduction band and represents electrons that are free to migrate through the crystal. The two bands are separated by the bandgap, the size of which determines wheter the material is classified as a semiconductor, conductor or insulator.

Due to the excitation process an electron passes in the conduction band from valence band and it leaves a vacancy called a hole. Mostly, there are two process that produce an electron-hole pair: thermal excitation and the passage of particle in the lattice. A good semiconductor detector requires a band gap wide enough to have the least thermal noise current (leakage) and small enough to have the highest particle signal. In this context, the Silicon Carbide (SiC) and diamond detectros (CVD) exhibit both a good bandgap respectively up to 3.2 eV and 5.5 eV[27, 30].

Both SiC and CVD are semiconductor detector, the first constituted by one junction realised with two regions doped while the second is an intrinsic semiconductor. In order to maximise the charge collection is typically applied voltage from several tens to few thousands volts. The reverse bias generates a high electric field region in the semiconductor, depleted by the

charge carriers. Photons and particles impinging such detector are interacting with the semiconductor lattice so generating a number of electron-hole pairs proportional to their energy.

The charge carriers, generated inside the high field region, drift toward the detector's anode (in case of electrons) and cathode (in case of holes), respectively, producing a current pulse at the electrodes.

A typical production of many electron-hole pairs along the track of the particle in a semiconductor detector with one single junction is shown in the Figure 2.7.

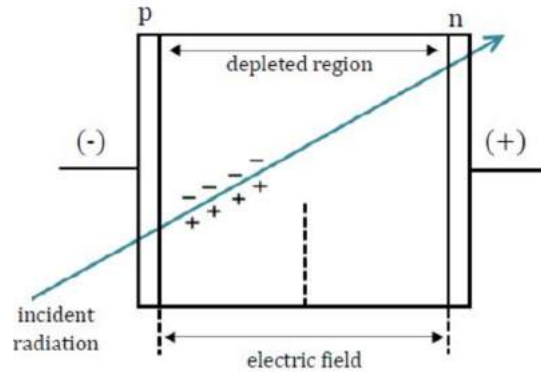


Figure 2.7: Scheme of semiconductor detector with one junction

A charge amplifier connected to the anode or cathode is used to integrate the current pulse. The amplitude of the step-like output voltage is proportional to the collected charge and also to the radiation energy. For this reason the energy spectroscopy is feasible for photon/particle counting.

With a set of simplifying assumptions, analytic expression can be obtained for the expected pulse shape signal for a simple geometrical configuration planar[10]. In general, the energy  $dE$  absorbed by the motion of a positive charge  $q_0$  through a potential difference  $d\varphi$  is given by

$$dE = -q_0 d\varphi \quad (2.8)$$

In term of the electric field  $\varepsilon(x) = -d\varphi(x)/dx$

$$\frac{dE}{dx} = q_0 \varepsilon(x) = q_0 \frac{V_0}{d} \quad (2.9)$$

where  $V_0$  is the applied voltage and  $d$  is the active region that for single crystal detector correspond to the detector thickness. So the energy absorbed by the motion from  $x_0$  to  $x$  is

$$\Delta E = \int_{x_0}^x dE = \frac{q_0 V_0}{d} \int_{x_0}^x dx = \frac{q_0 V_0}{d} (x - x_0) \quad (2.10)$$

and the signal voltage is

$$\Delta V_R = \frac{\Delta E}{C V_0} = \frac{q_0}{C} \frac{(x - x_0)}{d} \quad (2.11)$$

This voltage corresponds to an induced charge of

$$\Delta Q = C \Delta V_R \quad (2.12)$$

The development of the signal pulse can thus be represented by the growth of a time-dependent induced charge  $Q(t)$ . There are two separate components of the induced charge, one corresponding to the motion of the electrons and the other to the motion of the holes. It is possible to write this combination as:

$$Q(t) = q_0 \left( \frac{v_e}{d} t_e + \frac{v_h}{d} t_h \right) \quad (2.13)$$

where  $v_e$  and  $v_h$  are the drift velocity while  $t_e$  and  $t_h$  are the drift time for the electron and hole respectively.

Silicon Carbide is a special case of semiconductor junction with outstanding physical properties for manufacturing detectors of ionizing radiation such as alpha, electrons, protons, X and gamma rays. The wide band gap, high saturation velocities of the charge carriers, high breakdown field, high thermal conductivity and its radiation hardness, allow low-noise production and reliable operations in environments which are critical or forbidden to other semiconductor detectors. In particular, recent works have been done on the development of SiC radiation detectors and on the characterization of their performances. SiC detectors were used with excellent results as neutron [31] and X-ray detectors operating at high temperatures [32]. The charged-particle response characteristics have been measured by irradiating the detectors with alpha particles, protons, neutrons, ions and gamma rays obtaining promising results. For these reasons this particular semiconductor detector

seems to be the ideal for the diagnostic system accelerator laser driven ion beam.

Then again, Diamond detectors were tested (along with SiC) detecting a large number of particles such as alpha, neutrons, electrons, ions and protons. This detector has shown good results and high resistivity to radiation damage.

Diamond is usually cited as the hardest material known, and defines one extreme of the empirical Moh scale of hardness. This means that diamond detectors are not easily scratched and is a distinct advantage. The hardness is a consequence of the rigidity of the diamond lattice which also affects the physical properties in many other ways. For example, in combination with the low atomic mass of carbon, it leads to the highest Debye temperature of any material (2230 K). Also reflecting the extreme stability of diamond, the melting point is 4363 K and the highest thermal conductivity, the highest of any known substance[27].

The electrical properties are determined largely by its bandgap of 5.45 eV, which is so much larger than typical energies at room temperature that the pure or ‘intrinsic’ material has a resistivity in the region  $10^{13}$ – $10^{16}\Omega cm$ , making it in electrical terms an insulator, but it is often referred to as also a semiconductor because of the close similarity to conventional semiconductors like silicon and germanium.

A diamond detector can be artificially produced by the ‘chemical vapour deposition’ process (CVD): typically a thin layer of the material is gradually built up by deposition on a suitable substrate from a gas phase containing hydrocarbon gases and hydrogen at low pressure.

In the next table is shown some characteristics of the two different detectors.

	<b>4H-SiC</b>	<b>Diamond</b>
<b>Bandgap at 300K [eV]</b>	3.26	5.45
<b>Max. operating temperature [°C]</b>	1200	1100
<b>Electron mobility [<math>10^{-4} m^2/Vs</math>]</b>	900	2200
<b>Hole mobility [<math>10^{-4} m^2/Vs</math>]</b>	40	1600
<b>Dielectric constant</b>	10	5.5
<b>Breakdown electric field [<math>10^8 V/m</math>]</b>	2.2	10

Figure 2.8: Principal characteristics of SiC and diamond detector

## 2.3 Relative and absolute dosimetry of laser-accelerated ion beams

Due to the particular characteristics, broad energy spectra and extremely high dose per pulse, dosimetry of the optical accelerated beams available nowadays is extremely challenging.

For this reason the development and the characterization of a set of dedicated detectors for dosimetry are necessary in order to select the most appropriate ones and to design a customized dosimetric system; An independent absolute dosimetry and an online relative dose monitoring system are crucial for successful radiobiological and dosimetric experiments with such kind beams. Different detectors are in developing and tests are performing around the world to achieve this task. The ELIMED project is devoted to develop and test different detectors for absolute and relative dosimetry[22]. So far different preliminary test to using radiochromic films and CR-39 for relative dosimetry have been carried out an innovative Faraday Cup (FC) for absolute dosimetry was developed and tested, as well.

The radiochromic films and CR-39 can be used as single detector or in a stack configuration in order to have quantitative information on the energy spectrum of the accelerated protons. An accurate measurement of the energy spectrum is, in fact, necessary for a precise calibration of the FC.

The following is a brief description of the RCF and CR39 detectors. The use of Faraday cup for absolute dose measurements will be extensively treated in the next chapter.

### 2.3.1 Radiochromic Film

In radiation dosimetry it is important to measure the absorbed dose and the dose-profile of the radiation, in order to understand how radiation losses energy thought matter. Indeed, the purpose of dosimetry in medical application is also the measure of the Bragg peak depth, connected to particle energy and spread[32].

Radiochromic films are frequently used for dosimetry measurements in radiation oncology thanks to their specific characteristics as:

1. low energy dependence,

2. high spatial resolution (of the order of tens microns)
3. water-equivalence.

The film sensitive layer is located on a solid solution of colourless crystalline deacetylene monomer (sensitive component) coated on a flexible film base. When the active component is exposed to radiation, it reacts to form a blue colour polymer. The change in optical density, following a dose deposition in the Gafchromic films, may be measured with transmission densitometers, film scanners or spectrophotometer. A simple analysis of the irradiated film can be obtained by using flatbed RGB scanners in the red channel.

Recent experimental studies have demonstrated a clear independence of Gafchromic response from the dose rate. This characteristic is obviously essential, especially for the highly pulsed laser driven proton beams. Different model of RCF are available according to different dose sensitivity and dimension: Gafchromic HD-V2, GafChromic MD-V3, GafChromic EBT3. In particular, GafChromic EBT3 and HD-V2 has been developed specifically for applications in conventional radiotherapy and protontherapy.

### 2.3.2 CR39

These detectors are especially useful for registration of heavy charged particles of energy ranging from tens of keV up to several hundreds of MeV. The CR-39 revealed very high sensitivity and uniformity of response and appeared to be especially suitable for protons, deuterons and alphas detection. The plastic track detector is a  $C_{12}H_{18}O_7$  polymer with density  $1.3g/cm^3$ . Charged particles are registered directly and the tracks on the detector became visible after etching (fixing some parameters like temperature, duration and chemical element for eaching processand) and investigated them using a microscope. In particular, the chemical treatment transform the material damages into permanent structures called ion track which can be analyzed using dedicated software.

In general the investigation of yields for reaction from thick samples is difficult, because charged particles come to the detector with a large energy spread and their tracks have different diameters. The main parameter of track detector is the ratio of etching rates at the start of the track and at the end of the track because this is a function of the stopping power particles.

The dependence of track diameter on  $dE/dx$  makes possible identification of a particle[35].

Recently the CR39, solid-state nuclear track detectors, appeared to be especially useful for the experimental analysis of more energetic protons (up to 3 MeV). In particular, using in the same laser shots many detector samples covered, for example, with an Al foils of different thicknesses it is possible to estimate energy spectra of protons emitted under various irradiation conditions.

### 2.3.3 ELImon

ELImon is an innovative device for the online monitoring of the pulsed beam fluence. The pulsed beam is diffused by a thin gold target and the elastically scattered protons are detected at a tunable angle. A battery powered detection system consisting of a plastic scintillator coupled to a photomultiplier will detect the diffused protons. In this way it is possible to perform beam burst intensity downscaling by elastic scattering; the integrated total light reproduced by the protons impinging on the scintillator gives a direct and linear measurement of the proton burst intensity[22].

The detection system is shown in the Figure 2.9:

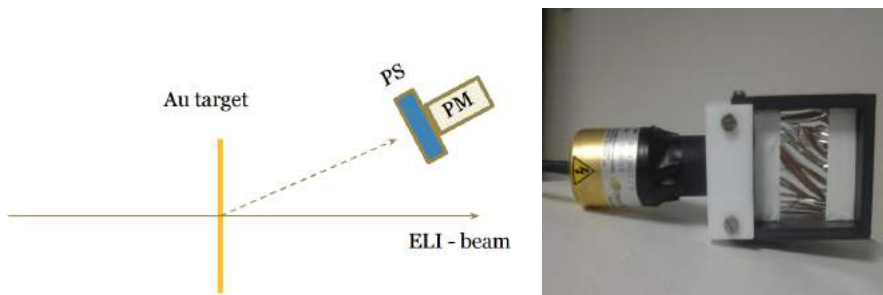


Figure 2.9: The plastic scintillator PM assembly

## Chapter 3

# Laser-plasma interaction

The generation of fast particles from the lasers-matter interaction was first observed in 60th, when the first experiments with a laser irradiating a solid target were performed[36]. Those experiments showed that plasma created on target surface is a source of ions of energies up to several KeV. Parallel to the development of lasers with increasing power, higher ion energies have been achieved; in particular, fast ions in the MeV energy range have been recently recorded.

A real breakthrough in the investigation of laser acceleration of charged particles was the use of high power lasers generating ultrashort pulses ( $\tau_L \leq 1ps$ ). These laser can produce radiation of much higher intensity (currently up to  $\sim 10^{21}W/cm^2$ ) are smaller and can work at pulse repetition rate orders of magnitude higher than ns or sub ns lasers with similar peak powers. Moreover, ultrashort-pulse lasers are capable of producing a short-lived hot plasma, which can emit intense beams of high-energy particle in extremely short bursts of sub-ns or ps duration.

In the present chapter the plasma features and production mechanisms will be described to highlight the physical process which happens when an high intense laser pulse interacts with matter allowing a state change which provokes the plasma formation. It will be described in detail, as a strong electric field generated by the electronic cloud and created inside the plasma, accelerates these particles (like protons and ions), in the normal direction to the target surface.

### 3.1 High intensity laser

The new laser technology *chirped pulse amplification* (CPA) of ultra intense pulse production is at the basis of the laser-plasma interaction and laser induced particle acceleration. A laser (acronym of Light Amplification by Stimulated Emission of Radiation) is a device that generates or amplifies electromagnetic radiation, fluctuating from the long infrared region up through the visible region and extending to the ultraviolet and recently even to the x-ray region. Lasers are based on the stimulated emission, discovered by Einstein in 1917 and postulating that an atom in an excited level could decay to lower energetic level either spontaneously either by stimulated emission. Thanks to this technique it is possible to obtain a peculiar kind of electromagnetic radiation which is spatially and temporally coherent and that can be well collimated. The laser light is widely used in many applications and in a wide range of pulse intensities, duration and wavelength, from pointing devices to data writing/reading of optic discs and so on.

The high intensity laser interaction with matter is a new research field that involves an increasing number of scientists and has a wide range of applications from particle acceleration to inertial confinement fusion and radiation generation. The laser maximum intensity evolved with few successive leaps, the most recent one being the introduction of the chirped pulse amplification (CPA). Since the invention of CPA the ability to increase the energy of ultra-short pulses dramatically improved and now it is possible to produce pulses with a duration of few femtoseconds ( $10^{15}s$ ) and a maximum intensity above  $10^{21}W/cm^2$ .

The production of an ultra short laser pulse with high intensity requires different steps and, depending on the technology used, and one or more amplification stages. First of all a very low energy short pulse ( $\sim 50fs$ ) is created with a simple oscillator laser. After this first stretch in time (chirped in frequency) by a factor  $\sim 10^4$ , then is amplified and finally recompressed. On other hand, the oscillator laser produces a train of few nJ pulses, one of these pulses is extracted, manipulated and stretched.

In the Fig 3.1 a representation of a basic CPA manipulation is presented.

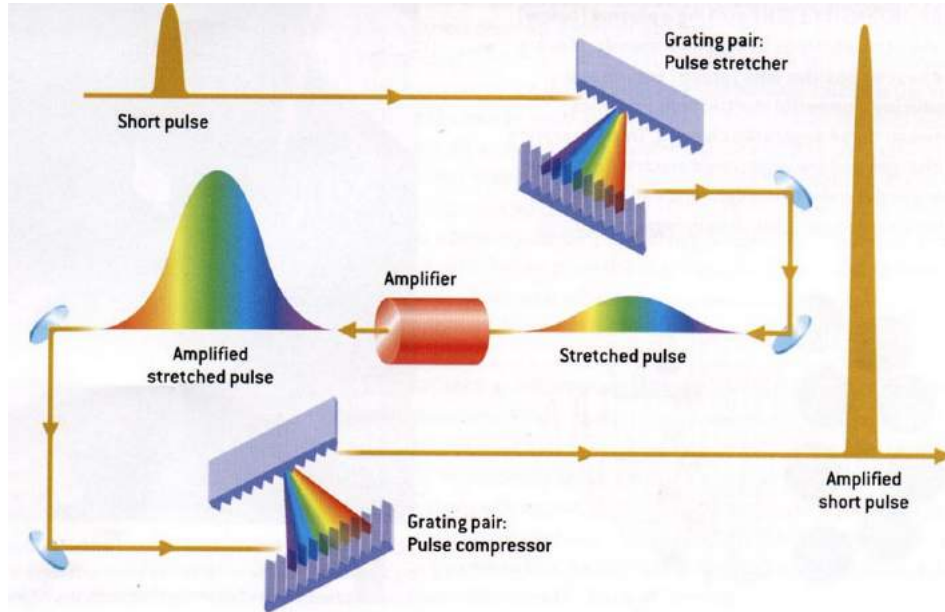


Figure 3.1: The chirped pulse amplification scheme with a pulse made by a low power laser stretched, amplified and recompressed

The stretching and compression steps are realised using a pair of gratings that can be arranged to separate the output pulse spectrum from the oscillator in such a way that different wavelengths follow different paths through the optical system. The different frequencies contained in the short pulse travel on different paths exiting the grating with different timings resulting in stretched pulse up to 4 order of magnitude longer than the initial seed. The pulse is then amplified traveling through one or more stages through an active medium with a wide gain bandwidth pumped by flashes or other lasers. In vacuum chamber the pulse is then compressed with a set of gratings complementary to the stretching set. The compressed pulse is then focused on the target up to few micron of radius reaching intensities that can exceed  $10^{21} W/cm^2$ .

An important characteristic of all the CPA pulses playing a relevant role in the experiments is the so called “pre-pulse”. The laser pulse obtained from the manipulation is ultra-short and intense, but the main peak reaches the target after a low intensity “pedestal” that has a time duration in the range of the ns and intensity in the range of  $10^{21} W/cm^2$ . The characteristic

prepulse can be changed with several techniques. A crucial parameter of the laser system is the so called *contrast* which is the ratio between the peak intensity and the intensity of the prepulse. The value of the contrast is a key parameter in some application and ranges from  $10^6$  up to  $10^{10}$ . It is easy to understand that a low contrast will lead to a very intense prepulse which can effectively interact with the target and possibly destroy it. For these reason the pre-pulse characteristic must be investigated and controlled in order to get reliable results.

Nowadays the high power laser systems available are mainly developed using two active media:

1. Titanium:Sapphire (Ti:Sa or  $Ti : Al_2O_3$ ) which are titanium doped sapphire crystals  $\lambda_0 = 800nm$ . These laser systems are usually smaller and can potentially work at higher repetition rate  $> 10$  Hz, with short period  $\tau \leq 100fs$  and less energetic 10 J pulses compared with Nd:YAG;
2. Neodymium YAG (Nd:YAG) which are neodymium doped YAG crystals ( $Y_3Al_5O_{12}$ , also called YAG from “yttrium aluminium garnet”)  $\lambda_0 \sim 1\mu m$ . These laser have been initially built to study the inertial confinement fusion and are, most of the time, big systems able to produce very energetic 100J, longer pulses  $\tau \sim 1ps$ .

Some of the currently in use laser systems are reported in table:

Name	Laboratory	Country	Type	Energy $E_L$ [J]	Length $\tau$ [fs]	Power $P$ [TW]
Petawatt	LLNL	USA	Nd:YG	700	500	1300
VULCAN	RAL	UK	Nd:YG	420	400	1030
PW laser	ILE	JPN	Nd:YG	400	400	1000
PHLIX	GSI	GER	Nd:YG	500	500	1000
LULI 100TW	LULI	FRA	Ti:Sa	30	300	100
GEMINI	RAL	UK	Ti:Sa	15	30	500
FLAME	LNF	ITA	Ti:Sa	6	30	300

Figure 3.2: Summary on some facility laser in the world

## 3.2 Plasma characteristics

Plasma state can be described as a physical system where free electrons and ions are present in proportions that give a collective character to the dynamics

of the system through the electromagnetic interactions. Important examples of plasma are interstellar gas, star, stellar atmospheres or fluorescent tubes. A more quantitative definition to be developed below. However, in general, a plasma must satisfy the following criteria:

1. Quasi-neutrality. A plasma maintains almost perfect charge balance:

$$-q_e n_e = q_i n_i \pm \Delta \quad (3.1)$$

where  $q_e$  and  $q_i$  are respectively the electrons charge and ions charge while  $\Delta$  is the tiny.

2. Interaction between individual charged particles are negligible compared to the collective effects (*Debye screening*).
3. The electron-neutral collision cross-section is much smaller than the electron-ion cross section:  $\sigma_{en} \ll \sigma_{ei}$ .

### 3.2.1 Plasma frequency and *Debye length*

The plasma frequency is the most fundamental time-scale in plasma and it is defined as:

$$\omega_p^2 = \frac{ne^2}{\epsilon_0 m} \quad (3.2)$$

where  $n$  is the density and  $\epsilon_0$  is the dielectric vacuum constant. Clearly, there is a different plasma frequency for each species. However, the relatively fast electron frequency is the most important, as we consider the plasma frequency as the electron plasma frequency.

The term  $\omega_p$  corresponds to the typical electrostatic oscillation frequency of a given species in response to a small charge separation. On other hand, an ion and electron plasma, can be sketched like a coupling of positive and negative charges which tend to neutralize each others because of the Coulombian force. In this context, the interaction between negative and positive charges can be conceived as an oscillation around equilibrium point, as result of a spatial separation.

For instance, if we consider a one - dimensional situation in which a slab consisting entirely of one charge species is displaced from its quasi-neutral

position by an infinitesimal distance  $\delta x$  Newton's law applied to an individual particle inside the slab yields

$$m \frac{d^2 \delta x}{dt^2} = eE_x = -m\omega_p^2 \delta x \quad (3.3)$$

Note that plasma oscillations will only be observed if the plasma system is studied over time periods  $\tau$  longer than the plasma period  $\tau_p \equiv 1/\omega_p$ , and if external actions change the system at a rate no faster than  $\omega_p$ . In the opposite case the system cannot usefully be considered to be a plasma.

Likewise, if the plasma is observed in spatial scale  $L$  smaller than the space  $v_p \tau_p$  travelled by particle during the period  $\tau_p$ , it cannot find any change in the plasma behaviour. This limit length connected to the plasma period coincides with plasma *Debye length* defined as:

$$\lambda_D = \sqrt{\frac{K_B T}{m\omega_p^2}} \quad (3.4)$$

Note that this term is generally comparable for different species. Clearly a system can be considered a plasma if it satisfies the conditions:

1.  $\frac{\lambda}{L} \ll 1$
2.  $\frac{\tau_p}{L} \ll 1$

Finally, now it is possible to give a more precise plasma parameter definition. This dimensionless parameter is obviously equal to the typical number of particles contained in a Debye sphere and is expressed by:

$$\Lambda = 4\pi n \lambda_D^3 \quad (3.5)$$

The case  $\Lambda \ll 1$ , in which the Debye sphere is sparsely populated, corresponds to a strongly coupled plasma that is the condition where in charged particles are dominated by one another's electrostatic influence more or less continuously, and their kinetic energies are small compared to the interaction potential energies. Likewise, the case  $\Lambda \gg 1$ , in which the Debye sphere is densely populated, corresponds to a weakly coupled plasma where electrostatic interactions between individual particles are occasional and relatively rare events.

### 3.3 Laser Interaction with matter

An high intensity laser pulse interacting with a solid target induces an intense ionization of the material and produces an ultra dense plasma from which the particles are accelerated. This effect causes, indeed, the electrons and ions acceleration from the target with energy and angular distribution depending on its material and thickness.

The understanding of laser to matter energy transfer mechanisms are essential to explain the consequent ion acceleration. The most important steps of the interaction are:

1. The creation of the plasma from laser-target interaction consequently to the target ionization and sputtering effects;
2. The interaction between plasma and the last part of the laser pulse by resonance absorption, which occurs when the beam energy is exactly equal to the excitation energy of the absorbing system and inverse bremsstrahlung effect;
3. The expansion of the plasma and particles emission through ponderomotive force;

#### 3.3.1 Laser-induced ionization

At the beginning of each high power laser-matter interaction with solid /gas /liquid targets stands the ionization process, that turns the target into plasma. The dominant mechanism responsible for the ionization strongly depends on the actual laser intensity and hence the electric field that acts on the target electrons[39]. Typically, the ionization process itself is of minor interest in laser-ion acceleration experiments; however, it is still important to know, at which laser intensities a target will start to ionize, especially with respect to the contrast of a real laser pulse, that can have a significant impact on the ion acceleration.

Laser-induced ionization typically occurs at intensities orders of magnitude below  $\sim 10^{10}W/cm^2$ , which is caused by multi-photon ionization. Here, the bound electron absorbs  $m$  photons, so that it is ejected from the potential of the atom its bound to. Its final energy is given by:

$$E_e = (n + s)h\omega - E_{bound} \quad (3.6)$$

where  $n + s = m$  is the sum of the photons  $n$ , necessary for the ejection of the electron, and the number  $s$  of additionally absorbed photons;  $E_{bound}$  denotes the binding energy of that specific electron.

### 3.3.2 Sputtering effect

During the laser-target interaction may occur four mechanisms sputtering:

1. Thermal, consist to fast evaporation from a heated target;
2. Electronic, which includes the processes of ionization and excitation. Usually there is a changed state (from solid to gas ultra dense) with the consequent expulsion of particles;
3. Exfoliant, which occurs when the system has a high thermal linear expansion;
4. Hydrodynamic, when the high energy of the laser melts the target surface. Impurities from the surface are accelerated by the substrates also fused. In other words, are formed “drops” of material that are ejected from the target.

### 3.3.3 Laser-absorption and energy transfer

The laser absorption is probably the most important process during the laser-plasma interaction, as it transfers energy from the laser to the plasma.

With the laser intensities today available, the laser electric fields are still to low to directly act on the plasma ions; hence, laser energy transfer is mediated by the plasma electrons, i.e, electrons gain energy ( $T_h$ ) in the laser field, which is “distributed” to the plasma ions and atoms through subsequent thermalization (collisions) of the electrons ( $T_e$ ) or other processes like instabilities. The laser absorption by electrons in a plasma can be separated into collisional and collisionless processes. The collisional absorption, which is also called “inverse Bremsstrahlung”, is the collision of an electron with an ion under the presence of an electric field. The collisionless absorption cannot be treated analytically in general, but has been studied with computer

simulations since many years. As a result, a large number of mechanisms has been identified in this regime, where the most prominent is the resonance absorption.

The resonance absorption is a process requiring oblique laser incidence of a p-polarized light wave and a long density scale length. The laser that is incident on the plasma at an angle  $\vartheta$  is reflected near the critical surface of the plasma. Due to the p-polarization of the light wave, the electric field of the laser can reach into the plasma and excite electron oscillations at the critical surface. These oscillations can grow resonantly over several laser oscillations and drive an electron plasma wave into the plasma. Energy can be transferred to the plasma through dampening of this wave by wave breaking or collisions.

### 3.3.4 Ponderomotive force

An important parameter in the laser - target interaction is the ponderomotive force. It is a nonlinear force that affects various physical processes, for example:

- Momentum transfer to the target;
- Changes in the density plasma profile;
- Generation of magnetic fields;

In order to understand the laser-target mechanism that involve in the plasma state it is useful to analyze the motion of a single electron in such a field[38]. The equation of motion can be derived from the Lorentz force:

$$\frac{d\vec{p}}{dt} q \left( \vec{E} + \frac{\vec{p}}{m_e \gamma} \times \vec{B} \right) \quad (3.7)$$

where  $p = \gamma m_e \vec{v}_e$  and  $\gamma = 1/\sqrt{1 - v_e^2/c^2}$  are the relativistic momentum and the Lorentz factor of the electron. In the limit non-relativistic  $v/c \ll 1$  the equation of motion become:

$$\frac{\partial v_y}{\partial t} = -\frac{e}{m} E_y(r) \quad (3.8)$$

It is assumed that the electromagnetic propagates in the positive x-direction as before but with a radial intensity dependence considered in the y-direction only. Taylor expansion of the electric field expression then gives:

$$E_y(\vec{r}) \simeq E_0(y)\cos\phi + y\frac{\partial E_0(y)}{\partial y}\cos\phi + \dots \quad (3.9)$$

where  $\phi = \omega(t - kx)$ . To lowest order:

$$v_y = -v_0\sin\phi \quad (3.10)$$

$$y = \frac{v_0}{\omega}\cos\phi \quad (3.11)$$

where  $v_0 = \frac{eE}{m\omega}$  is the speed electron oscillation. Substituting back into previously equation gives:

$$\frac{\partial v_y}{\partial t} = -\frac{e^2}{m^2\omega^2}E_0\frac{\partial E_0(y)}{\partial y}\cos^2\phi \quad (3.12)$$

Multiplying by m and taking the cycle-average yields it is obtained the ponderomotive force expression on the electron as:

$$f_p = m\frac{\partial \bar{v}_y}{\partial t} = -\frac{e^2}{4m\omega^2}\frac{\partial E_0^2}{\partial y} \quad (3.13)$$

Physically the force will tend to push electrons away from regions of locally higher intensity[38]. A single electron will therefore inevitably drift away from the center of focused laser beam, picking up a velocity  $v_0$  in the process. It is important to remember that the time dependence of the envelop must be slow compared to the laser period because otherwise the separation time- scales used in the derivation lose sense[37]. Moreover, because of the dependence of ponderomotive force from the square of particle charge and mass, the force results the same for positive and negative particles but it is higher for electrons then for protons. When ultra-short laser pulse begins to propagate in a underdense plasma, the ponderomotive force, pushing electrons while ions remains nearly unperturbed because of their bigger mass, creates a longitudinal charge separation that results in a longitudinal electric field which pulls back the electrons again. This perturbation induces a plasma wave that travels in the field at the group velocity of the pulse itself.

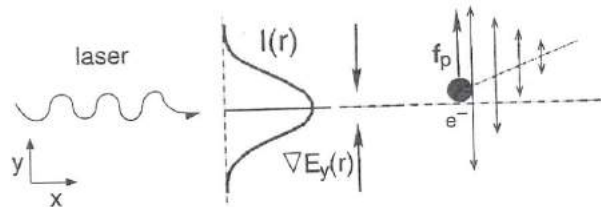


Figure 3.3: Radial ponderomotive force due to a focused beam

### 3.4 Laser induced ion acceleration

When a laser pulse reaches a solid, an overdense plasma slab is obtained and several energy absorption mechanisms can be involved. The laser energy accelerates and heats plasma electrons. At the same time, in particular if a normal incidence is considered, the laser ponderomotive force pushes inner electrons from the surface creating a charge separation which produces an electrostatic field.

Different ion acceleration regimes can be obtained for different laser pulses and target characteristics. These will be briefly described below.

In most of the experiments, the dominant regime is the so-called Target Normal Sheath Acceleration (TNSA). The accelerated protons come from the rear surface and the accelerating field is generated from the expansion of the electrons around the target[37]. Other regimes have been theoretically proposed and later tested experimentally, in which the radiation pressure of the laser is dominant on the heating process and the forward accelerated bunch is composed mainly by the ions of the target and comes from the irradiated surface: Radiation Pressure Acceleration (RPA).

Different interpretations of the acceleration mechanisms have been proposed and many theoretical and numerical studies have been done leading in some occasions to contrasting results. The interpretation of the sometime contradictory experimental results remains no easy task. Most of the laser systems used for experiments are unique machines, each with its peculiar characteristics. The pulse length and contrast may change from experiment to experiment, the target used and the vacuum level are not always constant parameters, but the acceleration mechanism proved to be very robust. The

physics of such extreme conditions is not simple and comprehends many non-linear phenomena even if reduced models are considered i.e. preformed plasma, no ionization, no collisions etc.

### 3.4.1 Target Normal Sheath Acceleration TNSA

During the interaction of the intense electromagnetic wave with the solid, the front surface of the target becomes ionized well ahead the pulse peak. The successive laser-plasma interaction accelerates the electrons through different mechanisms depending on the configuration. The electrons reach high temperature ( $T \simeq MeV$ ) and their free path becomes bigger than the plasma skin depth and the target thickness. This hot electron population propagates through the target, reaches the rear side and expands into vacuum. Most of these electrons remain confined near the target and recirculate through it, inducing a strong electrostatic field over a Debye length  $\lambda_D$  (micrometer range). The electrostatic fields on the rear side reach values up to TV/m which can ionize the atoms present on the unperturbed surface and accelerate the ions newly produced. This acceleration mechanism is known as Target Normal Sheath Acceleration (TNSA).

In the Figure 3.4 there is showed an schematic representation of the TNSA regime:

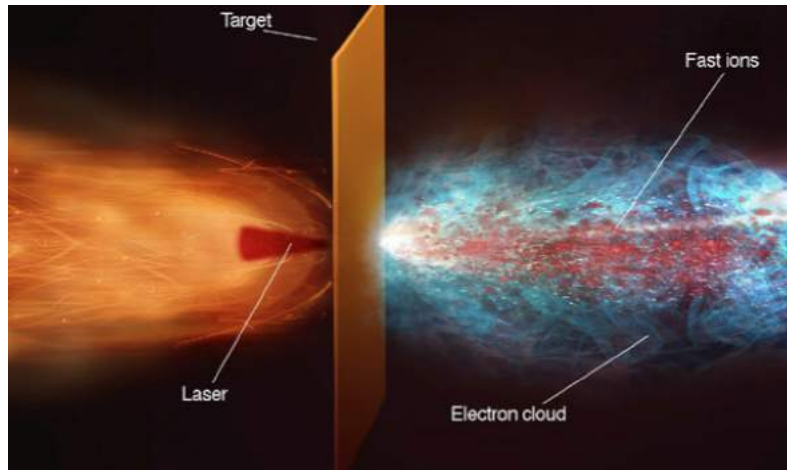


Figure 3.4: Scheme of acceleration mechanisms of the interaction between laser beam with thick solid target

The observation of multi MeV protons from the rear side of a laser irradiated solid foil is achieved independently from the target composition.

Generally, the energy spectra of the protons have a typical trend with a progressive cut-off as showed in the Figure 3.5:

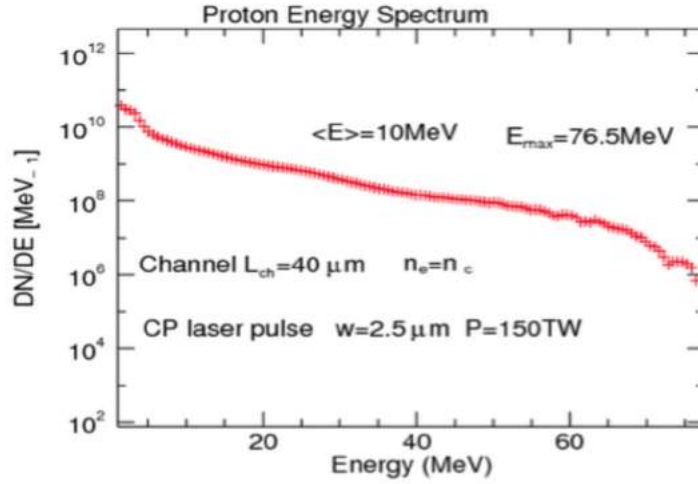


Figure 3.5: Typical energy spectrum of laser-driven proton beams

The electrons escaping from nuclei will acquire a kinetic energy greater than their rest mass, thus they become highly relativistic. In this context a useful parameter is the so-called laser strength parameter, defined as:

$$a_0 = \frac{eA}{m_e c^2} \quad (3.14)$$

it represents the peak value of the laser potential vector normalized with respect to the electron rest mass. It can be related to the laser peak intensity  $I$ , and the wavelength  $\lambda$ , of the laser by:

$$a_0 = \frac{e}{m_e c^2} \sqrt{I \lambda \frac{2}{\pi c}} \quad (3.15)$$

Thus  $a_0$  can be seen as the maximum momentum of an electron quivering in the laser field normalized respect to its rest mass. Indeed, since the laser pulse cannot penetrate into solid density regions, the absorbed energy is

transported mostly by energetic electrons called “hot” created during the interaction from several mechanisms[41].

The electrons involved in the TNSA regime can be divided in two populations: the electrons accelerated by the laser form a hot ( $T_H \simeq MeV$ ) low density ( $n_h \simeq 10^{20} - 10^{21} cm^{-3}$ ) population, whereas the rest of the electrons constitute a cold electron specie with a high density  $n_c \simeq n_e$ ,  $n_e = n_h + n_c$  and low temperature (c and h refer to cold and hot respectively). The ion population of the target can be also divided into two species, one being the heavy ions of the target with a relatively low charge over mass ratio  $Z_H/M$  and density  $n_h$ , the other specie is constituted by the protons with charge  $Z_L$  and density  $n_L$  (H and L stand for “heavy” and “light” ions). The model considers a 1D geometry in which the target is a plane sharp-edged plasma slab. The equations follow from the one dimensional Poisson equation:

$$\frac{\partial^2 \phi}{\partial x^2} = 4\pi e(n_e - Z_L n_L - Z_H n_H) \quad (3.16)$$

and look for the solution of the electric potential  $\phi$  in the semi-space of the target near side. Some assumption are needed to estimate the acceleration of the ions and proceed with the derivation. First of all, for short pulses,  $\tau < ps$ , the laser-target interaction occurs on a time scale shorter than the one typical of the ion motion. The cold electron population is assumed to have a constant density  $n_{0C}$  whereas the hot electrons are supposed in thermal equilibrium with the electrostatic potential then described by a Boltzmann distribution for the electrostatic potential at the target vacuum interface, where the maximum value is achieved, is obtained after some non trivial math[44]. The value of  $\phi$  at  $x = 0$  results to be function of only the electron temperature  $T$  and of the maximum energy of a bound electron  $\epsilon_e max$ .

$$\phi(0) = \phi_0(T, \epsilon_e max) \quad (3.17)$$

where the term  $\epsilon_e max$  depends on the physics of the laser-solid interatio and is the most crucial point of the model. Its value can be established from experimental data or properly conducted numerical simulation. In an estimate of  $\epsilon_e max$  is given as a function of the total laser energy  $E_L$ ,  $\epsilon_e max(E_L)$ . The electron temperature is then assumed to be:

$$T = mc^2(\sqrt{1 + a_0^2/2} - 1) \quad (3.18)$$

which relates the electron temperature directly to the laser irradiance through the adimensional parameter  $a_0$ . The maximum proton energy, or the cut-off energy of the proton spectrum analogously, is then simply given by

$$E_{cut-off} = Z_L \phi(0) = Z_L f(E_L, I_L) \quad (3.19)$$

This model predicts the cutoff energy of the proton spectrum making some strong assumption. The heavy ions are considered immobile on the time scale considered, the number of the light ions, the accelerated population, must be much smaller than the hot electrons. The hot electrons distribution does not evolve and its temperature does not decrease in time contrarily to what can be expected. Despite these strong hypothesis the model successfully predicts the scaling laws of the proton acceleration in the TNSA regime.

Charged particle beams produced with this new acceleration technique, have also a very high peak current ( $\sim 10^{12} - 10^{13}$  particles per shot) and rather small transverse and longitudinal emittance because of very small spatial dimension of laser spot and of its very short temporal amplitude, respectively. Despite this, the emitted particles show a very large angular divergence (up to 30 deg) when they leave the target surface. Moreover, the angular distribution also depends on the energy spectrum, as it is possible to see in the Fig 3.6.

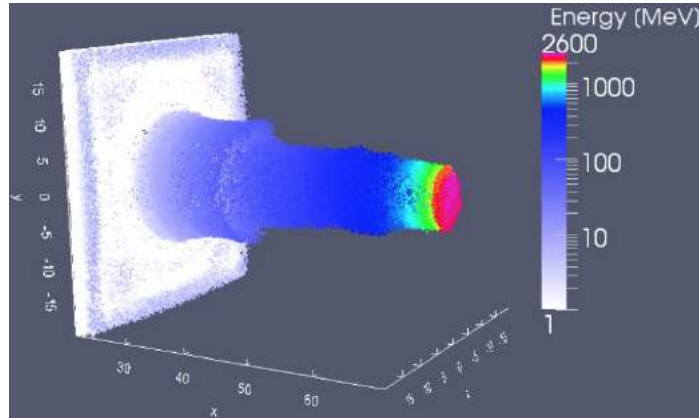


Figure 3.6: PIC simulation

### 3.4.2 Radiation Pressure Acceleration

Radiation Pressure Acceleration (RPA), is the ion acceleration regime which starts to dominate over TNSA at higher intensities. When there is a thick target the ponderomotive force is effective on a thin layer at the front surface of the target. The force applied by the laser depletes in a small layer, generating an electrostatic field which accelerates the ions. On the other hand, if there is a thin layer, the target is accelerated as a whole. These two different possible configuration are usually referred to as “hole boring” (HB) and “light sail” (LS)[45].

In the hole boring regime, the ion acceleration is due to the electrostatic field  $E_x$  (being  $x$  the direction of propagation of the laser), arisen from the electron displacement generated by the ponderomotive force. In this context the right model to explain the process consist to considered that there is a quasi-equilibrium between the ponderomotive force and the electrostatic force. The main idea is that the laser pushes the electrons with a force  $F_x \simeq 2I/c$  and penetrates in the plasma.

At earlier times the ions remain immobile at the initial density  $n_0$  whereas the electron density is depleted by the laser on a first layer of thickness  $x_d$ . The resulting electric field has a maximum  $E_0 = 4\pi en_0 x_d$  which accelerates the ions present in the depleted region[40]. The ions move forward and pile up until their density becomes singular and the fast particles overcome the slow ones leaving the accelerating region.

If the target is thin the laser is able to repeat the acceleration stage over the same ions and considerably higher energies are reachable. After the first acceleration the ions do not pile up in only singular high-density point. The laser interacts basically with the electrons only, but because the target is thin the ion motion is strictly bound to the electrons and although not formally correct, the target can be considered as a rigid object. Accepting this assumption the change in momentum of the entire foil must to be balance of the laser momentum resulting in as a non-relativistic estimate for the light-sail regime. Clearly, acceleration becomes more effective when is reduced areal mass density. The ion energy in the light-sail regime thus scales quadratically with laser intensity. This far more rapid scaling suggests that for higher intensities, RPA should become the dominant effect on ion dynamics in laser interactions with thin solid foils.

## Chapter 4

# Dosimetry for a laser - driven beam

As already explained in the previous chapter, the laser - target interaction produce a very high number kind of particles such as protons, electrons and ions with very high peak current, for example typically up to  $10^{13}$  protons within bunch duration of a few picosecond are emitted. Furthermore while in a typical beam emitted by a traditional accelerator is produced a current with very short repetition rate and high reproducibility bunch to bunch, in this case each shot is different to the previous. More precisely each shot is not exactly same to the other shot but there is difference to the beam emission depending on several factors such as the laser focus in the target or the vacuum level in the interaction chamber. In addition, in the laser-target interaction the beam has a large divergence and low transverse emittance. Often the electromagnetic noise is overlapping on the particles signal. It was observed, in fact, in several experiments, the high-frequency RF emissions from dense laser plasmas. All these characteristics make the dosimetric measurement extremely challenging. Today the application of the laser driven ion beams in medical physics can be a valid alternative to beams obtained by the conventional accelerator machine (such as cyclotron, synchrotron and LINAC) but so far no protocol for dose measurements has been established. In this context, one of the future ELIMED task, will be the definition of procedures aiming to obtain an absolute dose measurement at the end of the transport beam line with an accuracy as close as possible to the one required for clinical applications. A precise knowledge of the absolute dose, released

by the incoming radiation, is essential in the medical applications.

The dosimetric accuracy of a radiation treatment is a crucial prerequisite in order to estimate the correspondence between planned and delivered dose. In fact, it is demonstrated that an uncertainty higher than 5% in the absorbed dose evaluation can compromise the effectiveness of a radiation treatment as well as the patient health. Dosimetric international protocols, where the use of specific detectors and procedures are recommended, have been already established since 2000 for conventional clinical ion beams. For example, with conventional beams, measurements of absorbed dose are performed, according to the dosimetric protocols, with ionisation chambers[52].

Nevertheless as the worldwide availability, the maximum energy and intensity of laser-driven beams are continuously growing, during the last decade many researchers started several investigations on targets, detectors and procedures, in order to achieve an accurate evaluation of the dose released by laser driven ion beams. This represents a crucial step for the future use of these beams in multidisciplinary experiments like biology irradiation, dosimetric tests and detector characterizations. Currently, two main classes of dosimeters are under investigation for laser-driven beams: solid state detectors (such as nuclear-track detectors, radiochromic films, and fluorescent image-plates) and ionimetric detectors like Faraday Cups (FC) and ionization transmission chambers for high dose-rate beams.

## 4.1 The Faraday Cup

### 4.1.1 The Faraday Cup as beam intensity monitor

Faraday Cups are commonly used for beam intensity monitoring due to their simplicity and reliability. Despite the destructive aspects of the measuring operations, they can provide accurate information on the beam current in a very simple manner: a conductive beam stopper is introduced in the beam path and the total charge carried by the particles is collected. The term Faraday Cup (FC) was assigned for celebrating Michael Faraday who first theorized the existence of ions around 1830.

The most basic design consists only of an electrically conductive material in the shape of a cup, typically with cylindrical symmetry, which is placed in the path of the charged particle beam whose current is to be measured.

Ideally, all the particles in the beam are absorbed by the Faraday Cup, thereby inducing a charge on the cup that can be read out as a current with the appropriate electronics. In this theoretically ideal case, the Faraday Cup acts as a resistor, so the current read out from the Faraday Cup is a direct measurement of the beam current.

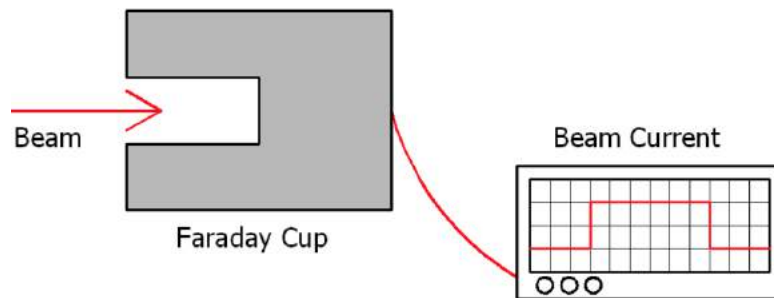


Figure 4.1: Scheme of the Faraday Cup

Although this analogy between a Faraday Cup and a resistor is useful at illustrating the essential principle behind Faraday Cup operation, it excessively simplifies the interface between the charged particle beam and the Faraday Cup, hiding the underlying complexities of the interactions involved with the transfer of charge from the beam line vacuum to the conducting material of the Faraday Cup. The physical processes that involving in the scattering of the incident particle beam with the material of the Faraday Cup are complex and depend on the type of particle and the kind of cup (in term to the material and geometric configuration).

Many important properties should be considered in designing a FC, including the characteristics of secondary electron (SE) emission, charged particle stopping range, and particle back scattering, especially the ability to preserve the high-frequency components of the electrical signals generated by the sub-nanosecond-level pulsed proton beam.

#### 4.1.2 The Faraday Cup as absolute dosimeter system

A Faraday Cup has a linear response for a given number of particles and its signal is independent from the dose rate, therefore these device can represent a good alternative to perform absolute dose measurements[51]. Under certain

circumstances, when the energy spectrum of the beam is known, the Faraday Cup can be used to evaluate the particle fluence distribution and the absorbed dose.

Using the relation between the absorbed dose[50], the fluence and the stopping power it is possible to evaluate the absolute dose measurement by a Faraday Cup:

$$D_W = \Phi \frac{S_W}{\rho_W} \Pi_{ki} \quad (4.1)$$

where  $\Phi$  is the particle fluence,  $S_W/\rho_W$  the mass stopping power of the proton beam in water and  $\Pi_{ki}$  is product of the correction factors due to the beam divergence, scattering, field nonuniformity, beam contamination and secondary particle build-up. This method relies on an accurate value of the proton stopping power in water for which the uncertainty, according to ICRU Report49, is estimated to be 1-2 %[54]. The absorbed dose to water due to a monoenergetic proton beam, can be then calculated according to the expression:

$$D_W = \frac{S(E)_W}{A} \frac{Q}{e} 1,602 * 10^{-10} (Gy) \quad (4.2)$$

where A is the effective beam area in  $cm^2$ ,  $S(E)_W$  is the mean mass stopping power, expressed in  $MeVcm^2g^{-1}$ , at proton energy E, Q is the total charge collected by the Faraday Cup in Coulomb. In the last equation appear evident that for a better evaluation of the dose is necessary a correct evaluation of the beam spot area and the charge measurement by FC must to have the smallest uncertainty as possible.

Assuming that the charge collection efficiency is near 100%, the main uncertainty in the fluence measurement is in the determination of the beam area. The effective area of the beam depends on the dose distribution inside and can be expressed as:

$$A_{eff} = \int_0^{2\pi} \int_0^R r P(r) dr d\theta \quad (4.3)$$

which can be approximated as:

$$A_{eff} \sim 2\pi \sum_{i=0}^{i=R} r_i P(r_i) \quad (4.4)$$

where  $r_i$  is the scan step,  $P(r_i)$  is the normalized dose distribution associated with the beam profile and  $R$  is the radius value at which  $P(r_i) = 0$ . The dose distribution is experimentally evaluated to fluence measurements at different distances from the last collimator from which is emitted the beam.

As already explained previously, the charge collection depends on several factors. When a Faraday Cup is used as ion detectors it is necessary that the secondary electrons must be ejected from the interior metal surfaces of the device when the ions strike those surfaces. One of the uncertainty source in FC measurements is due to the production of secondary electron that may escape from the FC aperture, causing a wrong charge collection.

The loss of secondary electrons signal will lead to an larger positive particle current or to a smaller negative particle current, either of which would result in an incorrect value for the absolute dose. Thus, either the contribution to the current due to the escaping secondary electrons must be determined or the FC must be designed to recapture all of the secondary electrons. In order to recapture the ejected electrons many traditional FC detector designs have cylindrically symmetric components and employ either coaxial electrostatic fields or magnetic fields. Based on a literature survey of existing Faraday Cups (Cambria et al.) an accurated study has been performed at INFN-LNS within the ELIMED activity. In the FC design, several parameters have been considered:

1. Window: A very thin entrance window has been used primarily to avoid any significant proton energy loss. In fact, usually are used kapton or mylar windows, in order to minimize the production of secondary electron (SE) and maintain the vacuum in the cup.
2. Cup: Although copper cup and wall thickness has to be sufficient in order to stop both the primary beam (protons) and the secondary particles produced in the interaction with the window and the cup itself
3. Guard ring or suppressor: An electric field can be applied in order to attract the secondary electrons generated in the cup toward the cup itself and stop the ones produced in the thin entrance window.
4. Vacuum: the charged particle beam has to move in a high vacuum ( $\sim 10^{-5}$  mbar) region before reaching in the cup in order to avoid the possible ionization of the gas generating a residual charge which can give an incorrect charge collection measurements

The FC realization has been possible thanks to several preliminary studies performed in order to optimize shape, dimensions, materials and electric field features. These studies have been carried out using the COMSOL FEM (Finite Element Method) software, the Simion FEA (Finite Element Analyze) software and, also, the Monte Carlo Geant4 simulation toolkit with the main aim to optimize the FC as absolute dosimeter for ion-beams and to maximize its performances also for laser-driven ions[56].

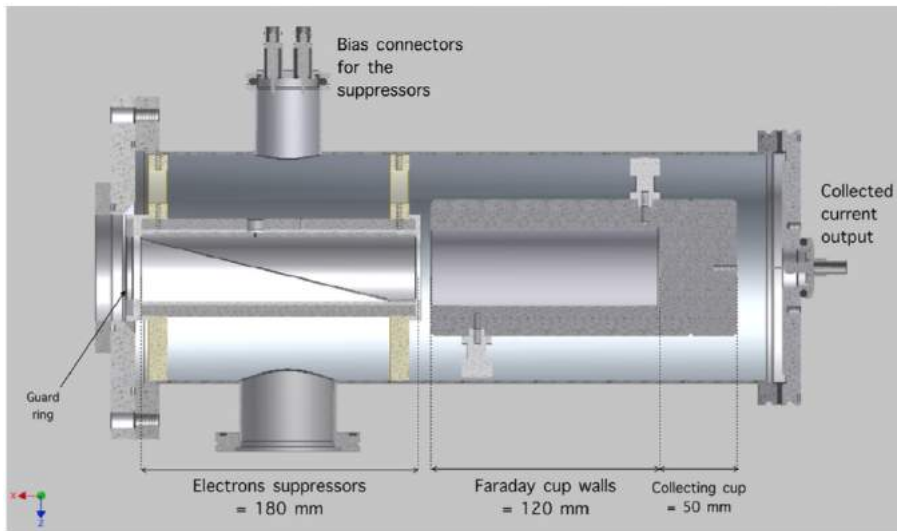


Figure 4.2: Schematic layout of the Faraday Cup (FC) detector. The current collected in the cup is sent to an electrometer for integration.

The last figure shows the final FC configuration with its details. It is about 400 mm long with an internal radius of 20 mm. The main components are a 25  $\mu\text{m}$  kapton window, a 5 mm thin mass ring, a 180 mm steel suppressor and a 100 mm aluminium cup. Since the ionization of the residual gas could affect the FC measurements, a high vacuum, of about  $10^{-5}$  mbar, is required as working condition.

In order to maximize the charge collection accuracy, following the work of Thomas et al., a special-shaped electric field has been designed. It is generated by the combined effect produced by two coaxial electrodes.

Typically a Faraday Cup is composed by a metallic cylinder provided with a guard ring on which a negative voltage is applied. The negative voltage

generates a coaxial and symmetric electric field[56]. The guard ring voltage needed for secondary electron suppression can be estimated considering the maximum energy  $E_{max}$  transferred to secondary electrons during the collision with the cup. Assuming that the proton energy is higher than the orbital electron energy ( $E_p \gg E_e$ ), the maximum energy transferred to electrons depends on the incident proton energy but also on the emission direction:

$$E_{max} = 4 \frac{m_e m_p}{(m_e + m_p)^2} E_{proton} \cos^2 \theta \quad (4.5)$$

where  $E_{proton}$  is the incident proton energy and  $\theta$  is the angle between the direction of the incident beam and the trajectory of secondary electrons,  $m_p$  and  $m_e$  are the proton and electron mass respectively. According to this equation it is possible to estimate the worst points where the possibility of the electron escape is maximum and investigate the electron trajectories ejected from these points. Starting from these points several studies to perform the better geometrical configuration of the suppressor in order to maximize the number of collected secondary electrons and minimizing the collection of the secondary electrons. The better configuration found it is shown in the figure 4.3

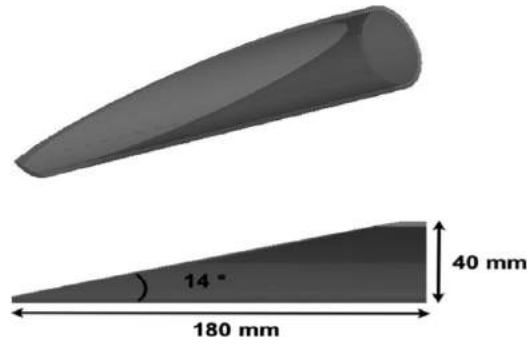


Figure 4.3: 3D view and dimension of the internal electrode of the Faraday Cup

The cylindrical symmetry of the electric field provided by the external electrode is broken due to the presence of the internal one. The resulting effect is a strongly asymmetric electric field, characterized by a significant transversal component able to maximize the deflection of the secondary electrons generated by both the entrance window and the cup.

The three components of the electric field as shown in the Fig. 4.4 are generated, by means of the COMSOL software, applying a bias of -600 V to the internal electrode and of +600 V to the external one.

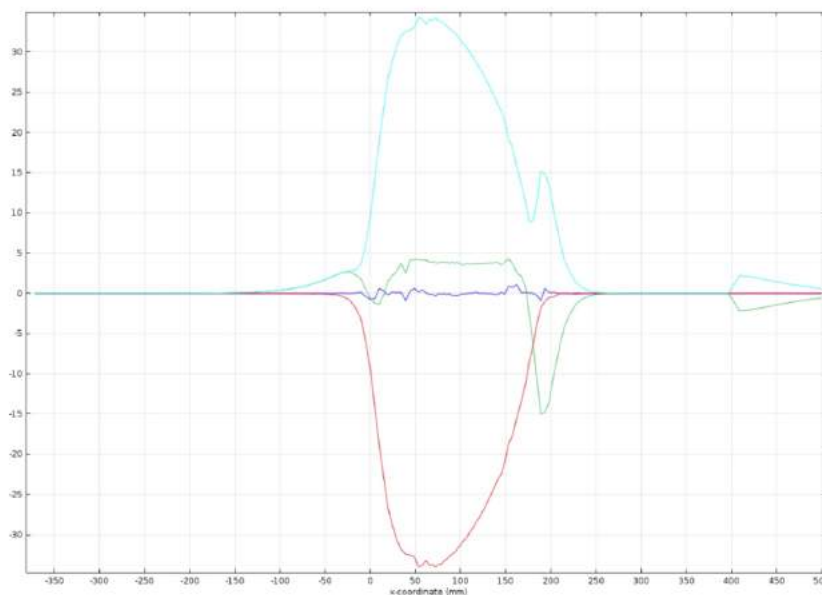


Figure 4.4: Electric field components  $E_x$  (green),  $E_y$  (red),  $E_z$  (blue) and the module  $E$  (sky blue). The electric field is expressed in V/mm and the X axis in mm.

Thanks to break cylindrical symmetry in the electric field, there is a big transverse component of the electric field. In this configuration the secondary electron produced in the entrance of the windows are deflected and the secondary electrons produced in the cup and in the walls are accelerate and collected.

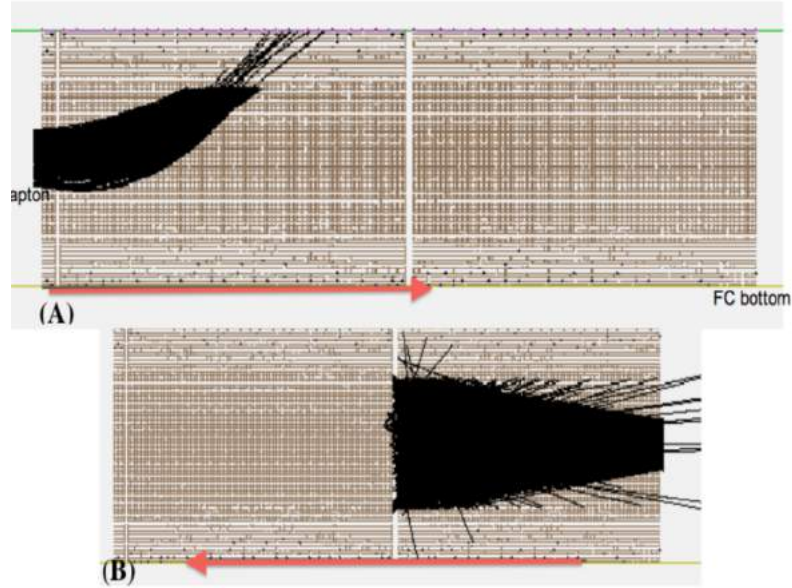


Figure 4.5: Simulation of the secondary electrons with an angular divergence of  $10^\circ$  and with an energy of 520 eV, emitted from the kapton entrance window (A) and from the cup bottom (B)

## 4.2 Preliminary test

The Faraday Cup behaviour response has been preliminary tested using 62 MeV conventional proton beams in different experimental campaigns. The tests have been carried out at the CATANA (Centro di AdroTerapia e Applicazioni Nucleari Avanzate) hadrontherapy facility of the Southern National Laboratory (LNS) in Catania. The response of the detector versus the applied voltage to the suppressor electrode, the dose, the dose rate have been investigated. Moreover a comparison between the absolute dose measures carried out with the Markus ionisation chamber as respect the one measured with the Faraday Cup, have been performed in order to estimate the real capability of the device to perform a dose measure with the precision required by the international protocols.

### 4.2.1 Experimental setup at *Centro di AdroTerapia e Applicazioni Nucleari Avanzate (CATANA)*

The CATANA hadrontherapy facility (INFN-LNS) in Catania, is currently the unique Italian protontherapy facility for the radiation treatment of ocular melanoma with proton beams[66]. This facility make use of 62 MeV proton beams accelerated by a superconducting cyclotron and transported inside a specific treatment room. Figure 4.6 shown two different views of the CATANA protontherapy room with the transport and diagnostic devices used for the therapy.

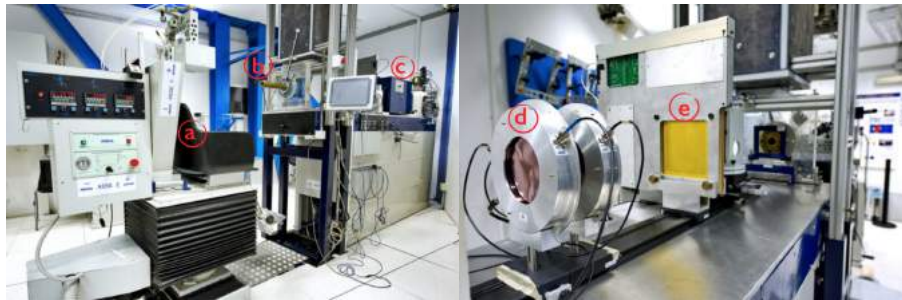


Figure 4.6: View of the CATANA beam line: a) Treatment chair for patient immobilization; b) Final collimator; c)Box for the location of modulator wheel and range shifter; d)Monitor chambers

The proton beam exits in air through a 50  $\mu\text{m}$  Kapton window placed at about 3 m from the isocenter. The isocenter represents the point in the space, along the proton beam axis where all the dosimetric evaluation are performed and it is the point where the tumor center is positioned during the treatment.

Just before the exit window, under vacuum, the first scattering foil made of 15 $\mu\text{m}$  tantalum is located. The first element of the beam in air is a second tantalum foil 25 $\mu\text{m}$  thick provided with a central brass stopper of 4 mm in diameter. The double foils scattering system is optimized to obtain a good homogeneity in terms of lateral off-axis dose distribution, minimizing the energy loss[65].

After these two elements, downstream the scattering system, a range shifter and a range modulator are placed inside a box.

A dosimetric key element of the treatment line is represented by two transmission monitor ionization chambers. The aim of the chambers is, respectively, to provide the on-line control of the dose. At the end, the last element before isocenter is a collimator located at 8.3 cm upstream of the isocenter.

During the experimental test, the Faraday Cup has been located along the beam-line at about 9 cm downstream the last collimator on a straight plane arranged instead of the treatment chair for patient immobilization, see the Fig. 4.7.



Figure 4.7: Faraday Cup mounted along the CATANA beam-line

The FC operating vacuum was  $10^{-5}$  mbar and the current signal was measured by means of an electrometer Keithley (Model 6517A). In order to process online the signal acquired by the electrometer, a Labview software has been implemented. In the Appendix C is reported the code.

## 4.2.2 Experimental characterization

As discussed in the previous section, a Faraday Cup to be used for absolute dose measurements, needs to be designed and equipped with a specific suppression electric field devoted to the minimisation of the secondary electrons loss.

### Charge-voltage characteristic

The first step in the experimental characterisation of a FC, is the study of its response (measured charge  $Q$ ) as function of the applied electric field ( $V$ ).

This is necessary in order to find the more stable part of Q-V curve, where also small variation of the applied potential will not sensibly affect the overall dose evaluation.

Figure 4.8 shows the experimental trend of the charge measured from the FC when the bias at the outer electrode varies from -2400 Volt to 2400 Volt. Each point corresponds to the charge accumulated by the FC for a total released dose of 13 Gy and it represent the average value of six consecutive measures. The error bar is expressed as the correspondent double sigma of a normal distribution. It is possible to observe a quite symmetric behaviour of the accumulated charge passing from negative to the positive bias values and a flat shape of the curve when the absolute applied voltage value exceed the 1000 V. In particular, the curve region between -800 Volt and -1500 Volt appears quite flat (variations less than 1%) and it was chosen as the operation region for the following experimental measures.

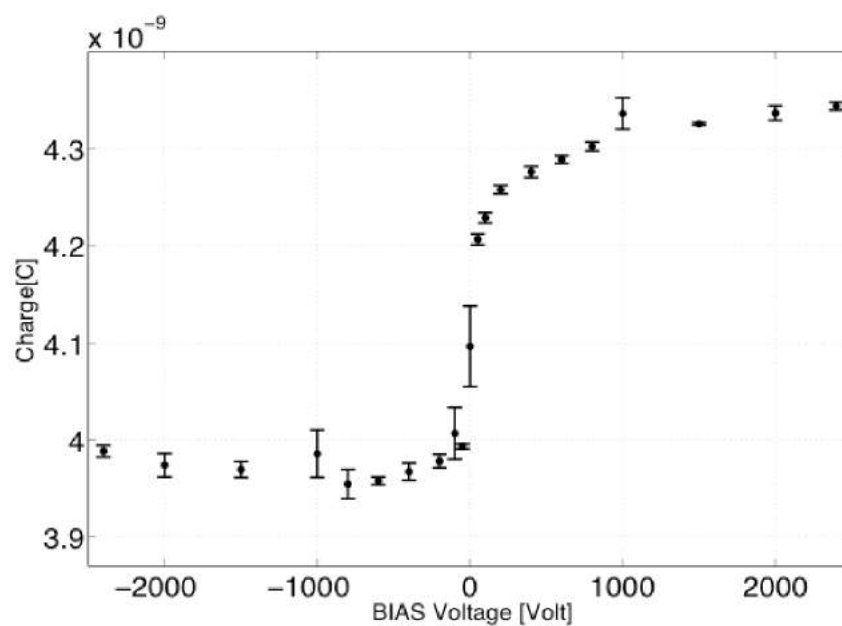


Figure 4.8: Charge measured by the Faraday Cup when the bias applied to the external electrode varies from -2400 to +2400V

## Dose-rate dependence

The evaluation of response from the beam dose rate is essential for any dosimetric system and its importance is still more important, in the case of laser-driven beams. They are in fact characterised by very high intensities that make a lot of conventional dosimetry not usable. Although the Faraday Cup response should not be affected by the dose rate value, its dose-rate dependence must be verified. The CATANA facility allows the transport of proton beam in a very large dose rate range (from tens up to hundreds of Gray). This permit us to carry out a complete characterisation of the FC response.

The secondary beam monitor detector (SEM) placed in-vacuum along the beamline, permit to monitor in real time the proton beam fluence. It was than used as reference detector but its response was firstly calibrated against the Markus chamber absolute dosimetry. Once its linearity in respect to the Markus chamber response was verified, only the SEM detector was used to monitor the beam current during the tests. Figure 4.9 reports the ratio of the FC versus the SEM detector as function of the dose rate when the external electrode was biased at -800 V. Each point is averaging the current of both SEM and FC detectors over a big number of points and keeping constant the proton beam fluence. Error bars are the standard deviations of the same set of points. The curve shows as,for values below 15 Gy/min, the FC response underestimate the collected charge indicating a minimum operational value for the device.

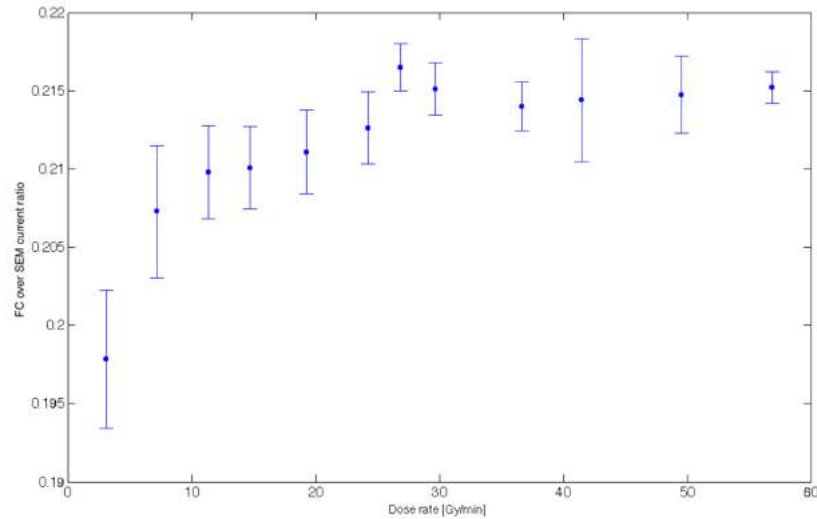


Figure 4.9: FC versus the SEM detector as function of the dose rate

### Dose dependence, dose repeatability and dose accuracy

The measure of the absolute dose using the FC, the evaluation of its repeatability and of its accuracy as respect the Markus chamber absolute dose measure, was the main task of the FC characterisation. Firstly the linearity of the FC charge as respect the released dose has been verified in a dose interval ranging from 9 Gy up to 90 Gy. The measure has been conducted polarising the FC external electrode at -800V and for a dose-rate value of the proton beam of 13 Gy/min. The result of the dose dependence is reported in Figure 4.10 where a response of the FC linear with the absorbed dose is fully demonstrated. For each fixed dose value 13 Gy charge measures have been performed and a maximum standard deviation of 1 % has been found, this representing the repeatability of our charge measure. This error will be part of the overall error in the dose calculation when the complete Equation 4.2 will be applied.

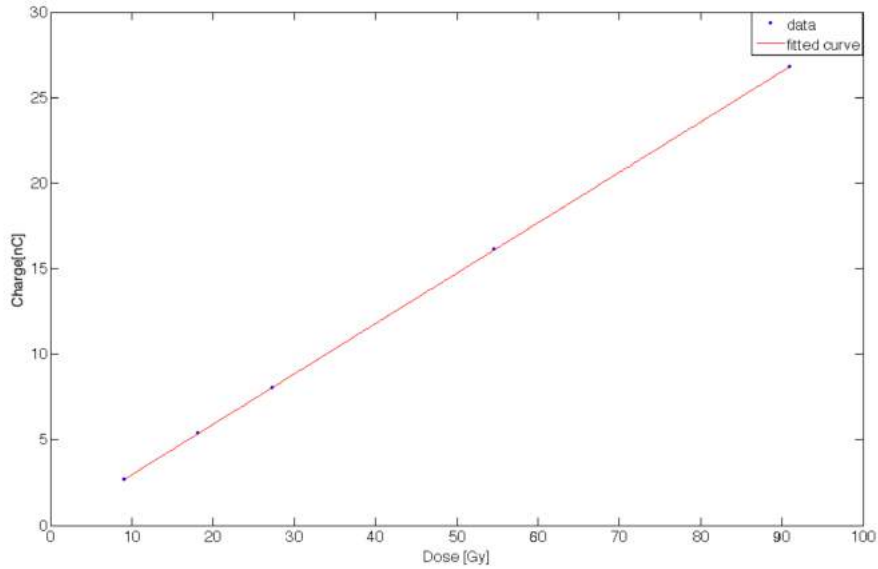


Figure 4.10: Charge measured with the FC as function of the released dose

As already explained in the previous section, in order to obtain a precise dose measure from the FC charge reading, the evaluation of three independent parameters must be carried out Eq.4.2:

1. The integrated charge from the FC, that is directly proportional to the beam total fluence;
2. The area of the proton beam, as the dose is expressed in Gray per centimetre square;
3. The energy of the beam from which the value of the stopping power can be retrieved.

In this process, one of the main critical parameter is the point 2, i.e. the correct knowledge of the beam spot area. In order to minimise the dose calculation uncertainties related to the beam spot-size calculations, a Matlab software has been implemented an software in Matlab code. In Figure 4.11 the flow-chart of the program is reported with its main steps for the computation of the beam profile while in the Appedix A the code is reported. The software assumes that a calibrated image of the beam spot size is available.

In our case the image is acquired using a gafchromic film positioned just in front of the FC entrance windows, i.e exactly at dose effective measurement point.

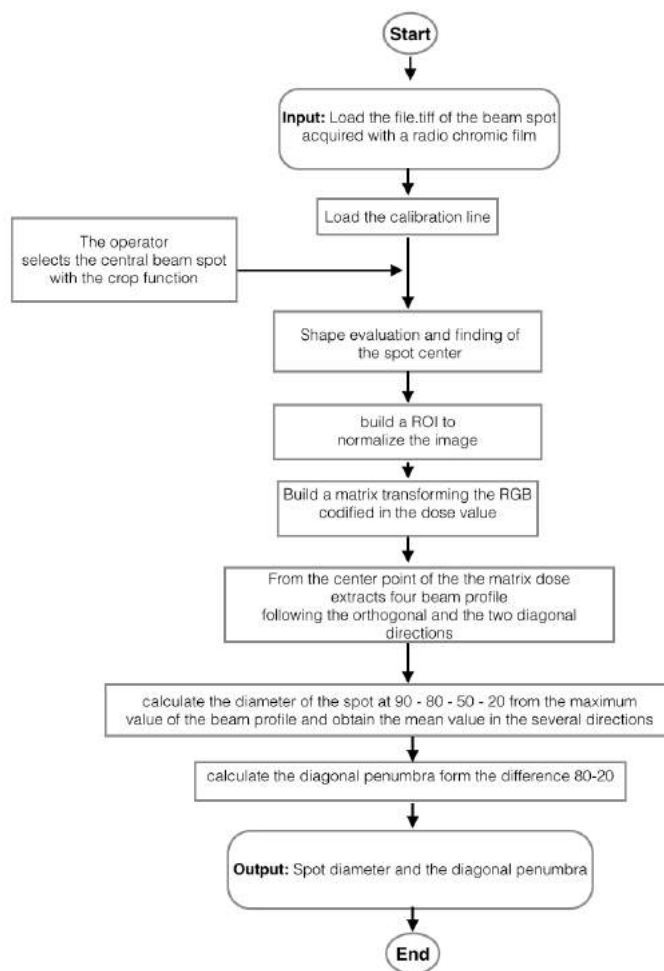


Figure 4.11: Flow chart of the Matlab software used for the estimation of the beam spot area.

In the considered experimental setup a collimator of 20 mm in diameter has been used, and a foil of the Radiochromic film EBT3 has been positioned in front of the Faraday Cup window at about 9 cm downstream the collimator (see the Figure4.7).

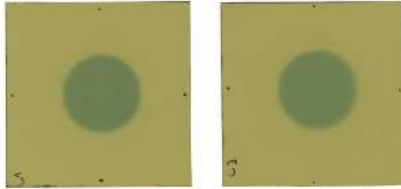


Figure 4.12: Pictures of the beam spot obtained with a Radiochromic film EBT3

The image of irradiated gafchromic film is shown in Figure 4.10, where the circular beam spot size is clearly visible. From the beam profile images and retrieving the dimension of the 50% of many one-dimensional profiles, the value of the surface  $S$  can be derived with accuracy of the order of 2%.

Once the total collected charge and the surface  $S$  are measured, the last parameter necessary for the derivation of the total absorbed dose, is the stopping power value of the beam entering in the FC. The Bethe and Bloch expression can directly calculate the stopping power, if the energy of the proton beam entering in the cup is known and this latter can be directly derived by the experimental measure of the Bragg peak of the monochromatic beam used for the measure.

The experimental Bragg peak for the mono-energetic proton beam, has been measured following the IAEA TRS 398 protocol and using an advanced Markus chamber in water. From the acquired Bragg peak, the proton beam range in water can be derived with an accuracy of the order of 0.2 micron. From this result, the energy and hence the beam stopping power can be calculated with an overall error of the order of 1%.

The stopping power value of  $10.92 \text{ MeV} \cdot \text{cm}^2 / \text{gr}$  has been used corresponding to a proton beam energy of 59 MeV.

Table 4.13 report the final dose calculated using the FC with the application of the Equation 4.2 for two different values of the external electrode bias (-1000 V and -1500 V). In the table the reference dose calculated with the Markus chamber and the percentage discrepancy with the FC dose is reported

Applied Voltage [ V ]	FC Charge [C]	FC Dose [ Gy ]	Reference dose [ Gy ]	Absolute Discrepancy [ % ]
-1500	3,97E-09	12,86 ±2.57	13,68	6.01
-1000	3,99E-09	12,92± 2.58	12,92	5.62

Figure 4.13: Dose calculated with the Markus chamber and the percentage discrepancy with the FC dose

## Chapter 5

# Experimental tests in laser facilities

As previously mentioned, several aspects make the dosimetric measurement in laser environment extremely challenging: the poor-reproducibility shot-to-shot, the large divergence, the low transverse emittance of the beam and the high-frequency RF emissions interfering on the particles signal.

In order to characterize the species and the fluence of the particle emitted in the TNSA regime and the intensity of the electromagnetic pulse produced in the laser-target interaction, two experimental campaigns have been performed in two laser facilities. Experimental tests have been carried out at the Terawatt Apparatus for Relativistic And Nonlinear Interdisciplinary Science (TARANIS) at the Queen's University in Belfast (December 2014, February 2015) and Prague Asterix Laser System (PALS) in Prague (May 2015). The plasma characterization in terms of particle emission has been performed using different detectors: Silicon Carbide (SiC) and CVD Diamond detector have been used as on-line diagnostics using the Time of Flight (ToF) technique; radiochromic film and CR39 have been used as passive detectors to measure the energy spectrum and the particle fluence.

Such a characterization has been performed in order to investigate the typical features of the proton/ion signal produced in a laser facility and identify the best experimental conditions (shielding, read-out, electronics) to perform absolute dose measurements with the Faraday Cup in a laser facility.

In particular, a relevant aspect, to consider in particle detection performed in laser environment, is the effect of the electromagnetic pulse (EMP) signal,

generated in the laser-target interaction, which strongly affects the particle signal. In order to investigate the EMP contribution, several tests have been performed. The energy of the EMP, produced by two lasers with different characteristics in terms of intensity and energy released on the target, has been measured using also different targets and focus conditions. Furthermore, EMP variations at different distance from the interaction chamber have been measured.

## 5.1 Terawatt Apparatus for Relativistic And Nonlinear Interdisciplinary Science (TARANIS)

The multi-Terawatt laser system, terawatt apparatus for relativistic and nonlinear interdisciplinary science (TARANIS), is installed in the Centre for Plasma Physics at the Queen's University in Belfast. The system supports a wide-ranging science program, which includes laser-driven particle acceleration, X-ray lasers, and high energy density physics experiments[58].

The TARANIS laser is a hybrid Ti:Sapphire-Nd:glass system operating in the chirped pulse amplification mode. The laser front-end consists of a three principal parts:

1. Ti:Sapphire Mira oscillator delivering an average power of 400 mW;
2. folded all-reflective stretcher;
3. Ti:Sapphire regenerative amplifier (RA);

As already explained in the third chapter, in the CPA scheme, a pulse made by a low power laser, which is able to create a short pulses packet that is first stretched in time (chirped in frequency), then amplified and finally recompressed.

At TARANIS the oscillator is constituted by a commercial system, Coherent Mira, that produces a train of pulses of 120 fs at a wavelength of 1053 nm, with a repetition frequency of 76 MHz. Sequentially, the train is injected into a folded all-reflective stretcher that consists of a spherical mirror, a diffraction gratin, a folding mirror located in the focal plane of the spherical mirror and a retro mirror.

A layout of the laser is shown in schematic form in the Fig. 5.1.

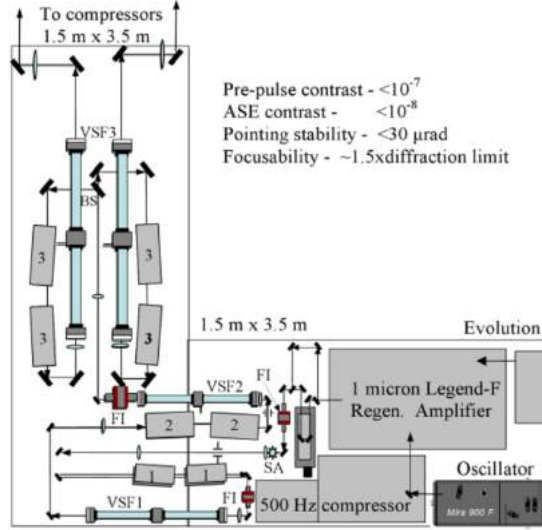


Figure 5.1: Optical layout of TARANIS laser: the numbers 1, 2 and 3 refer to the laser heads at different millimeters diameter rods; the term VSF are vacuum spatial filters located between the different amplification stages and used to obtain an high spatial quality of the beam profile; FI is referred to the Faraday isolator placed to avoid disruption of the oscillator; finally, with SA is indicated a serrated aperture and with BS is referred to a beam splitter

The bandpass of the stretcher is equal to 4 times of the laser output bandwidth with a stretching factor about  $10^4$ . The stretched pulse with a duration of 1.6 ns, enters in the last stage of the front-end which consist in the regenerative amplifier that is optimized for a high gain at a precise wavelength of 1053 nm (in order to the wavelength of the oscillator)[59]. Further amplification of the front end output occurs in three stages consisting of rod amplifiers pumped by flash lamps. Each amplification stage has two laser heads. The diameters of the rods are 9 mm, 25 mm and 50 mm which magnify the diameter the beam diameter. So the final output beam have a diameter of 100 mm. On other hand, two pulses from the glass amplification chain can be separately and re-compressed in two double-pass grating compressors each one equipped with two diffraction gratings. However, the energy extraction from the last rods is the highest giving almost 30 Joule per pulse after the

last amplification stage bypassing the compressors.

In conclusion, the TARANIS laser is a flexible system consisting of two parallel final amplification stages allowing a combination of outputs with pulse durations starting from ns to  $\sim 600$  fs and energies up to 30J.

### Target Chamber

The laser beam produced by the amplification system has to be transported to the interaction chamber where the target is placed in order to generate and accelerate the ion beam through the laser-matter interaction. The target is placed inside the interaction chamber, the operational vacuum kept in the target chamber is about  $10^4$  mbar. The target chamber consists of a cylinder, 150 cm diameter and 130 cm height, with 17 flanges, as one can see in Fig. 5.2.

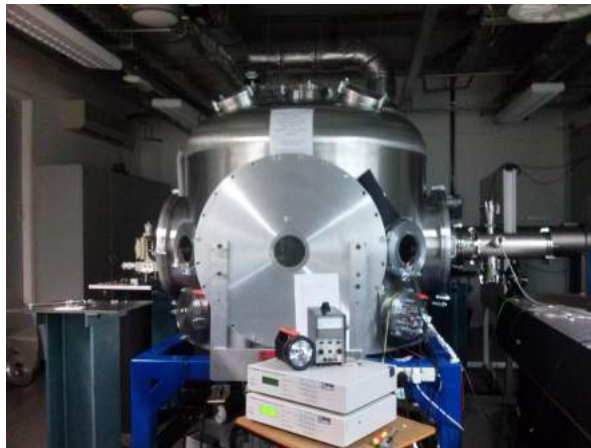


Figure 5.2: Picture of the TARANIS target chamber

## 5.2 Prague Asterix Laser System (PALS)

The core of the PALS facility is a iodine laser system, Asterix IV. The fundamental wavelength is 1315 nm and in correspondence of which the usual maximum energy delivered per pulse is about 600 J[67]. The time duration of the pulse is about  $\sim 400$  ps and the power peak, corresponding to 600 J delivered energy, is about 2 TW. The system consists of an oscillator that

generates the primary pulse followed by a succession of five power amplifiers which increase the energy of the pulse and removing the high spatial components from the angular beam spectrum. This arrangement is called Master Oscillator Power Amplifier (MOPA). The size of the amplifiers gradually increases along the chain, and the beam diameter is increased from the initial 8 mm at the output of the oscillator to 290 mm at the output of the final amplifier. A characteristic feature of the system is the high spatial uniformity of the beam, typically within  $\pm 6\%$  of the mean value. The laser can fire a full-energy shot every 20 minutes. A simplified scheme of the laser system is shown on the left side of Figure 5.3.

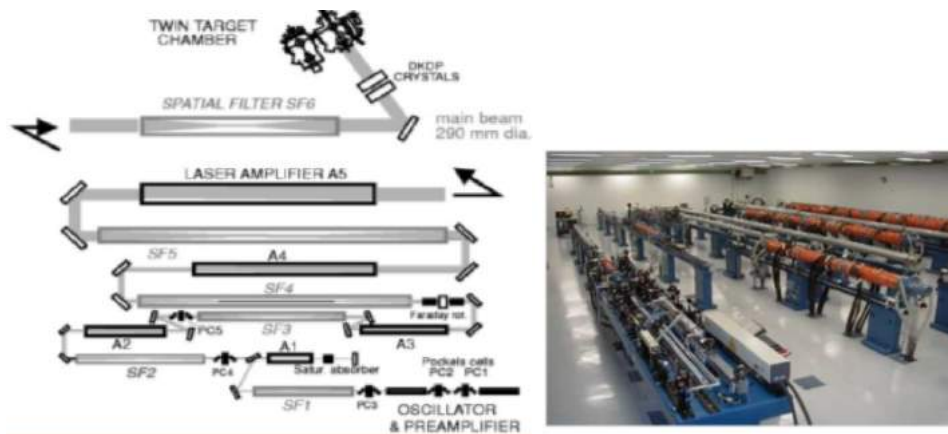


Figure 5.3: Left side: simplified scheme of the PALS laser system; right side: view of the chain amplifiers

The amplifiers are made of cuvettes filled by  $C_3F_7I$  gas. This gas laser uses neutral iodine atoms to generate of a narrow infrared line at 1315 nm. The iodine atoms dissociate from the parent iodide molecule  $C_3F_7I$  through a photochemical process called photodissociation (or photolysis). The process is caused by an external UV radiation, provided from a fresh lamp, which releases the iodine atom from the chemical bonding. The iodine atoms, which emerge from photolysis process, will be in an excited state and the laser pulse can be produced. The laser beam size amplification is made by optical telescopes, constituted by two convex lenses. The size increment is required in order to have a power density of the laser beam always below the threshold level at which the optics, in particular the lenses, can be damaged. In the following table, the parameters of the Asterix IV at PALS are reported.

<b>General</b>	Fundamental wavelenght	1315 nm
	Pulse duration	200 to 350 ps
	Pulse contrast (prepulses)	$\sim 10^{-7}$
	Repetition shot rate	25 min
	Output energy stability (over 10 shot)	$1 < \pm 1,5 \%$
<b>Main beam</b>	Pulse energy at 350 ps	1 kJ
	Pulse power at 350 ps	3 TW
	Diameter	290 mm
	Conversion efficiency to $3\omega$	55 %
<b>Auxiliary beam</b>	Pulse energy at 350 ps	100 J
	Diameter	148 mm
	Conversion efficiency to $3\omega$	30 %

Figure 5.4: The output parameters from the Asterix IV laser at PALS

### Target Chamber

The target chamber consists of a sphere with a 1 m diameter, equipped with an 80 cm diameter hinged end cap that serves as the main entrance port. A system of 15 circular ports with diameters, ranging from 64 to 500 mm, serves as connection way from the interaction chamber to the diagnostics devices for the detection, as one can see in Fig. 5.5.

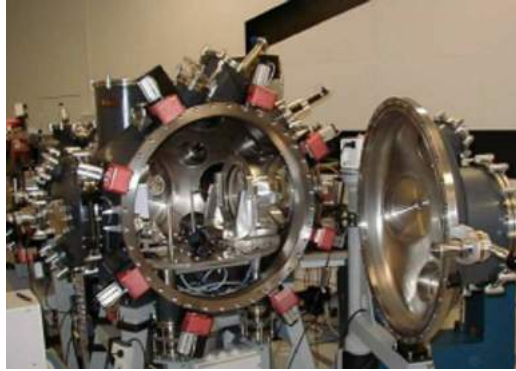


Figure 5.5: Picture of the master interaction chamber at PALS

## 5.3 Time of flight measurements

In order to characterize the particles accelerated from the plasma, a Silicon Carbide and a CVD Diamond detector have been used in ToF configuration. Both devices were chosen for their fast response, their radiation hardness and the possibility to discriminate the fastest proton signal from the ion signal generated from the plasma.

The charged particles produced can be divided into two groups, depending on the energy expressed in terms of temperature. Thanks to the deconvolution of the signal, it is possible to evaluate these two components and estimate the number and the species of the particles detected. Indeed, concerning the ion energy distribution measurements, it has been demonstrated [71] that the particle energy distribution follows a Maxwell-Boltzmann-shifted function.

### 5.3.1 Energy distribution of the ions emitted

As it has been described in chapter 3, laser-matter interaction converts the removed material from a target into a plasma which expands into the space[44]. The signal  $S_x$  of a time-of-flight detector measuring the impinging ions in x-direction depends on the detector response to their number, velocity or energy expressed by the term  $\alpha$ :

$$S_x(L, t, \alpha) \propto v_x^\alpha f(\vec{v}) d\vec{v} \quad (5.1)$$

where  $f(\mathbf{v})$  is the 3-dimensional velocity distribution function and the  $\alpha$  parameter depends on the detector response:

- $\alpha = 0$  if the response is proportional to the number (density) of incident particles;
- $\alpha = 1$  if the response is proportional to the stream (current) of incident particles;
- $\alpha = 2$  if the response is proportional to the deposited energy by particles;

Under the assumption that the detector is positioned at the distance  $L$  on the  $x$ -axis and its surface is parallel to  $y$ - $z$  direction (See Fig5.6) it is possible to obtain the number of particles impacted on the detector area  $ds=dydz$  per  $dt$ . So, the right side  $v_x^\alpha f(\vec{v})d\vec{v}$  of Eq. 5.1 can be transformed into laboratory space and time[68].



Figure 5.6: Scheme of the ion emission at distance  $L$  from the detector

In this way, each velocity component can be written as:

$$dv_x = \frac{x}{t^2} dt$$

$$dv_y = \frac{dy}{t}$$

$$dv_z = \frac{dz}{t}$$

Substituting  $L/t$  into  $f(\vec{v})d\vec{v}$  the number of particles hitting the detector's area  $ds$  per  $dt$  is then proportional to  $f(L/t)Lt^{-4}$ . Then the signal function is:

$$S_x(L, t, \alpha) \sim L^{1+\alpha}t^{-(4+\alpha)}f(L/t)dtds \quad (5.2)$$

Since the ion current  $j(L, t)$  is the sum of partial currents  $\Sigma j_{i,q}(L, t)$  of all the ionized species,  $i$ , with a charge-state  $q$ , and the shifted Maxwell–Boltzmann distribution well describes the motion of the particles, the detector signal can be expressed as:

$$S_x(L, t) = AL^{1+\alpha}t^{-(4+\alpha)}exp\left[-\frac{m_i}{2KT_i}\left(\frac{L}{t} - u_{i,q}\right)^2\right] \quad (5.3)$$

where  $m_i$  is the mass of the species constituting the partial current  $j_{i,q}(L, t)$ ,  $A$  is a normalizing term,  $u_{i,q}$  is the velocity of their centre-of-mass motion directed to the detector,  $K$  is the Boltzmann constant and  $T$  is the ion temperature. A deconvolution of the detector signal can be performed to disentangle the signal coming from the slow and the fast ion components.

A critical parameter to deconvolve the signal is the choice of the initial value of the particles temperature in the TNSA regime.

Different models of ion emission consider two-peak structure on the ion velocity and energy distributions, which are relative to hot and cold-electron temperature[70].

An useful characteristic to infer the initial temperature  $T$  of the particles and estimate the different populations, is the average intensity  $\bar{I}$  during the pulse time  $\tau_p$  on the target, defined as:

$$\bar{I} = \frac{E}{\tau_p S_{focal}} \quad (5.4)$$

where  $E$  is the energy related on the target and  $S_{focal}$  is the focal spot area assuming that the focal area is a circle. From the plasma surface the ions of the same temperature of the electrons leave with a temperature depending on the laser intensity[40]:

$$T = I\lambda^2 \quad (5.5)$$

where  $\lambda$  is the laser wavelenght.

### 5.3.2 Experimental Set-up at the TARANIS facility

A Silicon Carbide detector and a CVD diamond detector have been placed at 144 cm from the target in the backward direction.

The signal has been acquired by using a 2.5 GHz LeCroy Digital scope placed in the experimental room covered by a lead shield for the attenuation of the electromagnetic pulse. An RC circuit has been used to provide the bias voltage on the detectors and collect the signal[72], see Fig. 5.7.

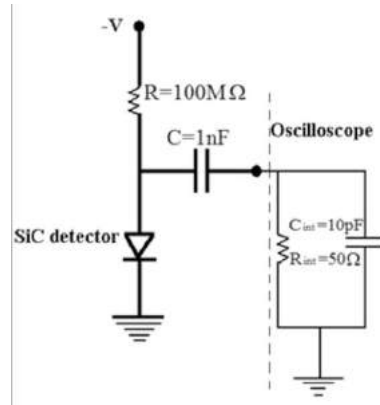


Figure 5.7: RC circuit used to provide the bias voltage

The characteristics of the detectors are briefly summarized here:

#### Silicon Carbide (4-H)

A 4H-SiC Schottky diode n-type with an active area of  $2 \times 2mm^2$  and two different dopant layers with the following characteristics:

- $n^+$  with a dopant nitrogen concentration of  $7 * 10^{18}N/cm^3$  and a thickness of  $279\mu m$ ;
- $n^-$  with a dopant nitrogen concentration of  $2,0 * 10^{15}N/cm^3$  and a thickness of  $43,7\mu m$ ;

The Schottky junction is realized by a  $0.2\mu m$  thick layer of  $Ni_2Si$  deposited on the front surface while the ohmic contact, on the back surface, is obtained with another layer of  $Ni_2Si$ [61].

The detector is composed by different active area (chips) glued on a brass foil 1mm thick with a conductive glue and single contacts between the  $Ni_2Si$  front surface and the pads of the board are realized by a wire bonding of 2  $\mu m$  thick [62]. In this experimental campaign only the chip with the active area of  $2 \times 2 mm^2$  has been used.

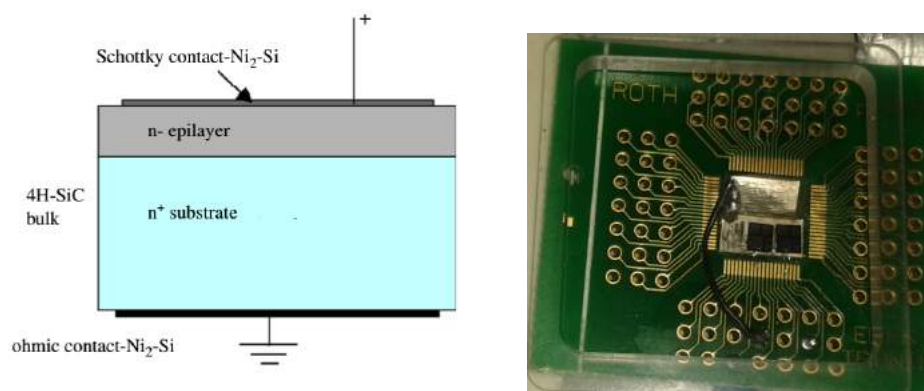


Figure 5.8: (a) The 4H-SiC diode layout (b) Picture of the SiC detector assembled on PCB board

### Chemical Vapor Deposition (CVD) Diamond

A CVD diamond detector,  $500 \mu m$  thick and area of  $0,25 cm^2$ , has been used during this experiment [60]. The front contact is composed by a single pixel with  $4,5 \times 4,5 mm^2$  active area and a dark current at 400V of 15 pA.



Figure 5.9: Picture of the CVD diamond detector shielded in a box

During the experiment at the TARANIS facility, several CR39 detectors have been placed at the same distance of the SiC and CVD detectors to measure

the fluence and also the energy spectrum, using a differential filter technique. In particular, to measure the particle energies with the CR39, a brass mask divided in four quadrants has been used: three of the quadrants have been covered with aluminium foils with different thicknesses for each region, and the fourth quadrant has been left without any foil, see Fig. 5.10. A proper thickness has been chosen in order to stop protons with energies, respectively, of 1,5 MeV, 3MeV and 6 MeV using Al foils. This evaluation has been obtained using the SRIM code based on Monte Carlo calculation [80].

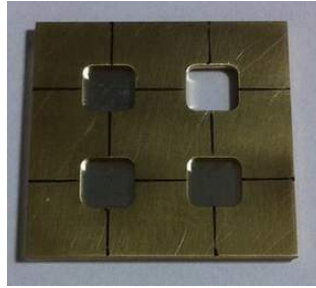


Figure 5.10: Brass shield with tree different Al filters.

In such a way, from the particle tracks detected in the three regions covered by the Al filters, it has been possible to estimate the energy of the particle and the fluency for each energy range to different stopping power.

### 5.3.3 Data analysis

As discussed in chapter 2 , using the ToF method, a signal at a certain time gives information correlated with the velocity (and so the energy). Moreover, also, the intensity of the impinging particles on the detector used for the plasma diagnostics can be extracted from the ToF distribution.

In the experimental campaign at the TARANIS laser facility, the SiC and CVD time dependent signals, generated by the ion bunches, has been registered allowing extracting the ion energy distribution and discriminating the different ion species produced. The TARANIS laser operated with an energy of 7,6J focused in a circular spot of about  $6\mu m$  diameter, reaching the intensity of  $4.6 \times 10^{19} W/cm^2$  on a 14.5um gold target. In the Fig. 5.11 and in the Fig. 5.12are shown the signals acquired with both detector corresponding to the same flight path.

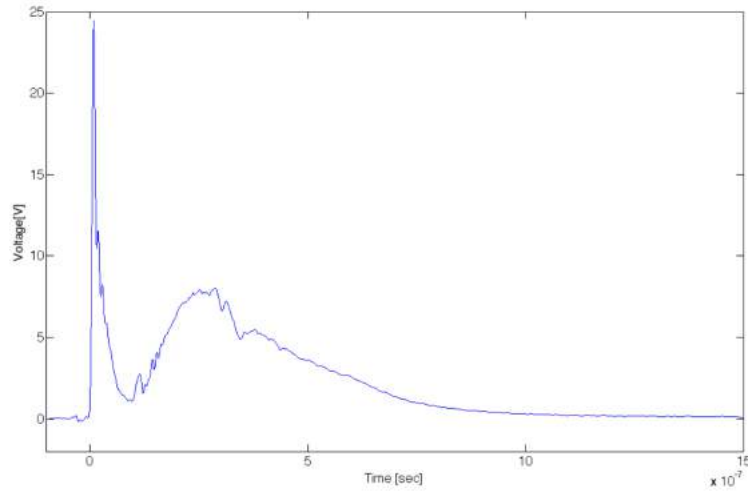


Figure 5.11: The ToF spectrum obtained from the CVD detector at 144cm

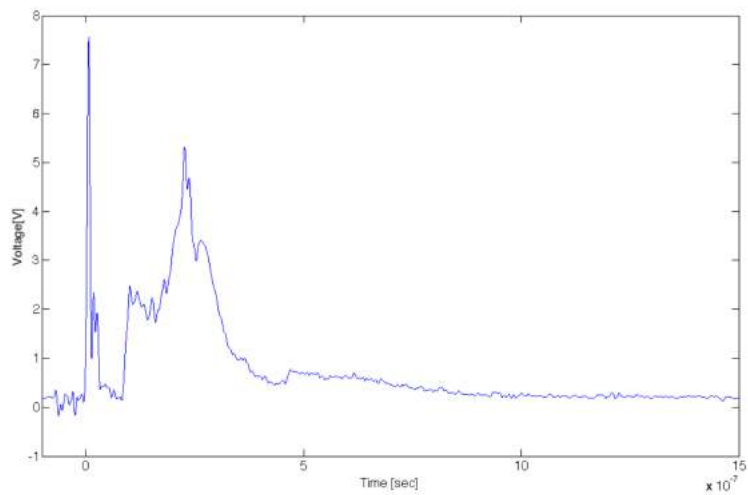


Figure 5.12: The ToF spectrum obtained from the SiC detector at 144 cm

The trigger signal for the time resolved measurements has been provided by the fast photopeak signal. In particular, during the data analysis to reconstruct the ion TOF, the first point just above the noise signal level has

been assumed to be the “zero” on the time axis. This relative zero time ensures that the following signals, due to the plasma products impinging on the detector with a certain time of flight, are measured with a good accuracy. As it is shown in the Fig. 5.11 and Fig. 5.12, in a typical TOF spectrum, the first peak, generated by photons, is followed by the peaks generated by the UV, the X-rays, the electrons and then the two bumps corresponding to protons and heavier ions.

According to the Eq. 5.3, the deconvolution of the signal has been performed in order to extract the energy of the particles emitted in laser-target interaction. In the Fig. 5.13 are shown the deconvolution curves overlapping the signal acquired with the CVD diamond detector.

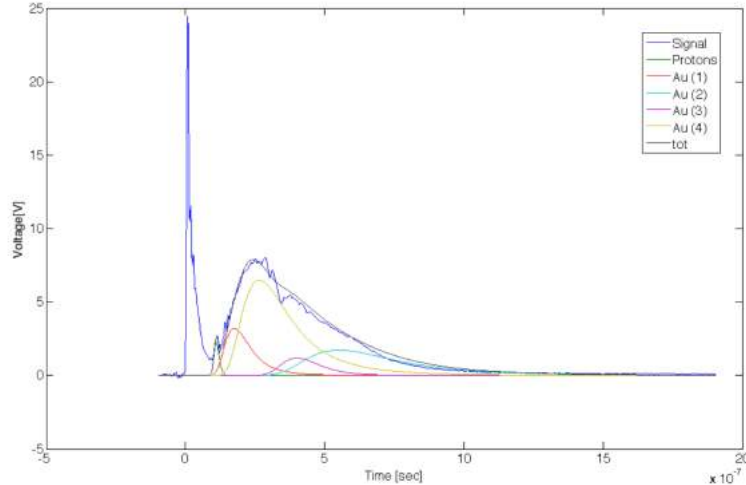


Figure 5.13: Signal obtained from the CVD detector (blue curve) together with the deconvolution curves corresponding to different ion species.

The fit of the experimental data showed maximum proton energy of about 1.1 MeV. After this peak, it is possible to assume that there are several curves corresponding to different charge states of the gold ion population excited in the laser-target acceleration mechanism. The ion energy distribution ranges from about 200 MeV to few MeV, in good agreement with the spectra expected with the TARANIS laser parameter.

The two-fundamental parameters for the fitting procedure, according to the 5.3, are the temperature of the proton and ion population and their relative

shift velocity. As discussed in the paragraph 5.3.1, a good starting point for the temperature evaluation is to consider the laser intensity in agreement with the equation 5.5. For the TARANIS laser this is the order of  $10^{11}$  K corresponding to few hundreds of KeV. The CVD signal has been also compared to the signal acquired from the SiC (see Fig.5.14)

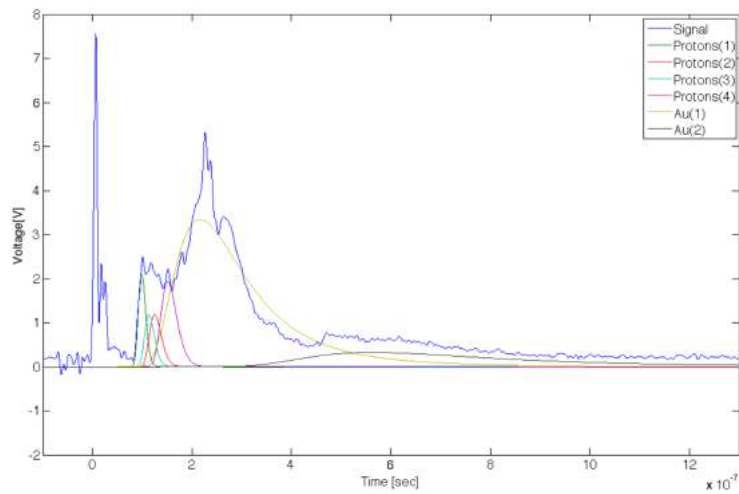


Figure 5.14: Signal obtained from SiC detector (line blue) overlapping with the deconvolution curves corresponding to several type of particles

As one can see, there are evident distinctions between the two signals acquired by different detectors. This discrepancy depends on the different active layer thickness and the resolution of both detectors.

In this experiment, the a type SiC has allowed to discriminate the different proton energies as shown in Fig 5.15.

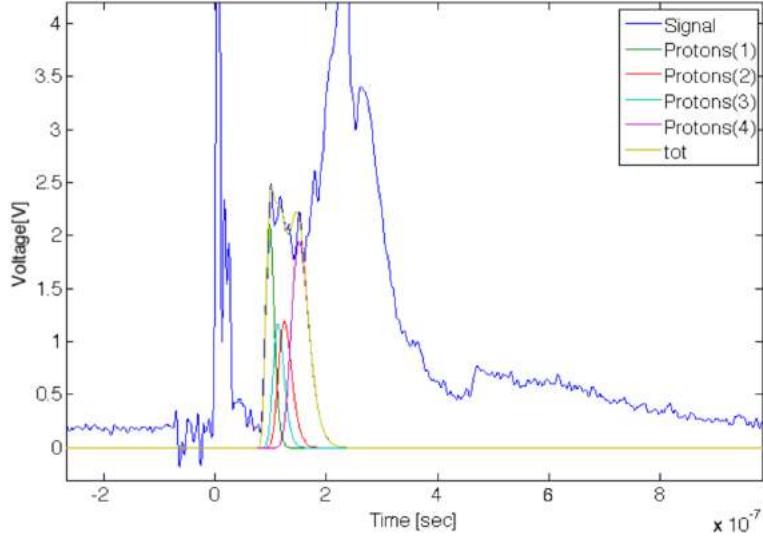


Figure 5.15: Signal registered by the SiC detector (blue curve) together with the deconvolution curves corresponding to several proton populations.

As one can see from the Fig5.15, in the proton energy distribution four peaks corresponding to 500 keV, 700 keV, 800 keV and 1 MeV, in agreement with the maximum proton energy observed in the CVD signal, can be identified.

In order to reconstruct the proton number impinging on the detector, it has been considered the linear proportionality from the charge detected  $Q$  to the number of particles  $N$ :

$$Q = \frac{eNE_G}{E} \quad (5.6)$$

where  $e$  is the elementary charge,  $E_G$  is the minimal energy needed to create the electron-hole pair inside the semiconductor active region and  $E$  is the kinetic energy of the particles which is entirely deposited in the detector sensitive layer. The energy distribution can be obtained from the first derivative of Eq. 5.6 resulting in[70]:

$$\frac{dN}{dE} = \frac{E_G V(t)}{eRE^2 \Omega_{detector}} \left( \frac{1}{2}t + \delta t \right) \quad (5.7)$$

where  $V(t)$  is the measured voltage signal at a given time  $t$  that depending on the particle kinetic energy,  $R$  is the detector impedance, which includes also the 50 Ohm termination on the scope  $\delta t$  is the smallest time step of the scope,  $\Omega_{beam}$  and  $\Omega_{detector}$  are respectively the solide angle of the beam and the detector.

In the Fig. 5.16 is reported the ratio  $\frac{dN}{dE}$  as a function of the energy for the proton peak detected by the CVD detector and shown in the Fig. 5.13.

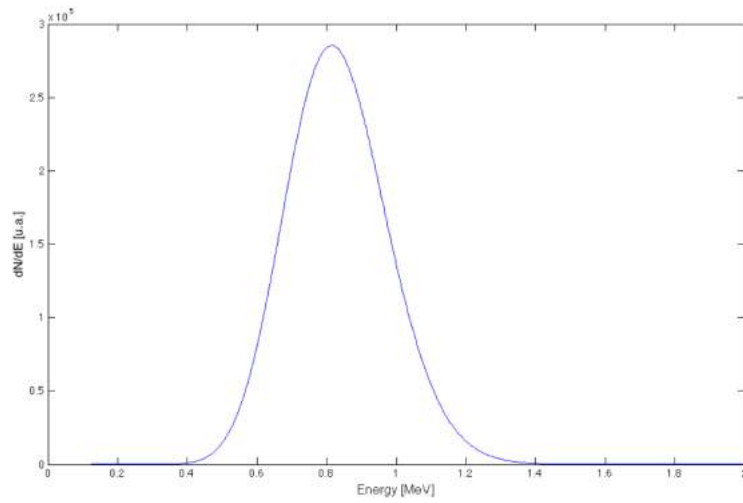


Figure 5.16: Ratio number of particle over energy as a function of the energy of the proton peak

As one can see, the proton energy distribution ranges from about 400 KeV to 1.1 MeV. The fluence, reconstructed by integrating the number of particle for the energy distribution shown in fig 5.15, is about  $2 * 10^4 [\frac{counts}{cm^2}]$ .

The study of the proton energy distribution corresponding with the different peaks detected by the SiC has shown a fluency in accord to the value estimated by the process of the CVD signal.

This result has been confirmed by the fluence measured with the CR39 placed at the same distance from the target with respect to the SiC and CVD detectors. The CR39 analysis has shown that the largest fraction of the particle has a maximum energy of about 0.1 MeV and very few particles have energies greater than 2 MeV. Furthermore, the proton energy distribution is

quite in good agreement with the typical TNSA emission, accounting many particles at low energy and few particles at higher energy.

Moreover, a fundamental parameter to evaluate the energy of the particles detected with the CR39 is the diameter and the circularity of the tracks. This analysis has been performed using the calibration curve of the proton track diameter as a function of the energy, shown in the Fig. 5.16, obtained with a NaOH etching solution 6,25 M [34].

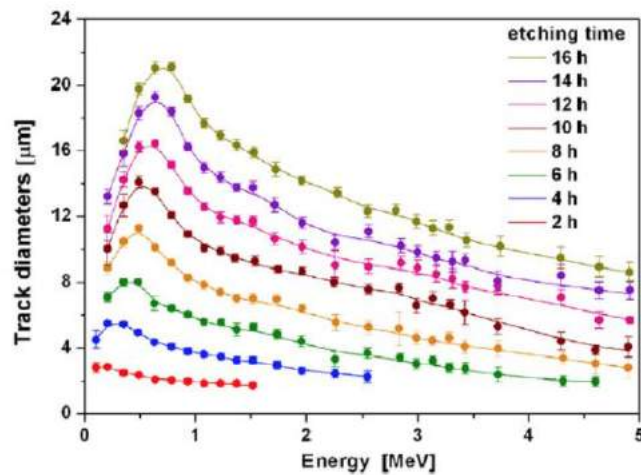


Figure 5.17: The calibration curve of the proton track diameter as a function of the energy.

The analysis of the proton tracks has been divided into several steps (see Fig. 5.18). In the first step, a thirty-minute etching has been done in order to measure the particle fluency. In the area without Al filter a particularly high track density, greater than about of  $10^8 p/cm^2$ , can be observed by visual census. On the other hand, in the areas with Al foils, a 120-minute etching procedure has been performed allowing estimating particle energies from the track diameter size.

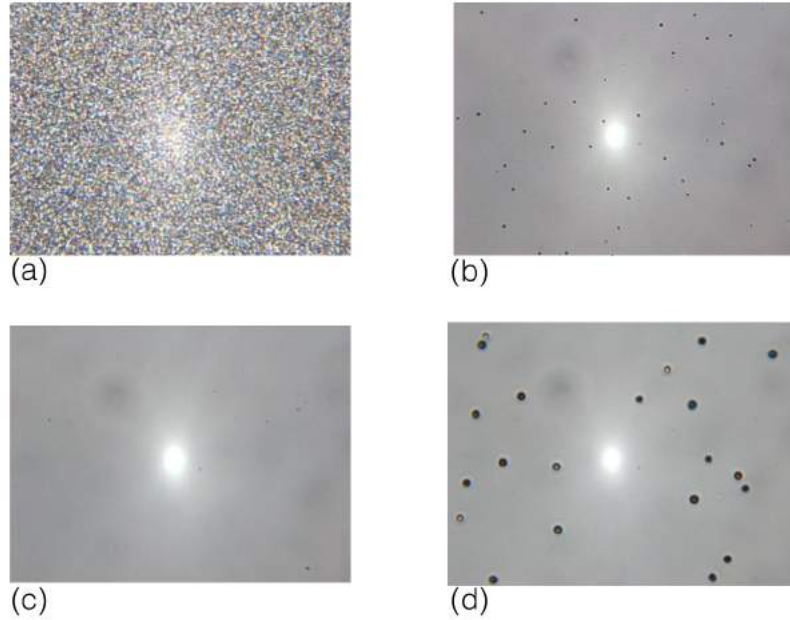


Figure 5.18: (a) CR39 region without Al filters after 30-minute etching (b) with 25 um Al filter after 30-minute etching (c) 100 um Al filter after 30-minute etching (d) 25 um Al filter after 6 hour etching

In order to get a reliable estimation of the track fluency in the region corresponding to an energy greater than 1.5 MeV (25 um Al filter), a matrix of 12x12 pictures has been taken in the central region, with 400 um steps along both of the x and the y direction accounting for a total of 124 pictures. The number of the proton tracks resulting is about  $5 * 10^3$  [counts] corresponding to a fluency of about  $10^4$  [ $\frac{counts}{cm^2}$ ]. The distribution of the track number as a function of the track diameter is shown in Fig. 5.18. As one can see, a Gaussian distribution peaked at 0.1 MeV proton energy has been obtained (Fig. 5.19).

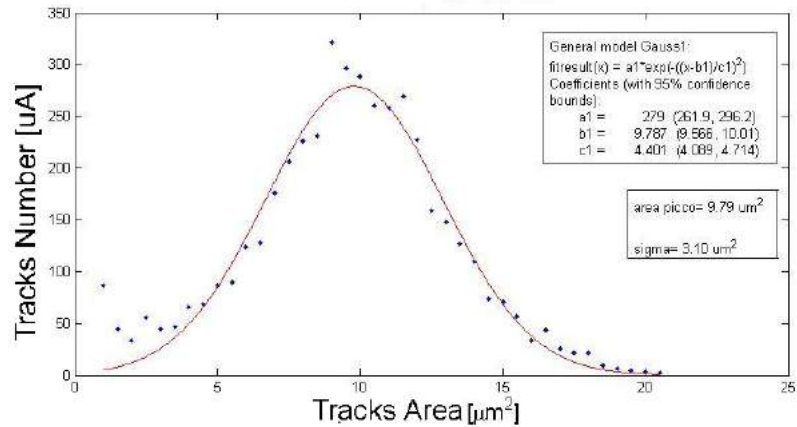


Figure 5.19: Gaussian distribution of the tracks number as function of the diameter

The etching procedure has been extended to 6 hours in order to observe also the higher energy proton. This analysis showed a maximum energy of about 2 MeV, with a fluency in agreement to the results obtained with the 120-minute time etching analysis.

In order to further confirm this result, the third and fourth areas, covered respectively with the 100 and 200  $\mu\text{m}$  Al foils, have been analysed as well. After 120 minutes of etching, this analysis has shown only a background signal comparable with what has been observed in the region covered by the brass mask. An additional 2 hour etching, reaching a total of 8 hours, has showed that no other significant tracks with energy greater than 2 MeV appear after this time. The plot showing the uniformity has been reported in Appendix B.

Furthermore, the number of the protons, the energy spectrum and the beam spot size have been also extracted from the Radiochromic film HD-V2 stack, placed at about 3 cm from the target in the forward direction. The proton energy spectrum obtained with the spectroscopic method is shown in Fig. 5.20.

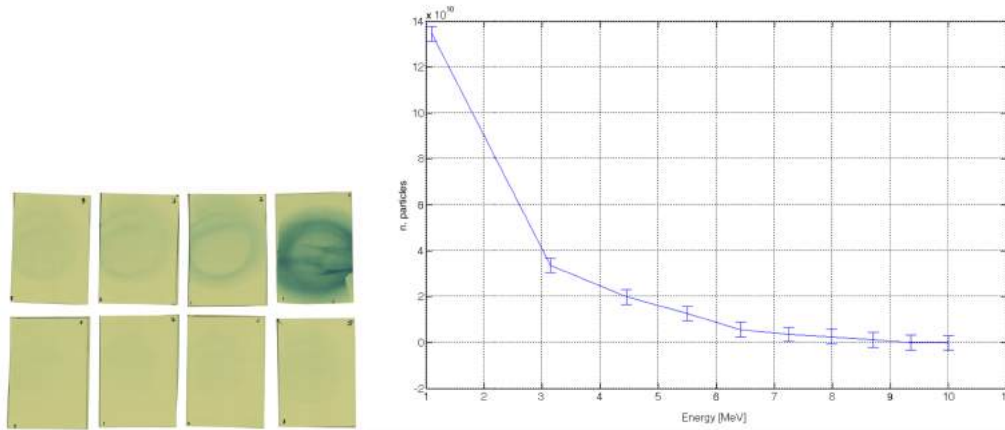


Figure 5.20: (a) Picture of the Radiochromic film stack (b) Proton energy spectrum extracted from the RCF stack.

As one can see, the maximum energy estimated in the forward direction is about 8.5 MeV with a fluence of about  $10^{11} \left[ \frac{\text{counts}}{\text{cm}^2} \right]$ . Moreover another stack of RCF placed at about 3 cm from the target in the backward direction has confirmed the same fluency in both directions.

## 5.4 ElectroMagnetic Pulse (EMP)

Interaction of high-energy and high-power laser pulses with a target is accompanied with the generation of a significant number of energetic electrons producing many secondary effects. The intense x-ray emission, ion acceleration and many other effects have been intensively studied and have been used in many applications. However there is a domain related to the laser electron acceleration, which has not yet been fully investigated. This is the generation of an intense electromagnetic pulse (EMP) during and after the laser pulse spanning a very broad frequency range from megahertz to terahertz. This transient EMP has been measured in several laser facilities with different regimes of laser intensity and pulse duration. The EMP generation is commonly attributed to radiation by laser-driven currents within the plasma and, at higher intensities, to high-energy electrons leaving the target and hitting either the chamber internal surface and/or the other elements[75]. The EMP can represent a serious limitation for the plasma diagnostics and

in general for the operation of the electronic devices. The mechanism of generation of the electric and magnetic fields in the broad frequency domain are not well known, yet. It is accepted that the fields are generated during the interaction of the laser pulse with the target and increase with the ejected charge but the exact mechanism is not defined. It could be related either to the electric current carried out by escaping electrons or with the charge accumulated on the target. The experimental data indicated that the signal strength and the temporal profile depend on the target material and geometry on the shape and the place of the metallic elements of the chamber, as well as on the laser pulse intensity and duration.

In order to evaluate this noise component, a characterization of EMP as function of the distance from the interaction chamber has been performed using several antennas placed at different distances. Thanks to this study it has been possible to infer a law that gives information to the EMP damp in a typical laser environment. Therefore, this law has helped us to identify the ideal distance in order to increase the particle signal to EMP contribution ratio.

In addition, the EMP variation as a function of the laser- target interaction in terms of intensity of laser, energy on the target and focus has been also investigated. This study has been carried out in two different laser facilities and it has pointed out all these parameters can significantly influence the EMP component.

#### 5.4.1 Characterization of the EMP propagation

An antenna converts bound circuit fields into propagating electromagnetic waves and, by reciprocity, collects power from passing electromagnetic waves. As it is known, Maxwell's equations predict that any time-varying electric or magnetic field produces an electromagnetic wave[74]. This wave has two fields oriented orthogonally, and it propagates in the direction normal to the plane defined by the perpendicular electric and magnetic fields that are expressed, assuming that  $x$  is the direction of the propagation wave, as:

$$E(x, y, z, t) = E(y, z)e^{\pm ikx - i\omega t} \quad (5.8)$$

$$B(x, y, z, t) = B(y, z)e^{\pm ikx - i\omega t} \quad (5.9)$$

where  $k$ , is the wave number and  $\omega$  is the phase.

In the study of the EMP propagation, the interaction chamber can be considered as a source that radiates spherical waves[79]. This wave propagates in the radial direction for a coordinate system centered on the source that at large distances can be approximated by plane waves. Usually, in order to evaluate both directions of propagation and the power density of the electromagnetic wave, the Poyntig vector is applied as follows:

$$\mathbf{S} = \mathbf{E} \times \mathbf{H} \left[ \frac{W}{m^2} \right] \quad (5.10)$$

where E and B are respectively the electric and magnetic field components. As it is shown, the Poynting vector is the product of the two fields and it is orthogonal to both fields so that these three terms defines a system of three coordinates ortgonal to each other[73]. In the description of electromagnetic wave propagation, if we consider a pair of concentric spheres centered on the antenna, supposed that the propagation is isotropic, it is possible to demonstrated that the power decreases by  $1/R^2$  away from the source:

$$4\pi R_1^2 S_1 = 4\pi R_2^2 S_2$$

where  $R_1$  and  $R_2$  are the two different radius of the concentric spheres. In order to validate this law, the antennas has been placed at different distances from the interaction chamber. In addition, a similar study has been repeated in two differents laser facilities, at Prague Asterix Laser System (PALS) and at Terawatt Apparatus for Relativistic And Nonlinear Interdisciplinary Science (TARANIS). In particular, four antennas have been placed and their signals have been recorded by using a 8GHz Angilent Digital scope at PALS facility and 2.5 GHz LeCroy Digital scope at TARANIS facility with DC coupled termination of 50 Ohms. In the table 5.21the experimental setup details in the two laser-facilities are listed.

	Antenna 1	Antenna 2	Antenna 3	Antenna 4
TARANIS	in the chamber at 144 cm from the target	on the external chamber wall	at 160 cm from the external chamber wall	at 350 cm from the external chamber wall
PALS	in the chamber at 5 cm from the target	on the external chamber wall	at 100 cm from the external chamber wall	at 350 cm from the external chamber wall

Figure 5.21: Experimental setup details at TARANIS and at PALS

An antenna has been placed inside the target chamber in order to have a reference signal also used for the normalization of the signals from the three antennas placed outside.

As previously discussed, each shot is different due to the poor-reproducibility. Furthermore, it has been demonstrated that the EMP emission is strongly dependent to the particle intensity generated in the laser-target interaction. A picture of the experimental setup at TARANIS facility is shown in the Fig. 5.22



Figure 5.22: Antennas placed at different distances from the interaction-chamber at the TARANIS facility.

The study of the electromagnetic wave attenuation has been performed analyzing the electrical energy obtained from the equation 5.11:

$$E = \int \frac{V(t)^2}{R} dt \quad (5.11)$$

where  $V(t)$  is the voltage signal acquired and  $R$  is the total resistivity of the antenna circuit including the termination on the scope.

The correlation between the EMP energy registered by the antenna and the distance from the interaction chamber is shown in Figs. 5.23 and 5.24, respectively at PALS and TARANIS. As one can see, it shows a linear dependence.

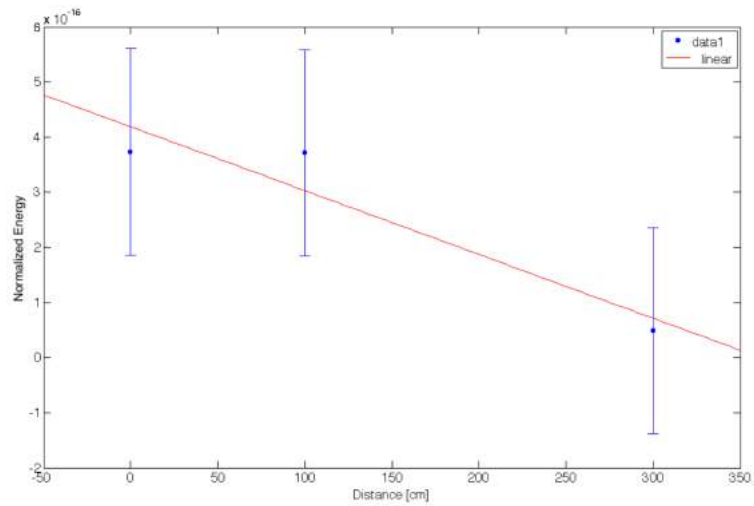


Figure 5.23: EMP normalized energy as function of the distance at PALS (The error bars represent the standard deviations)

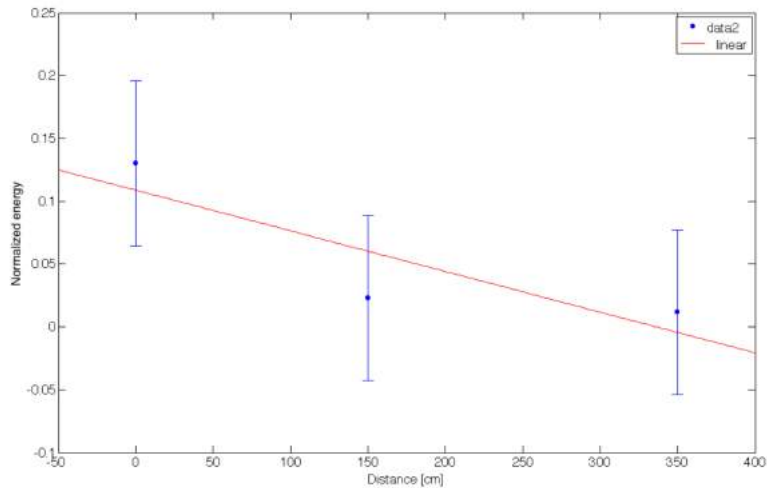


Figure 5.24: EMP normalized energy as function of the distance at TARANIS

Figs. 5.23 and 5.24 show that the attenuation law deviates from the typical attenuation behaviour of an electromagnetic wave as previously mentioned. This effect is probably due to the multiple-reflections with the metallic elements inside and outside the target-chamber. Several studies on the EMP attenuation have been performed considering the target chamber as a resonance cavity [79, 78]. Based on these studies mainly performed with Comsol simulations, each object placed inside the chamber can influence the resonance mode [79]. In addition, there is a non-negligible aspect related to the signal transport. The type of connectors and the shielding of the cable can influence the signal registered by the scope [76].

From a comparison between the curves obtained in different shots, it is possible to observe that the discrepancies between each curve decreases as the distance from the target increases, going from 10% to about 6% as one can see in Fig. 5.25.

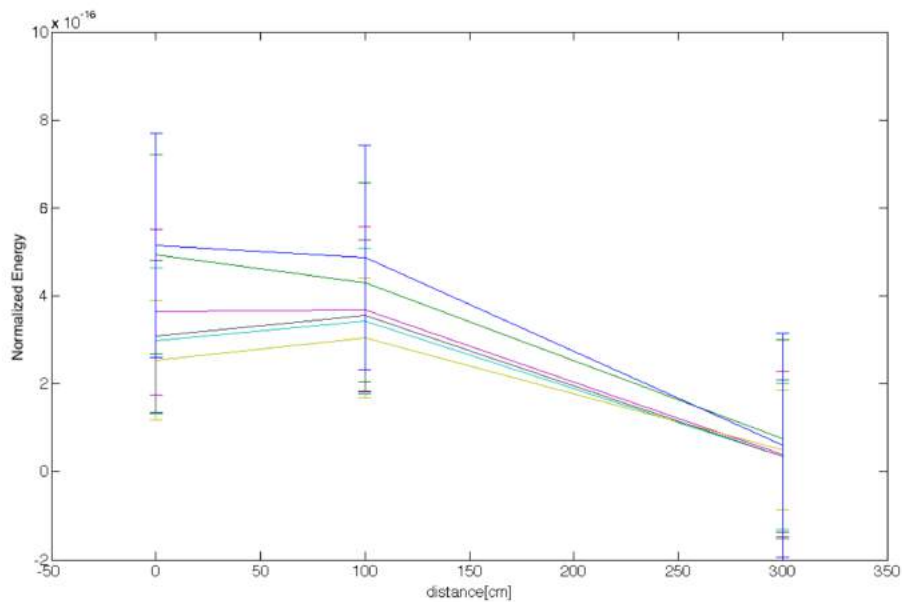


Figure 5.25: Normalized energy as function of the distance at PALS

The data taken from the antenna inside the chamber have been used as a reference signal in order to take into account the different EMP emission that varies from shot to shot. However, it has to be pointed out that the wave propagation outside the target chamber can be also affected from the propagation through the chamber walls, the propagation in the air and by the several reflection phenomena by the metallic objects placed outside.

Moreover, one of the possible explanation of the discrepancies observed in the signals from the antennas placed on the target chamber walls ( $d=0$  cm) could be due by their extreme proximity to the big Aluminum chamber, indeed the size and the metallic nature of the chamber could interfere with the antenna signal.

A comparison between the fitting parameters of the first plot Fig. 5.23 (related with the data acquired at PALS) and the second one Fig. 5.24 (related with the data acquired at TARANIS ) expressed in voltage has shown a similar trend with an angular coefficient discrepancy of about 1%.

## 5.4.2 EMP signal investigation as a function of the laser parameters

Several studies based on the correlation between the EMP emission and the particles emitted by the laser-target interaction, has been performed. Thanks to these analyses, the possibility to isolate several laser parameter that influence the EMP generation has emerged. In the current dissertation, an investigation of the EMP signal relation with the laser characteristics has been performed.

The EMP variation as a function of the energy released on the target has been evaluated. The EMP energy has been extract according to the Eq. 5.11. In the Fig. 5.26 and Fig. 5.27 are reported the results respectively at the TARANIS and the PALS campaigns, considering the antenna placed on the chamber walls.

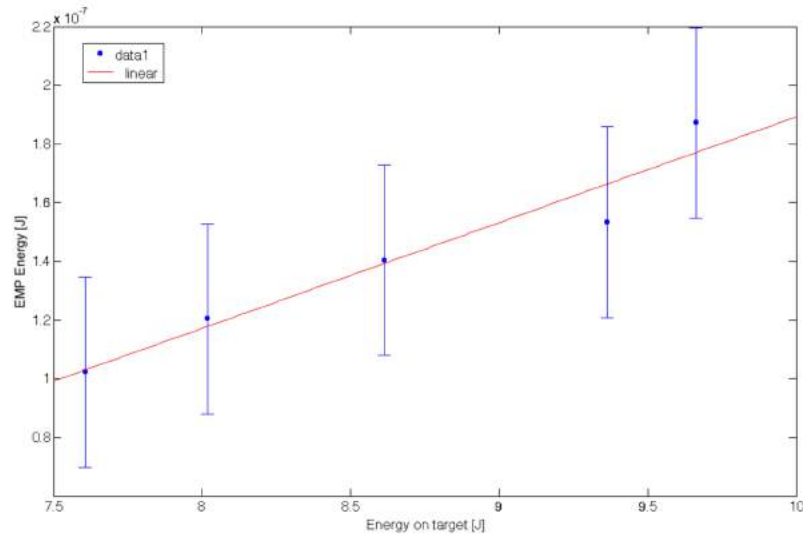


Figure 5.26: EMP energy emission at TARANIS facility as function of Energy released on target (The error bars represent the standard deviations)

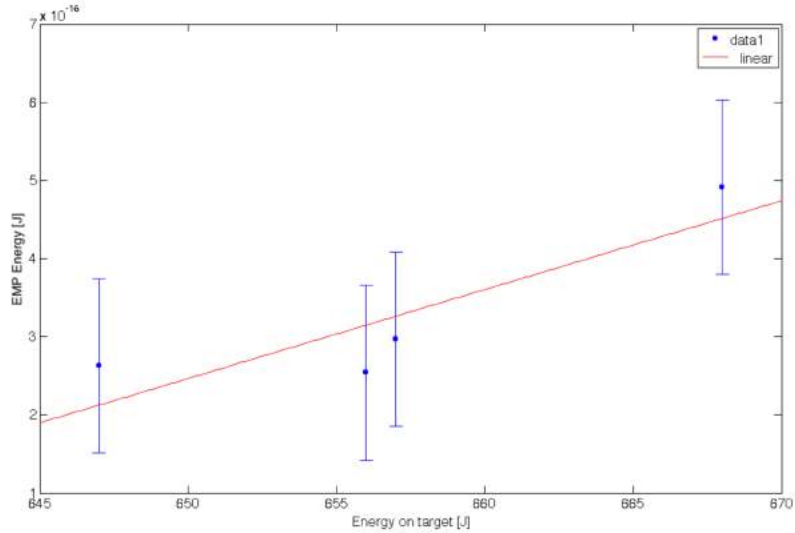


Figure 5.27: EMP energy emission at PALS facility as function of energy released on target (The error bars represent the standard deviations)

The TARANIS laser operates with an intensity of the order about  $10^{19}W/cm^2$  and the energy on the target varying from about 7.2 J to 9.8 J focused into a  $6\mu m$  circular spot in a 12.5  $\mu m$  Au target. On the other hand, the iodine laser pulse at PALS operates with an energy from about 630 J to 670 J focused into a  $100\mu m$  circular spot on a double target of Polimetilmetacrilate-Hydrogen-Boron reaching the intensity of about  $10^{17}W/cm^2$  on target.

The results show an increment of the EMP energy as a function of the energy released on the target, in agreement to the several experimental evidence observed in different laser facilities [76, 77]. A maximum standard deviation of 10% has been found, this value represents the repeatability of each shot in the same condition. The EMP energy fluctuations can be related to the variation in the laser focus on the target and several factor discussed previously such as the reflection in the chamber.

The EMP emission as a function of the energy released on the target and the laser intensity for the two experimental campaigns are reported in the Fig. 5.28 and Fig. 5.29.

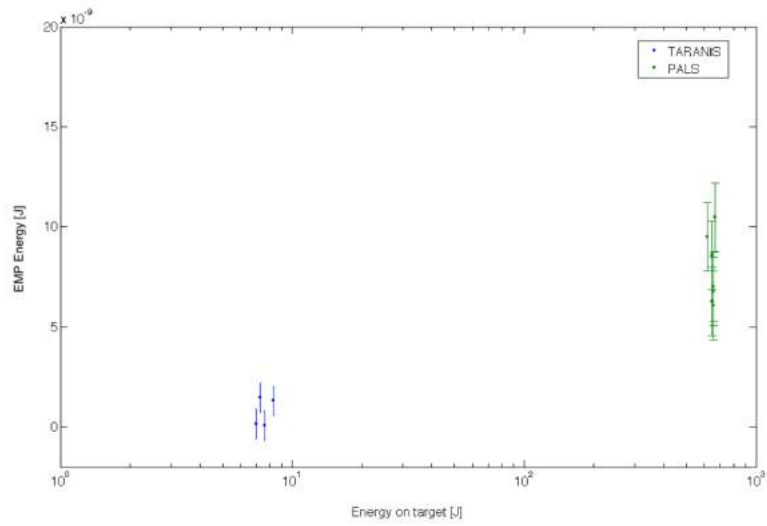


Figure 5.28: EMP energy emission at PALS and TARANIS facility as a function of energy released on target (The error bars represent the standard deviations)

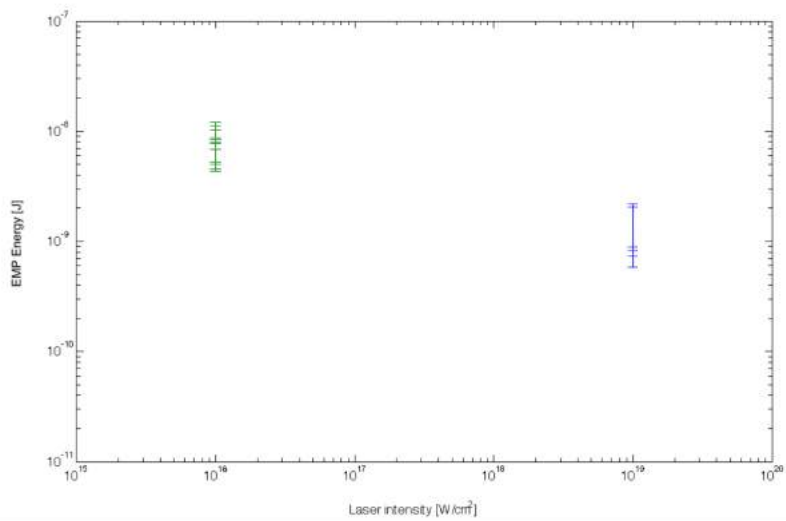


Figure 5.29: EMP energy emission at PALS and TARANIS facility as a function of laser intensity (The error bars represent the standard deviations)

As one can see, the EMP energy increases with the laser energy and decreases with the laser intensity according to experimental evidence published in [77]. The physical phenomena, associated to this result, seem to be correlated to the different temperatures of the plasma[75]. When the high energy of the laser is released to the target, both target destruction and plasma creation are generated. Several simulations performed with PIC code have shown that the energy transferred on the hot and cold electrons seems to be associated to the EMP emission. An additional confirm of this hypothesis might be the EMP variation observed as a function of the variation of the laser focus on the spot.

Therefore, following this hypothesis, at the TARANIS facility, the EMP emission as a function of the focus variation has been evaluated. Three antennas have been placed at different distances outside of the chamber. The first has been placed on the chamber walls, the second at 120 cm and the third at 250 cm from the chamber walls. The targets used were a 20  $\mu\text{m}$  Molibden foil and 12.5  $\mu\text{m}$  Gold foil. In Fig 5.30 is reported the energy of the antennas as a function of the distance.

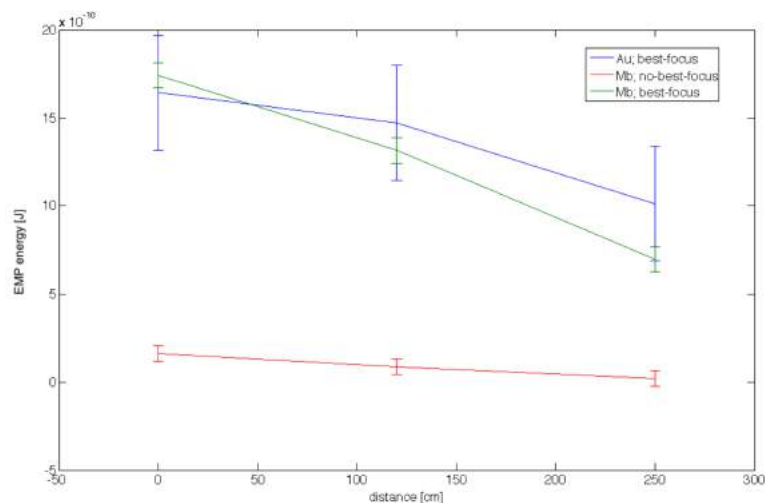


Figure 5.30: Energy released on target as function of the distance changing the laser focusing on the spot and the type of target (The error bars represent the standard deviations)

The blue and the green curves refer to the energy acquired in the best fo-

cus condition respectively with the Molibden and Gold target. On the other hand, the red curve refers to the energy acquired in the no-best-focus condition with Molibden target. As one can see, in agreement with the linear dependence with the distance observed in Fig. 5.30, the energy measured decreases when the distance increases. Moreover, an energy reduction, of about 80%, can be observed from the comparison between the best and non-best focus condition. On other hand, from comparison between the EMP energy emitted in best-focus condition with the two different targets, the EMP variation is about 4% only. This result indicate that the EMP emission variation seems to be strongly affected by the focus condition rather than the type of target.

## Conclusion

The fundamental goal pursued in the current dissertation is the characterization of an innovative Faraday Cup device, designed and realised in the context of the ELIMED project, with the aim to realize dose measurements in the future facility of laser driven beams, actually in construction in Prague (accomplishing schedule by 2017).

The characterization of this device has been led during three different experimental runs, the first of which took place in Catania, at the hadrontherapy facility CATANA of the Southern National Laboratory (LNS-INFN).

The tested Faraday Cup has been designed and built in order to maximize charge collection and minimize the uncertainty related to dose calculation. This device features a peculiar geometric configuration of the inner electrode making it more efficient in the charge-collection process in comparison to the traditional Faraday Cups actually employed in radiotherapy.

The first experimental test has been focused mainly on the characterization of the detector response without inner electrode and with conventional 62 MeV proton beams. The collected charge has been measured applying different voltages to the external electrode and the obtained trend shows a good agreement with the traditional response of conventional Faraday Cups.

Furthermore, the proton beam absolute dose has been measured, fixing the voltage applied to the electrode, and a discrepancy not greater than 6% with respect to the doses measured with a conventional dosimetric ionisation chamber, has been observed.

In conclusion, the dependence of the FC response with the beam dose rate, evaluating the response of the secondary beam monitor detector (SEM) signal has been estimated. From the latter measurement, a non-linear trend due to an underestimation of the dose at low dose rates, has been observed. As future prospects it has been planned to carry out more precise measurements at low dose rates in order to pinpoint the exact dose rate value in which the FC signal gets nonlinear. In addition, an experimental campaign aimed to investigate the FC charge signal applying the voltage on both inner and the outer electrode has been planned at LNS in order to quantify the increasing of the charge collection as expected by the simulations performed by means of the software SIMION. The occurred experimental campaign had also the purpose to implement two acquisition and analysis softwares that will be used for the future beam line that will be realized in Prague. A software

to process the image of beam spot acquired with Radiochromic films and a front-panel for the FC signals acquisition with an electrometer have been, indeed, developed in Matlab and Labview codes, respectively.

As it is written above, during the operations here in described, two additional experimental runs have been led in two laser facilities: at the Terawatt Apparatus for Relativistic And Nonlinear Interdisciplinary Science (TARANIS), at the Queen's University in Belfast (UK) and at the Prague Asterix Laser System (PALS) in Prague (CZ). The main purposes of these campaign have been respectively the measurement of the energy spectra and the fluence of laser-driven beams produced in the TNSA regime and the electromagnetic noise evaluation, which may notably affect the measurements.

These two aspects are crucial points for the prediction of the Faraday Cup response in a laser facility. Regarding plasma diagnostics, a SiC and a CVD detector in ToF configuration have been used. The signals from SiC and CVD have been deconvolved to make possible the evaluation of the species, the number, and the energy of the produced particles. Using some CR39 devices, located near the same detectors, a good agreement between the counted particles with CR39s and the ones obtained analysing the ToF signals has revealed. Finally, an estimation of the electromagnetic noise allowed to appraise how the EMP changes in relation to the laser features and the distance with respect to the target. Such kind of measure is meaningful to quantify the noise superimposed on the FC signal, which could be hiding the particle signal and affect the precise absolute dose measurements.

## Ringraziamenti

Le prime persone che devo ringraziare sono il mio relatore Giacomo Cuttone, per avermi indirizzato nel progetto ELIMED, i miei correlatori e tutto il gruppo di laboratorio con cui ho lavorato. In particolare vorrei ringraziare Pablo, per aver avuto sempre fiducia in me, per la pazienza dimostratami e per avermi dato l'eccezionale possibilità di lavorare anche all'estero facendomi confrontare per la prima volta con una realtà completamente diversa da quella di "casa".

Vorrei ringraziare Valentina e Giuliana, per i consigli datemi, per essermi state sempre accanto e avermi sostenuto fino all'ultimo, anche quando le ore si facevano piccole e le m.b.c.s.k.t. erano tante.

Renata, Rosanna, Giacomo, Francesco e Valentina per essere stati sempre disponibili e pronti a darmi una mano e a risolvere i mille problemi che emergevano.

Una volta qualcuno ha detto che "le tesi migliori sono quelle su cui si lavora fino all'ultimo", io non so quanto questo sia vero, non so se la mia tesi sia migliore o peggiore di altre ma so che questo lavoro di tesi è stato un percorso di un anno intero che mi ha dato proprio fino all'ultimo l'opportunità di crescere e di migliorare sia dal punto di vista professionale che umano.

So che se non avessi avuto accanto qualcuna di queste persone non sarebbe stato possibile niente di tutto questo. Ringrazio quindi ognuno di loro per quest'ultimo anno trascorso insieme e per questo traguardo raggiunto.

Infine devo ringraziare i miei genitori, per esserci sempre, per il sostegno che mi hanno dato finora e per non aver cambiato la serratura di casa quando si sono resi conto che a volte vorrei definitivamente trasferire la mia residenza al laboratorio. Ringrazio i miei amici, quelli di sempre, che sempre mi sosterranno in qualsiasi impresa folle voglia imbarcarmi. E infine ringrazio Alessandro, per la pazienza e per il supporto datomi.

## Appendix A

```
Main Function clear all
close all
disp('—');
disp('This script evaluates GAF outlines: after profiles extraction the func-
tion calculates the diameter of the spot and the lateral penumbra');
disp('—');
% Scanner dpi Resolution
Ris = 25.4/127; %127 dpi -> 25.4/127=200 um % pixel/cm conversion
%Load calibration lines for EBT3
M = dlmread('Parametri_fit_EBT3.txt','');
N = dlmread('Average+Dose_EBT3.txt');
O = 'EBT30';
% Image calibration
[a,b]=size(N);
for s=1:1:a;
AverageR(s,1)=N(s,1);
Dose(s)=N(s,2);
end
a1=M(1);
b1=M(2);
c1=M(3);
a2=M(4);
b2=M(5);
c2=M(6);
f = fittype('a1*exp(-((x-b1)/c1)^2) + a2*exp(-((x-b2)/c2)^2)');
PR = cfit(f,a1,b1,c1,a2,b2,c2);
% Select image for profile evaluation %
[FileName,PathName]=uigetfile('*.tif','Select the image');
fullchosenfile = [PathName FileName];
image=imread(fullchosenfile);
```

```

%Select from the image only the beam spot
figure(1)
[ROI rect]=imcrop(image);
[m,n]=size(ROI);
y=1:m; x=1:n/3;
%Plot the image according to several codes
subplot(2,1,1) imshow(ROI); title('Original image');
A = rgb2gray(ROI); subplot(2,1,2) imshow(A); title('Greyscale');
%Insert a dynamic vector h=imdistline; dist = getDistance(h);
stats = FoundBeamSpot(ROI);
%Calculate the diameter and find the spot center
for region = 1 : length(stats)
Diameter(region) = stats(region).EquivDiameter;
Centro_x(region) = stats(region).Centroid(1);
Centro_y(region) = stats(region).Centroid(2);
end
% Index of the detected center ROI_CX = round(Centro_x(region));
ROI_CY = round(Centro_y(region));
radius = Diameter(region)/2;
%Calibrate the image in dose
for i=1:m
for j=1:n/3
doseDistributionR(i,j)= interp1(AverageR(:,1),Dose(:,double(ROI(i,j,1))),'PR');
doseDistribution(i,j)=(doseDistributionR(i,j));
end
end
% Normalisation of the dose matrix: normalisation value is a mean value
% calculated in a square region around the center of the beam spot.
% The square semi-dimension is chosen to be 1/5 the radius of the circular
% beam spot size
ROI_halfSize = round((1/5)*radius);

```

```

[PVM, DoseNorm] = DoseNormalisation(doseDistribution, ROI_halfSize, ROI_CX,
ROI_CY);
%*****
%*** Profile extraction ***
%*****

[rows, columns] = size(DoseNorm);
minimalMatrixDimension = min(rows, columns);
% Building a squared matrix around the central crop
SquaredMatrix = DoseNorm(ROI_CY-maximalDimension:ROI_CY+maximalDimension,
...
ROI_CX-maximalDimension:ROI_CX+maximalDimension);
% Find the indexes of the central point in 'SquaredMatrix'
% corresponding to the points (ROI_CX, ROI_CY) ella 'DoseNorm'
[CX CY] = find(SquaredMatrix == 100);
% Profile along X and along Y
profileAlongX = SquaredMatrix(CY, :);
profileAlongY = SquaredMatrix(:, CX);
% Profile along the first diagonal
profileAlongDiagonal = diag(SquaredMatrix);
profileAlongAntiDiagonal = diag(fliplr(SquaredMatrix));
figure
imshow(DoseNorm)
hold on
X1 = [ROI_CX ROI_CX];
X2 = [1 columns];
Y1 = [1 rows];
Y2 = [ROI_CY ROI_CY];
plot(ROI_CX, ROI_CY, 'o', X1, Y1, X2, Y2)
%%
LAlongX = length(profileAlongX);
% the same for the profileAlongY
LAlongY = length(profileAlongY);

```

```

LAlongDiagonal = length(profileAlongDiagonal);
LAlongAntiDiagonal = length(profileAlongAntiDiagonal);
distanceAlongX = Ris/2:Ris:LAlongX*Ris;
distanceAlongY = Ris/2:Ris:LAlongY*Ris;
distanceAlongDiagonal = (Ris*sqrt(2))/2 : Ris*sqrt(2) : LAlongDiagonal*Ris*sqrt(2);
distanceAlongAntiDiagonal = (Ris*sqrt(2))/2 : Ris*sqrt(2) : LAlongAntiDiagonal*Ris*sqrt(2);
% Since each profile vector differs in lenght from one another
% it is mandatory to execute some translations if you want them to fit in
space
lengthAlongX = distanceAlongX(LAlongX);
lengthAlongY = distanceAlongY(LAlongY);
lengthAlondDiagonal = distanceAlongDiagonal(LAlongDiagonal);
lengthAlondAntiDiagonal = distanceAlongAntiDiagonal(LAlongAntiDiagonal);
traslation1 = (lengthAlongX - lengthAlongY)/2;
traslation2 = (lengthAlongX - lengthAlondDiagonal)/2;
traslation3 = (lengthAlongX - lengthAlondAntiDiagonal)/2;
distanceAlongY = distanceAlongY + traslation1;
distanceAlongDiagonal = distanceAlongDiagonal + traslation2;
distanceAlongAntiDiagonal = distanceAlongAntiDiagonal + traslation3;
figure
plot(distanceAlongX, profileAlongX,'-',...
distanceAlongY, profileAlongY,'-',...
distanceAlongDiagonal, profileAlongDiagonal,'+',...
distanceAlongAntiDiagonal, profileAlongAntiDiagonal,'v') l
legend('Along X','Along Y','Diagonal','Anti diagonal')
% Making pofile coordinates symmetrical in relation to the new center
% (CX,CY)negative on the left and positive on the right
distanceAlongX_Simmetrico = distanceAlongX - distanceAlongX(CY);
distanceAlongY_Simmetrico = distanceAlongY - distanceAlongY(CX);
distanceAlongDiagonal_Simmetrico = distanceAlongDiagonal - distanceAlongDiagonal(CX);

```

```

distanceAlongAntiDiagonal_Simmetrico = distanceAlongAntiDiagonal - dis-
tanceAlongAntiDiagonal(CY);
% Plot X e Y profiles
figure plot(distanceAlongX_Simmetrico, profileAlongX,'o',...)
distanceAlongY_Simmetrico, profileAlongY, '-','...
distanceAlongDiagonal_Simmetrico, profileAlongDiagonal,'*',...
distanceAlongAntiDiagonal_Simmetrico, profileAlongAntiDiagonal,'v');
legend('X Profile','Y profile','Diagonal','Anti Diagonal')
xlabel('Distance from axis [mm]')
ylabel('Dose [a.u.]')
[distanceAlongX_Simmetrico_pos, distanceAlongX_Simmetrico_neg, pro-
fileAlongX_pos, profileAlongX_neg]
= symmetric(distanceAlongX_Simmetrico, profileAlongX);
[distanceAlongY_Simmetrico_pos, distanceAlongY_Simmetrico_neg, pro-
fileAlongY_pos, profileAlongY_neg]
= symmetric(distanceAlongY_Simmetrico, profileAlongY);
[distanceAlongDiagonal_Simmetrico_pos, distanceAlongDiagonal_Simmetrico_neg,
profileAlongDiagonal_pos, profileAlongDiagonal_neg] =
symmetric(distanceAlongDiagonal_Simmetrico, profileAlongDiagonal);
[distanceAlongAntiDiagonal_Simmetrico_pos, distanceAlongAntiDiagonal_Simmetrico_neg,
profileAlongAntiDiagonal_pos,
profileAlongAntiDiagonal_neg] = symmetric(distanceAlongAntiDiagonal_Simmetrico,
profileAlongAntiDiagonal);
%*****
%** 90% **
%*****
%right profile [ p_profileX_dx90, X_profileX_dx90 ] =
function_interp( 90, distanceAlongX_Simmetrico_pos, profileAlongX_pos);
[ p_profileY_dx90, X_profileY_dx90 ] = function_interp( 90, distanceA-
longY_Simmetrico_pos, profileAlongY_pos);
[ p_profileDiagonal_dx90, X_profileDiagonal_dx90 ] =
function_interp( 90, distanceAlongDiagonal_Simmetrico_pos, profileAlong-
Diagonal_pos);

```

```

[ p_profileAntiDiagonal_dx90, X_profileAntiDiagonal_dx90 ] =
function_interp( 90, distanceAlongAntiDiagonal_Simmetrico_pos, profileAlongAntiDiagonal_pos);
%left profile [ p_profileX_sx90, X_profileX_sx90 ] =
function_interp( 90, distanceAlongX_Simmetrico_neg, profileAlongX_neg);
[ p_profileY_sx90, X_profileY_sx90 ] = function_interp( 90, distanceAlongY_Simmetrico_neg, profileAlongY_neg);
[ p_profileDiagonal_sx90, X_profileDiagonal_sx90 ] =
function_interp( 90, distanceAlongDiagonal_Simmetrico_neg, profileAlongDiagonal_neg);
[ p_profileAntiDiagonal_sx90, X_profileAntiDiagonal_sx90 ] =
function_interp( 90, distanceAlongAntiDiagonal_Simmetrico_neg, profileAlongAntiDiagonal_neg);
%% Repeat the same string changing '90' with '80','50' and '20'
%*****
%** Diameter Calculation **
%*****
%_____90_____
diameter_90X=X_profileX_dx90 + abs(X_profileX_sx90);
diameter_90Y=X_profileY_dx90 + abs(X_profileY_sx90);
diameter_90Diagonal=X_profileDiagonal_dx90 + abs(X_profileDiagonal_sx90);
diameter_90AntiDiagonal=
X_profileAntiDiagonal_dx90 + abs(X_profileAntiDiagonal_sx90);
%% Repeat the same string changing '90' with '80','50' and '20'
%*****
%** Means diameter Calculation **
%*****
diameter90=[diameter_90X, diameter_90Y,diameter_90Diagonal,diameter_90AntiDiagonal];
profile90=mean(diameter90)
diameter80=[diameter_80X, diameter_80Y,diameter_80Diagonal,diameter_80AntiDiagonal];
profile80=mean(diameter80)
diameter50=[diameter_50X, diameter_50Y,diameter_50Diagonal,diameter_50AntiDiagonal];

```

```

profile50=mean(diameter50)
penumbra1 = X_profileX_dx20-X_profileX_dx80;
penumbra2 = X_profileY_dx20-X_profileY_dx80;
penumbra3 = X_profileDiagonal_dx20-X_profileDiagonal_dx80;
penumbra4 = X_profileAntiDiagonal_dx20-X_profileAntiDiagonal_dx80;
penumbra8020 = mean([penumbra1, penumbra2, penumbra3, penumbra4])

```

## Secondary Function

- Dose normalization

```

function [PVM, doseNormalised] = DoseNormalisation(doseDistribution,...
ROI_halfSize, ROI_CX, ROI_CY)
% Normalisation procedure of a square dose matrix
% % The original matrix must be normalised in such a way that a given
point
% will assume the '100' value. %
% This procedure will normalise the matrix to a medium pixel value (PVM).
% PVM is calculated as the average of the pixel values in a square region %
centered in (ROI_CX, ROI_CY).
% The half side of the square ROI is an input.
% % The PVM value will be then associated to the point (ROI_CX, ROI_CY)
% of the doseDistribution matrix (doseDistribution(CX,CY) = PVM);
% % The normalisation will consist into the division of each point of the
% dose matrix to PVM.
% In such a way will ever result doseProfile(ROI_CX,ROI_CY) = 100;
% % INPUT:
% - doseDistribution: matrix of the dose distribution
% - ROI_halfSize: halside of the square region around (ROI_CX, ROI_CY)
% - ROI_CX, ROI_CY: indexes of the coordinates of the center of the cir-
cular
% detected region
% % OUTPUT:

```

```

% - doseNormalised
% - PVM
pixelValueSum = 0;
for i = ROI_CX - ROI_halfSize:ROI_CX + ROI_halfSize
for j = ROI_CY - ROI_halfSize:ROI_CY + ROI_halfSize
pixelValueSum = pixelValueSum + doseDistribution(i,j);
end
end
squareArea = (2*(ROI_halfSize) + 1)^2;
%PVM or Pixel Value Medium PVM=pixelValueSum/squareArea;
% The PVM value is associated to the point (ROI_CX, ROI_CY)
doseDistribution(ROI_CY,ROI_CX) = PVM;
% Normalisation of the dose profile dose
Normalised = (doseDistribution./doseDistribution(ROI_CY,ROI_CX))*100;

```

- Function Interp

```

function [ p, XP ] = Valori_interesse( n, X, Y )
%The function has to check X and
%Y axes and verify if they have increasing or decreasing trend
%Difference between n and each element in Y diff= abs(n - Y);
min_diff = min(diff);
index_min_diff = find(diff == min_diff);
value_min_diff_Y=Y(index_min_diff);
if X(1)<0
% disp('Calculate the left profile');
if n>=value_min_diff_Y min_Y=Y(index_min_diff);
min_X=X(index_min_diff);
max_Y=Y(index_min_diff+1);
max_X=X(index_min_diff+1);
else
max_Y=Y(index_min_diff);
max_X=X(index_min_diff);

```

```

min_Y=Y(index_min_diff-1);
min_X=X(index_min_diff-1);
end
end
if X(1)>0
% disp('Calculate the right profile');
if value_min_diff_Y>=n
max_Y=Y(index_min_diff);
max_X=X(index_min_diff);
min_Y=Y(index_min_diff+1);
min_X=X(index_min_diff+1);
else
min_Y=Y(index_min_diff);
min_X=X(index_min_diff);
max_Y=Y(index_min_diff-1);
max_X=X(index_min_diff-1);
end
end
y=[max_Y, min_Y];
x=[max_X, min_X];
% -----
%Execute an interpolation between points A and B y=ax+b
p=polyfit(x,y,1);
a=p(1); b=p(2);
XP=(n-b)/a;
end

```

- Symmetric

```

function [X_pos, X_neg, Y_pos, Y_neg] = symmetric(X,Y)
index_X_neg = find(X <= 0);
index_X_pos = find(X > 0);
X_neg = X(find(X <=0));

```

```
X_pos = X(find(X >0));  
Y_neg = Y(index_X_neg);  
Y_pos = Y(index_X_pos);  
end
```

## Appendix B

### Uniformity analysis

After 120 minutes of etching, an uniformity analysis in the area has been performed with a 25  $\mu\text{m}$  Aluminium filter.

In order to evaluate the distribution of the particles number, 20 pictures have been taken along the vertical axes and longitudinal axes with a step of 400  $\mu\text{m}$ . In the Fig. 5.31 and 5.32 is shown the distribution plots of two different directions.

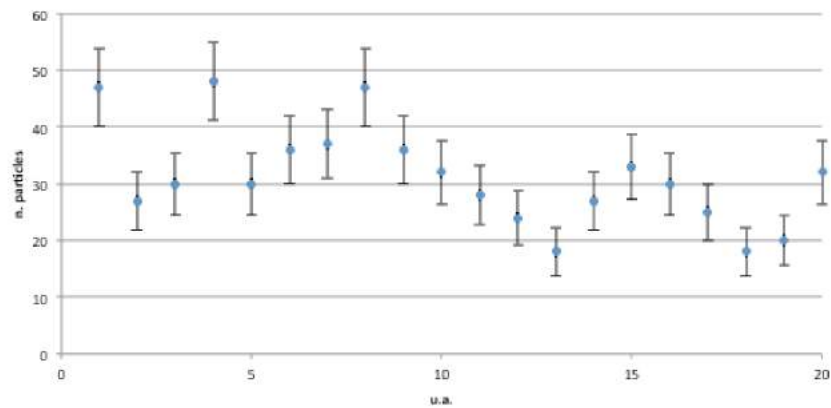


Figure 5.31: Particles distribution along X-axes

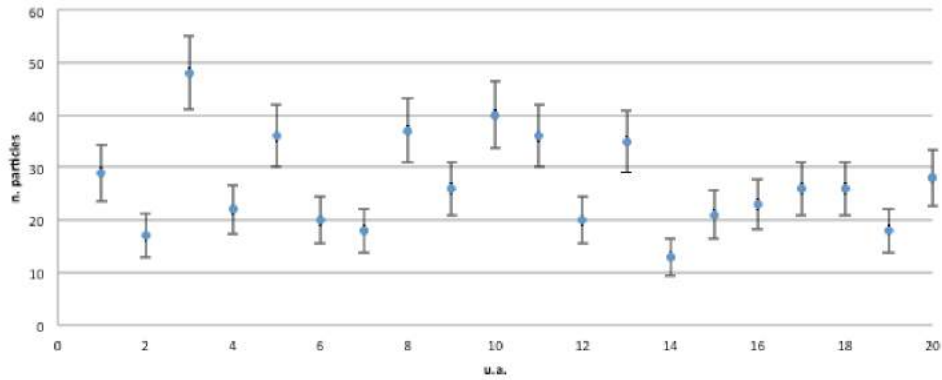


Figure 5.32: Particles distribution along Y-axes

The uniformity is the order of  $10^7$  for the X-axes distribution and  $10^6$  for the Y-axes distribution. The results are reported in the Fig. 5.33.

	row 1	row 2	row 3	row 4	row 5
<b>Mean Particle Number</b>	39.4	44	44.6	56	41.8
<b>Dev. Standard</b>	2.8	5.6	10.5	12.2	7.5
<b>Uniformity [%]</b>	92.2	87.3	76.5	78.2	82.1

	column 1	column 2	column 3	column 4	column 5
<b>Mean Particle Number</b>	39.6	38.2	50.4	49.8	47.6
<b>Dev. Standard</b>	9.8	2.8	11.6	10.7	6.3
<b>Uniformity [%]</b>	75.2	92.7	76.9	78.5	86.7

Figure 5.33: Uniformity analysis

# Appendix C

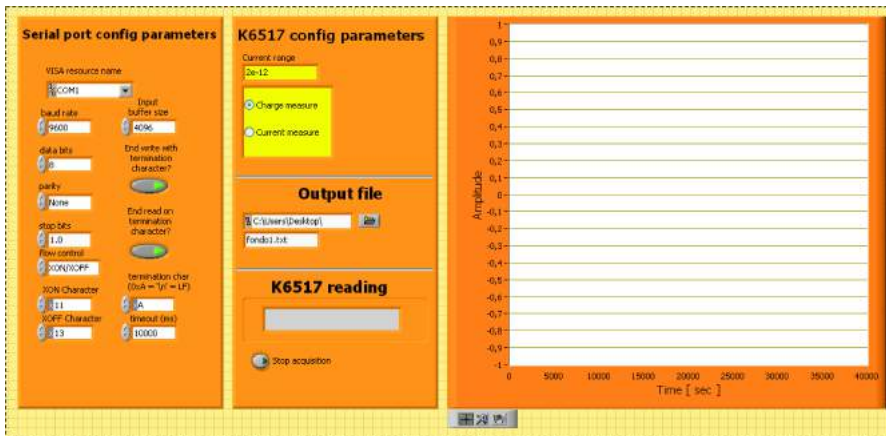


Figure 5.34: Front panel of the acquisition system

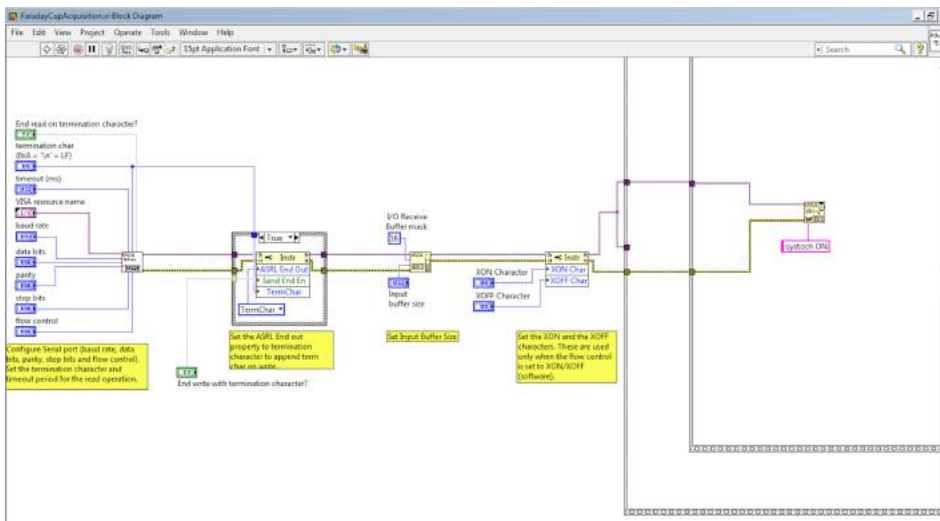


Figure 5.35: Port initialization connected to Keithley

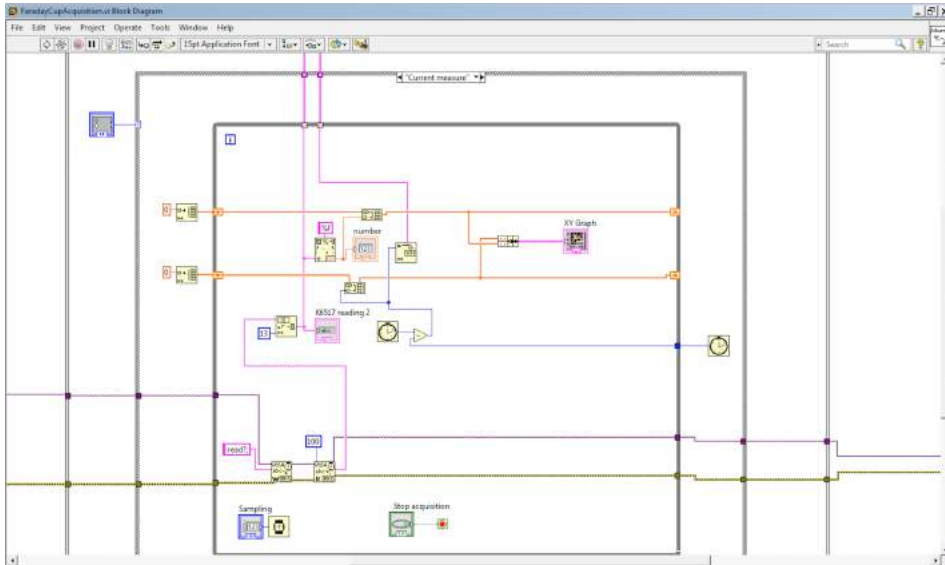


Figure 5.36: Signal processing

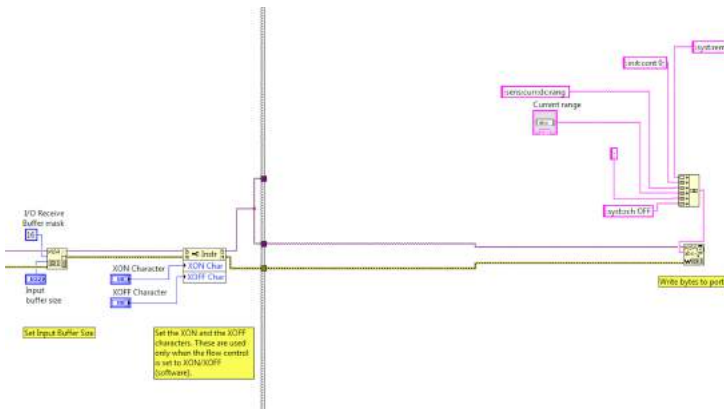


Figure 5.37: Disabling acquisition

# Bibliography

- [1] Siegel R., Ma Liemin, Zou Z., Jemal A., "Cancer Statistics 2014", Cancer Journal for Clinicians, January 2014
- [2] PTCOG, facilities in operation: <http://www.ptcog.ch/index.php/facilities-in-operation>
- [3] G. A. P. Cirrone, G. Cuttone, D. Battaglia, L. Calabretta et al., "The INFN Experience in the Hadron Therapy Field", Polish J. of Environ. Stud. Vol. 15 No. 4A (2006), 171-173
- [4] U. Amaldi, B. Larsson, Y.Lemoige, "Advances in Hadrontherapy", ICS International Congress Series 1144
- [5] F. H. Attix, "Introduction to Radiological Physics and Radiation Dosimetry", Wiley VCH
- [6] K. Kase, B.B. Bjarngard, F.H.Attix, "The dosimetry of ionizing radiation", Vol. II Academic Press
- [7] Proposal for an INFN experiment 2013 - 2015, "ELIMED: MEDical applications at ELI-Beamlines", August 2012
- [8] Leo, William R., "Techniques for Nuclear and Particle Physics Experiments", Springer Verlag, Second Edition
- [9] N. Bohr, "On the theory of the decrease of velocity of moving electrified particles on passing through matter", Philosophical Magazine Series 6 Volume 25, Issue 145, 1913
- [10] Glenn F. Knoll, "Radiation Detection and measurement", John Wiley & Sons, Third Edition

- [11] ICRU, 1993, ICRU Report 51, “Quantities and Units in Radiation Protection Dosimetry International Commission on Radiation Units and Measurements”, Bethesda, MD.
- [12] A. Tramontana et al., “Medical research and multidisciplinary applications with laser-accelerated beams: the ELIMED network at ELI-Beamlines”, 10.1088/1748-0221/9/04/C04026
- [13] Loeffler, J. S. Durante, M. Nat. Rev. Clin. Oncol. advance online publication 21 May 2013; doi:10.1038/nrclinonc.2013.79
- [14] J. J. Livingood, “Principles of cyclic particle accelerators”, D. Van Nostrand Company, Inc., Princeton, New Jersey
- [15] S.Yamada et al. , NIRS Int. Seminar on Appl. Of Heavy Ion Accelerator to Radiation Therapy of Cancer, p.1
- [16] M. Nishiuchi , H. Sakaki,” Toward laser driven proton medical accelerator”, Journal of Physics: Conference Series 244 (2010) 022051
- [17] P.Heikkinen, “Injection and Extraction for Cyclotrons”, CERN Accelerator School: 5th General Accelerator Physics Course
- [18] P.J.Bryant, “Introduction to Transfer Lines and Circular Machines”, Lectures given in the Academic Training Programme of CERN, CERN 84-04.
- [19] G.A.P. Cirrone, F. Romano et al., ”Transport and dosimetric solutions for the ELIMED laser-driven beam line”, Nuclear Instruments & Methods in Physics Research A (2015)
- [20] The PLASMAMED project at INFN, <https://sites.google.com/site/elimedfacility/>
- [21] G. A. P. Cirrone et al., “ELIMED, future hadrontherapy applications of laser- accelerated beams”, NIMA 730 174-177 (2013)
- [22] D. Margarone, P. Cirrone, G. Cuttone, G. Korn, “2nd ELIMED Workshop and Panel”, Catania 18-19 October 2012, AIP- Proceeding Vol.1546

- [23] V. Scuderi et al., “Development of an energy selector system for laser-driven proton beam applications”, *Nuclear Instruments and Methods in Physics Research A* 740 (2014) 87–93
- [24] M. Maggiore et al., “Design and realisation of a Thomson Spectrometer for Laser Plasma Facilities”, 23rd Symposium on Plasma Physics and Technology (SPPT), *Acta Technica* 56 (2011) T266.
- [25] A. Tramontana, “Produzione di Plasmi-Laser e monitoraggio con spettrometro di Thomson per applicazioni medicali.”, 2011/2012
- [26] F. Schillaci, “Modellizzazione e Diagnostica di Fasci di Ioni Accelerati Otticamente”, 2011/2012
- [27] R. J. Tapper, “Diamond detectors in particle physics”, *Rep. Prog. Phys.* 63 (2000) 1273–1316. Printed in the UK
- [28] J. Prokupek, D. Margarone et al., “Experimental test of ToF diagnostic for PW class lasers”, *Proc. of SPIE* Vol.8779
- [29] M. Marinelli, E. Milani et al., “Analysis of laser-generated plasma ionizing radiation by synthetic single crystal diamond detectors”, *Applied Surface Science* 272 (2003) 104-108
- [30] G. Bertuccio, D. Puglisi et al., “Silicon carbide detector for laser-generated plasma radiation”, *Applied Surface Science* 272 (2013) 128-131
- [31] D. Margarone, J. Krasa et al., “New methods for high current ion beam production by laser-driven acceleration”
- [32] F. Fusi, G. Cuttone, et al., “Optical characterization of a radiochromic film by total reflectance and transmittance measurements”, *MEDICAL PHYSICS* 31(7):2147-54 · August 2004
- [34] A. Szydlowski, J. Badziak, et al., “Application of solid-state nuclear track detectors of the CR-39/PM-355 type for measurements of energetic protons emitted from plasma produced by an ultra-intense laser”, *Radiation Measurements* 44 (2009) 881–884

- [35] J. Y. Lee, J. H. Jo, H. Park et al. "Study on the Tracks in a Nuclear Track Detector (CR39) for Detection of Laser-Induced Charged Particles", *Journal of the Korean Physical Society*, Vol. 51, No. 1, July 2007, pp. 426~430
- [36] H.P. Schlenvoigt, O. Jäcke, S. M. Pfotenhauer and M. C. Kaluza<sup>1</sup>, "Laser-based Particle Acceleration", Mikhail Grishin 2010
- [37] Brehm J J; Mullins W. J., "Introduction to the structure of matter: a course in modern physics", John Wiley & Sons, 1988
- [38] John Howard, "Introduction to Plasma Physics", April 15, 2002
- [39] C. Labaune, C. Baccou et al., "Fusion reactions initiated by laser-accelerated particle beams in a laser-produced plasma", *Nature Communications* 4:2506 doi:10.1038/ncomms3506 (2013)
- [40] Richard Fitzpatrick, "Plasma Physics"
- [41] M. Passoni, V. T. Tikhonchuk, et al. "Charge separation effects in solid targets and ion acceleration with a two-temperature electron distribution", *Physical Review E* 69, 026411 2004
- [42] Paul M. Bellan, "Fundamental of Plasma Physics"
- [43] M. Zepf, M. Borghesi," Radiation Pressure Acceleration in the Light-Sail Regime", 37th EPS Conference on Plasma Physics
- [44] P. Gibbon, "Short pulse laser interaction with matter an introduction", Paul Gibbon, Imperial College Press 2007
- [45] A. Macchi, M. Borghesi, M. Passoni, "Ion acceleration by superintense laser - plasma interaction", arXiv:1302.1775v1 [physics.plasm-ph] 7 Feb 2013
- [46] Grussell E, Isacson U, Montelius A and Medin J *Phys. Med. Biol.* 40 1831–1840 (1995).
- [47] G. Cuttone, L. Raffaele et al, "First dosimetry intercomparison Results for the CATANA Project", *Physica Medica* Vol.XV, N.3, July September 1999

- [48] Z. B. Zhang , L. Chen et al, "A compensated coaxial Faraday Cup for absolute bunched proton beam current determination", Nuclear Instruments and Methods in Physics Research A 764 (2014) 257–260
- [49] Stopping Powers & Ranges for Protons & Alpha Particles (ICRU Report N. 49). Intl. Commission on Radiation (June 1993).
- [50] R Cambriay, J H´eraultz, N Brassartz, M Silarixk and P Chauvelz, "Proton beam dosimetry: A comparison between the Faraday Cup and an ionization chamber", Phys. Med. Biol. 42 (1997) 1185–1196.
- [51] C Richter, L Karsch, Y Dammene, S D Kraft, J Metzkes, U Schramm, M Schu rer, M Sobiella, A Weber, K Zeil and JPawelke, Phys. Med. Biol. 56 1529–1543 (2011).
- [52] Lynn J. Verhey et al, "The determination of Aborbed Dose in a Proton Beam for Proposes of Charged-Particle Radiation Therapy", Radiation Research, Vol 79 No1(Jul 1979), pp34-54
- [53] J.D. Thomas, G.S. Hodges, D.G. Seely, N.A. Moroz, T.J. Kvale, "Performance enhancement study of an electrostatic Faraday Cup detector", Nuclear Instruments and Methods in Physics Research A 536 (2005) 11–21
- [54] Seong Hee Park et al., "Faraday Cup Measurements of a Laser-Induced Plasma for a Laser-Proton Acceleration", Journal of the Korean Physical Society, Vol. 49, No. 1, July 2006
- [55] J. Prokupek at al., "Development and first experimental tests of Faraday Cup array", Reviw of scientific Instruments 85, 013302 (2014)
- [56] G. G. Milluzzo, "Monte Carlo simulation and experimental tests of a Faraday Cup for absolute dosimetry with high pulsed ion beams", 2014/2015
- [57] D. Margarone, J. Jrasa et al., "Full characterization of laser-accelerated ion beams using Faraday Cup, silicon carbide, and single-crystal diamond detectors", Journal of Applied Physics 109, 103302 (2011)
- [58] C. L. S. Lewis, D. Riley, "Proceedings of the 11th International Conference on X-Ray Laser", August 2008

- [59] T. Dzelzainis, G.Nersisyan et al, "The TARANIS laser: A multi-Terawatt system for laser-plasma investigations", Laser and Particle Beams, pag. 1 of 11, 2010. Cambridge University Press
- [60] G.A.P. Cirrone, G. Cuttone et al, "Dosimetric characterization of CVD diamonds irradiated with 62 MeV proton beams", Nuclear Instruments and Methods in Physics Research A 552(2005) 192-202
- [61] M. De Napoli, G. Raciti et al., "Response of silicon carbide detectors", Nuclear Instruments and Methods in Physics Research A 572(2007) 831-838
- [62] M. De Napoli, F. Giacoppo et al., "Study of charge collection efficiency in 4H-SiC Schottky diodes with  $^{12}\text{C}$  ions", Nuclear Instruments and Methods in Physics Research A 608 (2009) 80-85
- [63] J.S. Pearlman and G.H. Dahlbacka," Emission of rf radiation from laser-produced plasmas", Journal of Applied Physics 49, 457(1987)
- [64] L. Vinoth Kumar, E. Manikanta et al, "RF emissions form laser breakdown of target materials", 978-1-4799-2174-4/13 2013 IEEE
- [65] G. Cuttone, G. A. P. Cirrone, et al., "Implementation of a new Monte Carlo simulation tool for the development of a proton therapy beam line and verification of the related dose distributions", IEEE Transactions on Nuclear Science, 52 1756-1758.
- [66] G. Cuttone, G. A. P. Cirrone, et al., "Catana protontherapy facility: The state of art of clinical and dosimetric experience", The European Physical Journal Plus, July 2011, 126:65
- [67] Prague Asterix Laser Facility: <http://www.pals.cas.cz/>
- [68] J. Krasa, "Gaussian energy distribution of fast ions emitted by laser-produced plasmas", Applied Surface Science 272 (2013) 46–49
- [69] J. Krasa, L. Velardi, A. Lorusso, et al., "Distance-of-flight spectra of charge density of ions generated with low laser intensity", Journal of Physics: Conference Series 508 (2014) 012004
- [70] J. Prokupek, "Diagnostic Systems for Laser-Accelerated Ion Beams", 2012

- [71] D. Margarone, J. Krasa, et al., "Full characterization of laser-accelerated ion beams using Faraday Cup, silicon carbide, and single-crystal diamond detector", *Journal of Physics*: 109 (2011) 103302
- [72] C. K. Alexander, M. N. O. Sadiku, "Circuiti Elettrici", Mc-Graw Hill Education, Terza edizione
- [73] J.D. Jackson, "Classical Electrodynamics", John Wiley & Sons Ltd., 3rd edition
- [74] S. Barabrino, "Appunti di Teoria sulle Antenne I", 2014
- [75] J.L. Dubois, F.L. Lavaderci, D. Raffestin, et al., "Target charging in short-pulse laser-plasma experimentis", *Physical Review* 89, 013102 (2014)
- [76] M. De Marco, M. Pfeifer, et al., "Basic features of electromagnetic pulse generated in a laser-target chamber at 3-TW laser facility PALS", *Journal of Physics: Conference Series* 508 (2014) 012007
- [77] J. Cikhardt, J. Krasa, M. De Marco, et al., "Measurement of the target current by inductive probe during laser interaction on terawatt laser system PALS", *Review of scientific instruments* 85, 103507 (2014)
- [78] M. De Marco, J. Cikhardt, J. Krasa, et al., "Electromagnetic pulses produced by expanding laser-produced Au plasma", *NUKLEONIKA* 2015;60(2):239: 243
- [79] F. Consoli, R. DeAngelisa et al., "Measurement of the radiofrequency-microwave pulse produced in experiments of laser-plasma interaction in the ABC laser facility", *Physics Procedia* 62 (2015) 11 – 17
- [80] SRIM code: <http://www.srim.org>